NOVEL CAVITIES IN VERTICAL EXTERNAL CAVITY SURFACE EMITTING LASERS FOR EMISSION IN BROAD SPECTRAL REGION BY MEANS OF NONLINEAR FREQUENCY CONVERSION

by

Michal L. Lukowski

A Dissertation Submitted to the Faculty of the

DEPARTMENT OF OPTICAL SCIENCES

In Partial Fulfillment of the Requirements for the Degree of

DOCTOR OF PHILOSOPHY

In the Graduate College

THE UNIVERSITY OF ARIZONA

2016

THE UNIVERSITY OF ARIZONA
GRADUATE COLLEGE

As members of the Dissertation Committee, we certify that we have read the dissertation prepared by Michal L. Lukowski, titled Novel Cavities in Vertical External Cavity Surface Emitting Lasers for Emission in Broad Spectral Region by Means of Nonlinear Frequency Conversion and recommend that it be accepted as fulfilling the dissertation requirement for the Degree of Doctor of Philosophy.

____ Date: 08/04/2016
Mahmoud Fallahi

____ Date: 08/04/2016
Ewan Wright

____ Date: 08/04/2016
Robert Norwood

Final approval and acceptance of this dissertation is contingent upon the candidate's submission of the final copies of the dissertation to the Graduate College.

I hereby certify that I have read this dissertation prepared under my direction and recommend that it be accepted as fulfilling the dissertation requirement.

____ Date: 08/04/2016
Dissertation Director: Mahmoud Fallahi

STATEMENT BY AUTHOR

This dissertation has been submitted in partial fulfillment of the requirements for an advanced degree at the University of Arizona and is deposited in the University Library to be made available to borrowers under rules of the Library.

Brief quotations from this dissertation are allowable without special permission, provided that an accurate acknowledgement of the source is made. Requests for permission for extended quotation from or reproduction of this manuscript in whole or in part may be granted by the head of the major department or the Dean of the Graduate College when in his or her judgment the proposed use of the material is in the interests of scholarship. In all other instances, however, permission must be obtained from the author.

SIGNED: Michal Lukowski

Acknowledgements

I would like to thank my advisor Prof. Mahmoud Fallahi for giving me the amazing opportunity to conduct research on VECSELs at the University of Arizona. I greatly appreciate his support, guidance and encouragement throughout my years at the College of Optical Sciences and will be forever grateful.

I am especially thankful to Professor Robert Norwood and Professor Ewan Wright for finding time to provide advice and meticulously review this dissertation.

Extraordinarily appreciation to Dr. Chris Hessenius with whom I spent countless hours, day and night building lasers and conversing. I could have not imagined a better lab mate.

Thank you to my colleagues with whom I have worked over the years, Jason Meyer, Olli Nordman, Omid Mahdavi and Dr. Mike Yarborough.

To everyone at the College of Optical Sciences for making it such a friendly and welcoming place to come and work at every day.

I would like to thank Prof. dr. hab. Maciej Bugajski and Dr. Anna Wojcik-Jedlinska at the Institute of Electron Technology in Poland for introducing and putting me on the path of VECSELs.

Finally, I would like to thank my parents, my grandparents, my sister and my family for all of their support. I am particularly grateful to my girlfriend Brooke, who was by my side the whole time. I am thankful for her infinite patience and understanding for the crazy and random work schedule. I unconditionally appreciate your love, help and support.

to my grandfathers Henio and Romek

Table of Contents

List of Figures

List of Tables

Abstract

Optically pumped semiconductor vertical external cavity surface emitting lasers (VECSEL) were first demonstrated in the mid 1990's. Due to the unique design properties of extended cavity lasers VECSELs have been able to provide tunable, high-output powers while maintaining excellent beam quality. These features offer a wide range of possible applications in areas such as medicine, spectroscopy, defense, imaging, communications and entertainment. Nowadays, newly developed VECSELs, cover the spectral regions from red (600 nm) to around 5 μm. By taking the advantage of the open cavity design, the emission can be further expanded to UV or THz regions by the means of intracavity nonlinear frequency generation.

The objective of this dissertation is to investigate and extend the capabilities of high-power VECSELs by utilizing novel nonlinear conversion techniques. Optically pumped VECSELs based on GaAs semiconductor heterostructures have been demonstrated to provide exceptionally high output powers covering the 900 to 1200 nm spectral region with diffraction limited beam quality. The free space cavity design allows for access to the high intracavity circulating powers where high efficiency nonlinear frequency conversions and wavelength tuning can be obtained.

As an introduction, this dissertation consists of a brief history of the development of VECSELs as well as wafer design, chip fabrication and resonator cavity design for optimal frequency conversion. Specifically, the different types of laser cavities such as: linear cavity, V-shaped cavity and patented T-shaped cavity are described, since their optimization is crucial for transverse mode quality, stability, tunability and efficient frequency conversion. All types

of nonlinear conversions such as second harmonic, sum frequency and difference frequency generation are discussed in extensive detail.

The theoretical simulation and the development of the high-power, tunable blue and green VECSEL by the means of type I second harmonic generation in a V- cavity is presented. Tens of watts of output power for both blue and green wavelengths prove the viability for VECSELs to replace the other types of lasers currently used for applications in laser light shows, for Ti:Sapphire pumping, and for medical applications such as laser skin resurfacing. The novel, recently patented, two-chip T-cavity configuration allowing for spatial overlap of two, separate VECSEL cavities is described in detail. This type of setup is further used to demonstrate type II sum frequency generation to green with multi-watt output, and the full potential of the T-cavity is utilized by achieving type II difference frequency generation to the mid-IR spectral region. The tunable output around 5.4 μm with over 10 mW power is showcased. In the same manner the first attempts to generate THz radiation are discussed. Finally, a slightly modified T-cavity VECSEL is used to reach the UV spectral regions thanks to type I fourth harmonic generation. Over 100 mW at around 265 nm is obtained in a setup which utilizes no stabilization techniques. The dissertation demonstrates the flexibility of the VECSEL in achieving broad spectral coverage and thus its potential for a wide range of applications.

Future research consists of utilizing new VECSEL wafer structures to increase the efficiency and output power for deep UV applications and also expand upon the design to achieve broad tunability in the difficult to achieve 8 to 12 μm spectral region. In addition, work will continue to achieve even greater efficiency in the visible region due to the many potential medical applications.

Chapter 1 – Introduction to VECSELs

1.1 Brief history

Semiconductor diode lasers have proven that high output powers covering a wide range of wavelengths can be delivered efficiently in a form of a small device [1]. However, difficulties with simultaneously achieving circular, good beam quality has been their main drawback, which limited their use in many possible applications where a fundamental TEM_{00} laser mode is necessary. The arrival of surface emitting lasers solved the beam quality issue at the price of high output powers. However, in the mid-1990s, vertical external surface emitting lasers were developed as a new semiconductor source of coherent radiation that could provide high output power while maintaining a high quality fundamental transverse mode [2, 3].

In the area of semiconductor lasers, there is a significant distinction between two major device designs: edge emitting [4, 5] and surface emitting [6, 7] lasers, as schematically shown in Figure 1.1. Edge emitting lasers (Figure 1.1a)) use a waveguide structure to confine light to the plane of the semiconductor chip. The cleaved back and front edges of the chip constitute a cavity resonator and the light is emitted from one of the edges. The gain cross-section is typically one × several microns in size, thus resulting in a highly asymmetric laser beam with strong angular divergence which is different for vertical and horizontal planes. In order to achieve high output powers, the waveguide gain area has to be wider to improve the heat dissipation and prevent optical damage [8]. In this manner, very high output powers are achieved [9], albeit while sacrificing the output beam quality – it becomes multimode and very elongated [10, 11].

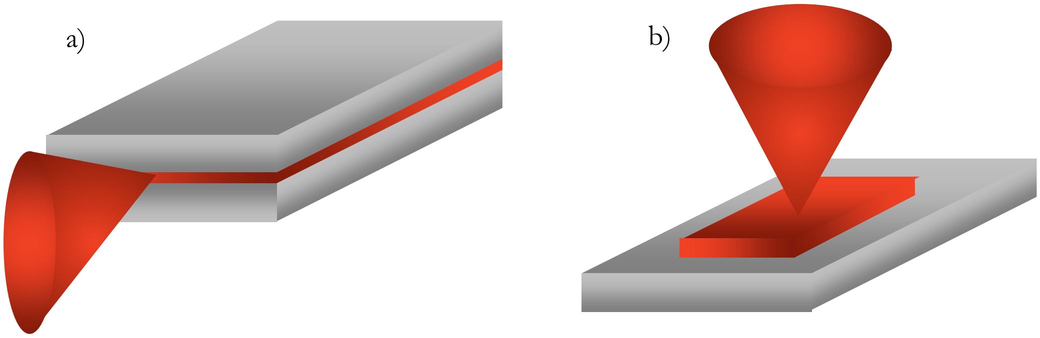

Figure 1.1 Schematics of semiconductor a) edge emitting laser and b) surface emitting laser.

On the other hand, in vertical cavity surface emitting lasers (VCSEL) [6, 7] the resonator cavity axis and thus emitted light are perpendicular to the plane of the laser chip (Figure 1.1b)). Such a design provides a beam with a circular fundamental mode several microns in diameter with low angular divergence. Scaling up power, similarly to edge emitting lasers, requires a larger active area for heat dissipation purposes. But increasing the beam size to tens of microns makes uniform current injection cumbersome and results in multimode transverse outputs. High output powers can be achieved by putting VCSELs into arrays of semiconductor chips [12].

These obstacles had to be overcome to make a high power semiconductor laser delivering the fundamental TEM_{00} output beam. It is clear that the only way to scale up to high output powers was to increase the gain area to hundreds of microns. Since edge emitting lasers cannot provide circular beams, only surface emitting designs could work. The larger beam sizes still resulted in higher order modes, thus a way of controlling transverse modes was required. Having freedom over the cavity geometry design allows one to ensure that the laser will operate with a fundamental transverse mode. Therefore, a laser resonator with additional mirrors would have to be used externally to the semiconductor chip. Hence, the vertical external cavity surface emitting laser (VECSEL) came to be.

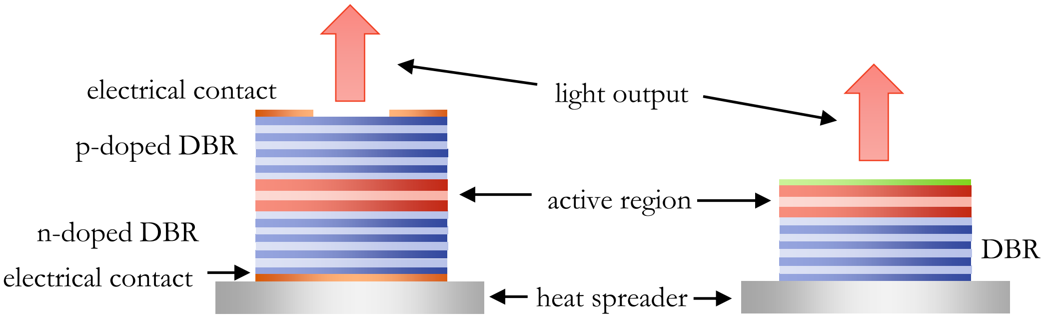

Figure 1.2 Comparison of VCSEL (left) and VECSEL (right) structures.

Because the large gain area has to be excited to achieve high output powers, the other major issue to consider was uniform pumping. Carrier injection could be utilized, but requires a thick doped current spreading layer, which can increase the laser threshold and lower the efficiency [13]. Thus the alternative of using optical pumping became the preferable method. The diode pump lasers with low beam quality and high output power were readily available and were used to pump solid state lasers.

These approaches were combined by Kuznetsov et al. and in 1997 the first VECSEL was demonstrated [2]. The semiconductor structure (see Figure 1.2), compared to a VCSEL, lacked both doped layers, which were necessary for electrical pumping, and the top mirror layer (distributed Bragg reflector), which was replaced by an external output mirror. A basic configuration of a working VECSEL is depicted in Figure 1.3. The optical pump beam is directed onto the semiconductor chip, which is mounted on a heat sink. The heterostructure consists of a gain region and a multilayer high reflectivity mirror, which with the external output coupler mirror makes for the laser resonant cavity. The proper cavity length and radius of curvature (ROC) of the external mirror define the single transverse mode of the laser beam. In the experiment led by Kuznetsov, high output power of $> 0.5\ W$ with a circular fundamental beam was achieved emitted at $\sim 1\ \mu m$ at room temperature. Thus, due to its characteristics, an

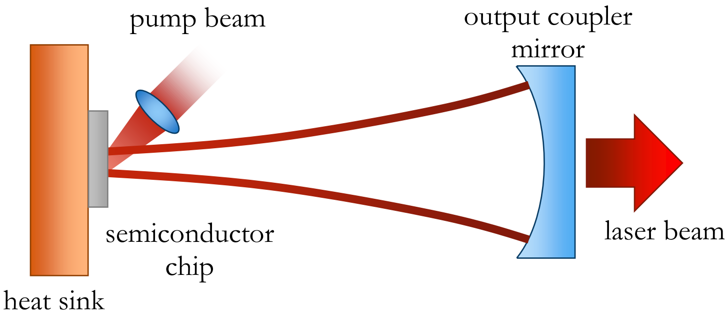

Figure 1.3 Schematic of basic configuration for an optically pumped VECSEL.

optically pumped VESCSEL can be considered a light converter, which uses a high power, low quality multimode pump beam and outputs a high power, high brightness fundamental transverse mode beam with desired spectral properties.

Over the past couple of decades since the first demonstration of VECSELs, they have proven to have many advantageous features, such as high power, good beam quality, and intracavity access, as well as simplified semiconductor wafer growth and chip fabrication. The upward power scaling by simply increasing the optical pump spot diameter resulted in output power of over $100\,W$ [14-16]. The external cavity geometry allows one to utilize various resonator schemes while maintaining diffraction limited transverse beam quality, making for a very flexible laser system [17-19]. Moreover, bandgap engineering using established III–V semiconductor compounds allowed for light emission in spectral regions of $600\,nm - 2.3\,\mu m$ [20-22]. Nowadays, thanks to their advantages, VECSELs are utilized for nonlinear frequency conversion and mode-locking. Intracavity nonlinear generation allows one to reach UV and visible spectral ranges [23-27] as well as long infrared regions [28, 29]. Ultrashort pulse generation was achieved by utilizing semiconductor saturable absorber mirrors (SESAM) [30-34] and self-mode-locking schemes [35, 36]. Other intracavity elements such as birefringent filters and Fabry-Perot etalons were used to obtain single frequency operation [37, 38].

1.2 Principles of operation

1.2.1 Semiconductor structure

The semiconductor band structure illustrated in Figure 1.4 plays a key part in the VECSEL operating scheme. The chip contains a multilayer distributed Bragg reflector (DBR), a gain region made of multiple quantum wells (MQW), and a window layer. The DBR consisting of alternating high and low refractive index quarter wavelength layers makes for one of the laser cavity mirrors. A so called microcavity is defined by the DBR and the semiconductor-air interface. During the optical pumping process, the incident photons are absorbed in pump absorbing barriers. The excited electron-hole pairs then diffuse into the quantum wells. Electron-hole recombination in the quantum wells provides the optical gain. The energy of emitted photons corresponds to the energy gap of quantum wells. The window layer prevents

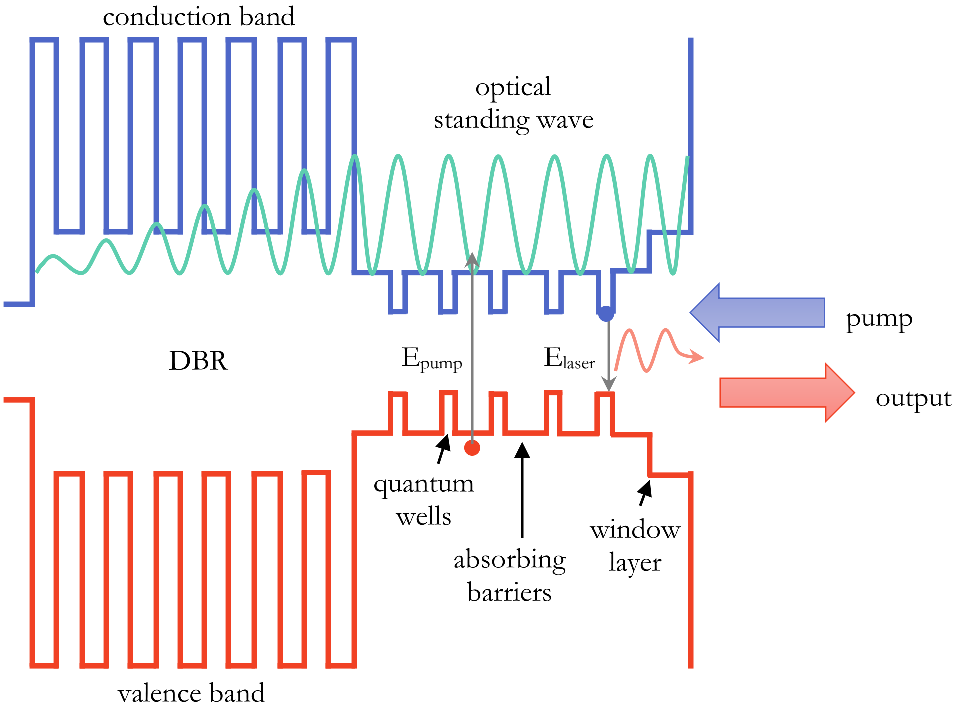

Figure 1.4 Band structure diagram of optically pumped VECSEL.

carriers from diffusing to the semiconductor-air interface, where nonradiative recombination could occur, and also prevents the oxidation of the gain region. In the VECSEL structure design process, the thicknesses of the MQW layers are chosen such that the quantum wells are positioned at the antinodes of the optical standing wave defined by the resonator cavity. This so-called resonant periodic gain (RPG) design allows one to maximize the laser gain [43]. Due to VECSELs nature, the optical gain length is very small, thus the overall intracavity losses should be very low to maintain efficient operation.

1.2.2 Pumping schemes

Even though optically pumped VECSELs are more common, the electrical pumping scheme has been developed as well [44]. As mentioned before, the optical pumping scheme is a straightforward way to obtain a large uniform pump area. Since the gain region is confined by the pump spot, this allows for effective power scaling. With the addition of the external resonator, a high fundamental beam quality can be maintained. Because the pump beam can be low quality, focusing a multimode fiber-coupled diode laser beam onto the VECSEL chip is a simple way to execute optical pumping. Also, since the pumping is purely optical, all of the semiconductor layers can remain undoped, simplifying the structure and thus growth process. Also, the lack of doped and current spreading layers, which have large free carrier absorption, reduces the optical loss. Thanks to the broad absorption band of semiconductors, a wide range of pump sources can be used. Additionally, the high absorption coefficient on the order of $10^4\ cm^{-1}$ makes the single-pass absorption of the pump photons sufficient. On the other hand, because the available high power, low-cost pump sources provide output in $700 - 1000\ nm$ range, developing VECSELs with shorter or longer wavelengths becomes an issue. Due to a large mismatch between pump and emission wavelengths (the so-called quantum defect), the overall efficiency of VECSELs emitting in longer infrared regions is lower. Shorter wavelengths can be reached thanks to nonlinear frequency up conversion. The second major disadvantage of optical pumping is the increased overall footprint of the device due to the external pump's source setup. This decreases the mobility and stability of the system, which may be the limiting factor for VECSELs in some application areas.

For these reasons, research in the electrically pumped VECSELs is still of interest. The lead in the development of electrically pumped VECSELs has been taken by Novalux Inc. and their proprietary NESCEL™ design [44]. The semiconductor structure had to be modified to incorporate a p-n junction, thus it consists of a p-doped high reflectivity DBR layer and a partially reflective n-doped DBR layer which caps the MQW region. This design resulted in $> 500\ mW$ output power at $980\ nm$ [45], thus staying far below the reported powers of optically pumped VECSELs.

1.2.3 Thermal management

Excessive heat, as in any laser, is its greatest weakness, thus effective thermal management is essential for efficient operation. In case of the VECSELs, the major contributor to waste heat is the quantum defect. The energy difference between pump and emitted photons results in generation of waste heat, which has to be efficiently extracted from the gain region. Otherwise, the increased temperature of the active region would allow for the excited carriers to thermally escape from the quantum wells into the barriers, thus reducing the gain and leading to thermal rollover [46]. Since the refractive index is also temperature dependent, heating of the semiconductor layers also leads to spectral shifts of the gain peak and of the microcavity resonance. While in both cases the shift is towards longer wavelengths, the gain peak shifts at a rate of $\sim 0.3\ nm/K$ and is faster than that of the microcavity resonance, which shifts at a rate of $\sim 0.1\ nm/K$ [47]. With a temperature rise, a mismatch between the gain peak and microcavity resonance occurs, thus reducing the gain. This can only be overcome by increased pumping, thus further increasing the temperature, which again can lead to thermal rollover.

High power operation requires efficient heat extraction from the active region to avoid thermal rollover. A heat spreader has to be used to sufficiently remove the waste heat and high thermal conductivity chemical vapor deposition (CVD) diamond is a good choice. Thus, the semiconductor chip is bonded to CVD diamond to efficiently extract heat from the gain region through the DBR region during laser operation.

1.3 Nonlinear frequency conversion

Nonlinear frequency conversion, since the first demonstration of second harmonic generation by Franken, Hill, Peters and Weinreich in 1961 [48], has been a great technique for creating coherent radiation at wavelengths for which gain materials are not available or are of very low efficiency. Since IR semiconductor sources are the most common and efficient, they are used in conjunction with second harmonic or sum frequency techniques to generate shorter wavelengths in the visible or UV spectrum, while difference frequency generation allows for wavelengths in mid-IR or THz range. Recently, well-developed VECSELs based on GaAs/InGaAs semiconductor materials demonstrated that they are capable of providing high power cw output in the $900 - 1200\,nm$ range [14-16]. Their free-space, external cavity combined with optical pumping allows for excellent mode quality control. Access to high circulating power within the cavity allows for high power, efficient new wavelength generation, while additional intracavity elements can be inserted to provide single frequency or tunable operation. Due to this flexibility, the variety of applications for VECSELs can be further expanded thanks to nonlinear frequency conversion.

High power visible lasers are of great interest due to their many possible applications such as fiber communication, spectroscopy, medicine, defense, pump sources and entertainment [49-53]. Previously, the main sources of coherent green and blue light were frequency doubled solid state lasers. The frequency doubled Nd:YAG laser provides output at $532\ nm$ while the frequency doubled Nd:YVO$_4$ laser delivers the output at $457\ nm$. While these type of lasers can deliver around $20\ W$ of continuous wave (cw) output power, the beam quality factor is greater than 2.5 and the tunability is very limited [54, 55]. Thus, these solid state lasers are more renowned for their high average power Q-switched pulsed operation [56]. Nowadays, VECSELs are a viable alternative for laser sources in blue, green, yellow and red spectral regions [24-27].

The visible light spectrum can be further used to achieve UV emission by the means of fourth harmonic generation. Deep-UV high power lasers are of great interest due their applications in atom cooling, eye surgery, and UV microlithography [57-59]. Light generation in the $200\ nm - 300\ nm$ range with a VECSEL as a source of fundamental emission has been demonstrated previously [23] and shows great promise as a high power, tunable UV alternative for solid-state UV lasers.

In recent years, lasers emitting in the long wavelength spectral range have attracted a lot of attention due their possible applications. Sources providing emission in the $4 - 12\ \mu m$ region can be used in areas such as laser surgery, gas detection, or LIDAR, among many others [60-62]. Thus, the development of mid-IR lasers has been driven by the interest they have been gathering. Currently fiber lasers, quantum cascade lasers, lead-salt based lasers, and optical parametric oscillators are capable of coherent radiation in mid-IR spectral band [63-67]. However, due to the complex design, low efficiency, narrow tuning capabilities, and/or the inability to deliver short pulses, their widespread use is limited. Going further to $30 - 1000\ \mu m$, THz waves are becoming yet another radiation range with increased interest. The non-invasive detection and identification of biological and chemical compounds as well as imaging, communications and defense are some among many applications [68-71]. In addition to currently developed THz sources such as quantum cascade lasers, optical parametric diodes and photoconductive antennas, [72-75] new methods of achieving high power, tunable THz emission are welcome. Difference frequency generation can be a technique utilized in two-color VECSELs [76-77] to achieve coherent radiation in the mid-IR and THz spectral range. A low-cost, compact, efficient and continuously tunable coherent radiation source in the desired long wavelength region can be accomplished thanks to nonlinear conversion phenomena.

Chapter 2 – Design and Fabrication of VECSEL chips and Characterization

2.1 Design

The design of the VECSEL semiconductor structure is the first step towards achieving an efficient laser capable of high power output. The active region consisting of quantum wells needs to provide enough gain under optical pumping, while the distributed Bragg reflector has to have high enough reflectivity at the emission wavelength to minimize losses. Moreover, during the whole microcavity design process, thermal effects have to be considered, so the laser can reach its optimal operation. A more detailed description of these key elements can be found below.

2.1.1 Gain region

The gain of the first VECSELs was modeled using a simple phenomenological model, which did not take thermal effects into account. It was based on a quantum well gain with logarithmical dependence on carrier density [78]

$$g = g_0 \ln\left(\frac{N}{N_0}\right) \qquad (2.1)$$

where g_0 is the material gain, N is the carrier density and N_0 is transparency carrier density. The carrier density can be obtained using

$$N = \frac{\eta_{abs} P_p}{h\nu_p N_w L_w A_p} \tau(N) \qquad (2.2)$$

where η_{abs} is the pump absorption efficiency, P_p is pump power, $h\nu_p$ is pump photon energy, N_w and L_w are the number of quantum wells and thickness of each quantum well and A_p is the pump spot area. Here, the carrier lifetime is defined by

$$\frac{1}{\tau(N)} = A + BN + CN^2 \qquad (2.3)$$

where A, B and C are monomolecular, bimolecular and Auger recombination rates, respectively. The above equations can be used to model the threshold pump power and lasing output power, although the thermal rollover cannot be estimated.

One of the methods providing the most complete model of semiconductor structures is the fully microscopic approach. It allows for calculations of laser gain and absorption, photoluminescence, as well as the Auger recombination losses [79, 80]. The model is based on the Bloch equations, the luminescence equations, and Boltzmann scattering equations. This methodology proved to provide successful results when compared with experimental measurements [81, 82].

In addition to accurate design of quantum wells, the resonant periodic gain mentioned in the previous chapter, plays an important role in maximizing the effective gain of the VECSEL active region. The longitudinal confinement factor is expressed as [83]

$$\Gamma_z = \frac{\int^{\int}_{active} E^2(z)dz}{\int_L \, E^2(z)dz} \qquad (2.4)$$

where E is the electric field, the numerator is the integral over the active regions and the denominator is the integral over the whole structure. When the RPG condition is fulfilled with the standing wave antinodes positioned at the QWs, $\Gamma_z \approx 2$ and the effective gain is enhanced

$$g_{eff} \propto \Gamma_z g \qquad (2.5)$$

Since there is a strain mismatch between the QWs and GaAs barrier layers, strain compensating layers have to be used [84]. Thus, to fulfill the RPG requirement, the composition and thickness of each layer have to be carefully selected. See Figure 2.1 for a layer schematic of a typical VECSEL semiconductor structure.

2.1.2 Distributed Bragg reflector

The distributed Bragg reflector is the second part of the VECSEL semiconductor structure. Its design is based on a series of alternating high and low refractive index layers with quarter wave optical thickness. The high reflectivity is obtained thanks to the constructive

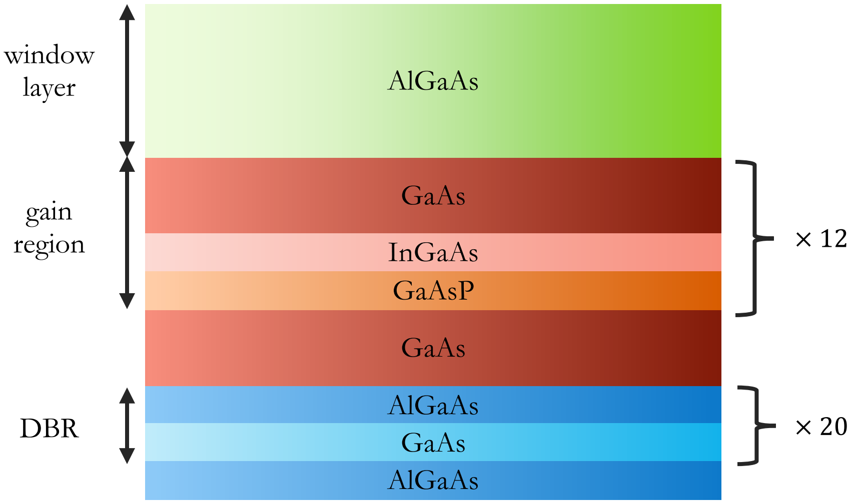

Figure 2.1 Semiconductor layer structure of optically pumped VECSEL chip.

interference at the interfaces of alternating layers. In the case of GaAs based VECSELs, a stack consisting of $20-25$ pairs of GaAs (high index) and AlGaAs (low index) is used to achieve a high reflectivity (HR) ($> 99.9\,\%$) DBR. Figure 2.1 illustrates a DBR structure in a schematic of a full VECSEL semiconductor chip. Since the DBR is a relatively thick layer and separates the active region from the heat spreader, it is a heat barrier. Thus, the overall thickness has to be chosen in a way such that the heat extraction is not compromised.

2.1.3 Optical pumping

Optically pumped VECSELs are the only type employed for experiments in this dissertation. In all cases a high power diode pump laser operating at $808\,nm$ is utilized. A large core diameter high power fiber is used for coupling in the light from the diode bars. The output beam from the fiber is then collimated and refocused onto the VECSEL chip. The pump beam is incident at the angle of $25° - 35°$ to the chip surface. A pair of standard fiber collimator and focusing lenses is used to reimage the pump laser. A set of focusing, collimator lenses and fibers allows us to obtain the desired optical pump spot size diameter on the chip surface, which can be calculated with a simple equation

$$D_{spot} = \frac{f_{foc}}{f_{col}} D_{fiber} \qquad (2.6)$$

where f_{foc} is focusing lens focal length, f_{col} is collimator focal length and D_{fiber} is the fiber core diameter. In most cases spot sizes of $400-600\,\mu m$ in diameter are used.

2.2 Fabrication

The fabrication of VECSEL samples is crucial to the overall performance of the laser. One of the main factors on which laser performance depends is thermal management. To avoid unwanted thermal effects, the heat has to be efficiently extracted from the active region. For this purpose, VECSEL chips are mounted on a chemical vapor deposition diamond heat spreader, which has a high thermal conductivity $> 18\ W/(m \cdot K)$ [85]. Scattering and diffraction losses are the second factor limiting VECSEL performance. Thus, a careful substrate removal process is utilized to provide excellent surface quality as well as the use of the polished CVD diamond with very low surface roughness of $< 50\ nm$ [85].

The VECSEL heterostructures, which are used to fabricate the devices utilized in the experiments presented here, are grown using the so called "bottom emitter" design as shown in Figure 2.2. The name simply refers to the layer growth order, where on top of the GaAs semiconductor substrate an etch stop layer is grown first, followed by the MQW active region and DBR layer.

The full fabrication process for functioning VECSEL chips, which involves metallization, bonding and chemical wet etching, is described in detail below.

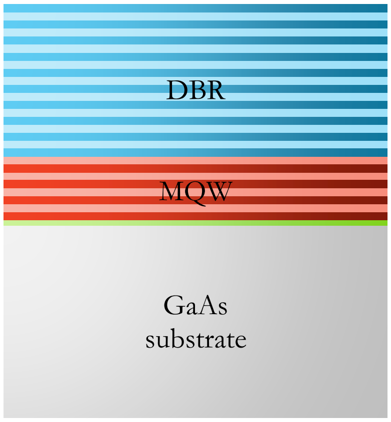

Figure 2.2 "Bottom emitter" design of VECSEL structure.

2.2.1 Metallization

The fabrication process starts with cleaving VECSEL chips from a wafer into about $3-4\,mm^2$ rectangular or square pieces. The high thermal conductivity of the CVD diamond heat spreader is utilized if the thermal impedance between the chip and the diamond is minimized. This requirement is fulfilled by metallizing both VECSEL chips and CVD diamond heat spreaders with thin layers of titanium, gold and indium. The $50\,nm$ titanium layer and $300-400\,nm$ gold layer are deposited using an e-beam evaporation system on the polished CVD diamond and on the DBR side of the cleaved VECSEL chip. When the Ti/Au deposition process ends, the metallized pieces are transferred to a thermal evaporation chamber, where a $6-7\,\mu m$ thick layer of indium is deposited. During an earlier fabrication step, a $50\,\mu m$ thick indium foil was used in the bonding process. Switching to the new indium thermal deposition process allowed us to control and reduce the thickness of the material as well as minimize the number of voids between the chip and heat spreader. The titanium layer on the CVD diamond and semiconductor chip is required as it acts as an adhesive for the gold layer. The gold layer is then needed to form an alloy with indium during the bonding process. This allows for efficient heat extraction from the gain region due to the high thermal conductivity of gold and indium.

2.2.2 Bonding

Before the bonding process starts, the surfaces of the metallized CVD diamond and VECSEL chip are deoxidized in $49\,\%$ hydrochloric acid to ensure that indium surfaces are free of oxidation. Then, the chip is stacked on top of the heat spreader with a weight ($\sim 200\,g$) and placed into a vacuum chamber. The pieces are heated up to a temperature of $\sim 230\,℃$ to melt the indium, thus bonding both pieces together. The slow cooldown period extending over 30 minutes ensures that the sample will not crack due to rapid thermal dimensional changes. Maintaining the whole process under vacuum prevents any new oxidation occurring in the solder layer.

2.2.3 Wet etching

After the VECSEL chip is mounted and bonded to a CVD diamond heat spreader, the process is completed with GaAs substrate removal to reveal the actual VECSEL chip structure. The etch stop layers grown prior to the active region make chemical wet etching the method of choice for substrate removal. The proper composition of the etch stop layers as well as a careful and well controlled etching process prevent any damage to the window or active region layers. The bulk of the $500\ \mu m$ thick GaAs substrate is removed using aggressive, fast, non-selective piranha etchant, which consists of a $1:1:8$ ratio of $98\ \%$ sulfuric acid, deionized water and $30\ \%$ hydrogen peroxide. When less than $100\ \mu m$ of the substrate is left, the etchant is replaced with a slower and selective four parts citric acid and one part H_2O_2 etchant. Thanks to a thin high aluminum content AlGaAs etch stop layer, further etching is prevented. Strongly diluted $5\ \%$ hydrofluoric acid is used to remove the final etch stop layer without affecting the window layer. The finalized VECSEL heterostructure has a surface roughness of less than $30\ nm$ and stands $\sim 6\ \mu m$ tall on top of the bonded diamond heat spreader, realizing the goals of efficient heat extraction and high surface quality.

Figure 2.3 presents the pictures taken at each step of the fabrication process: a) cleaved VECSEL chip and CVD diamond, b) after Ti/Au metallization, c) bonded chip with CVD diamond after indium deposition, d) finished etched VECSEL sample. When the VECSEL

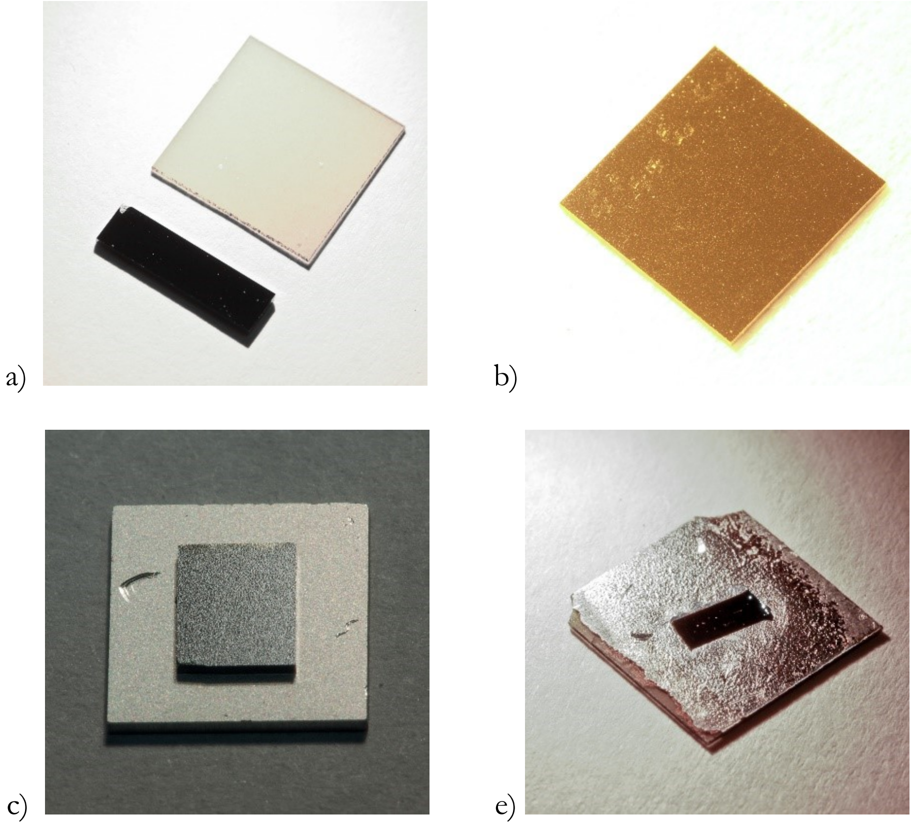

Figure 2.3 Steps of the VECSEL chip fabrication process: a) cleaved VECSEL chip and CVD diamond, b) after Ti/Au metallization, c) chip bonded with CVD diamond after indium deposition, d) finished VECSEL sample after substrate etching.

device is ready to use, it is mounted on a water cooled copper heat sink for temperature control purposes.

In the experiments described in this dissertation VECSEL chips from four wafers with different structure designs were used. Due to their lasing wavelength, they are referred to as $980\ nm$, $1180\ nm$, $970\ nm$ and $1070\ nm$ chips. The latter two come from newer, more optimized wafer designs and thus are characterized with much greater performance.

2.3 Basic characterization

After a VECSEL chip is fabricated, its lasing properties are characterized. The photoluminescence (PL) spectrum, which is determined by the QW emission, DBR, and microcavity, provides information about the VECSEL structure peak gain wavelength. The output power measurements allow us to determine the maximum output power and efficiency of the laser. The obtained lasing spectrum provides information about lasing wavelengths and if it corresponds well to the PL spectrum. In addition, the wavelength tuning measurements give insight about spectral width of the gain. Finally, beam quality measurements ensure proper cavity design for fundamental TEM$_{00}$ mode operation. A picture of the VECSEL setup used for characterization is shown in Figure 2.4. A chip clamped to the copper heatsink is visible as well as the fiber with attached focusing optics and a half-inch curved output coupler mirror.

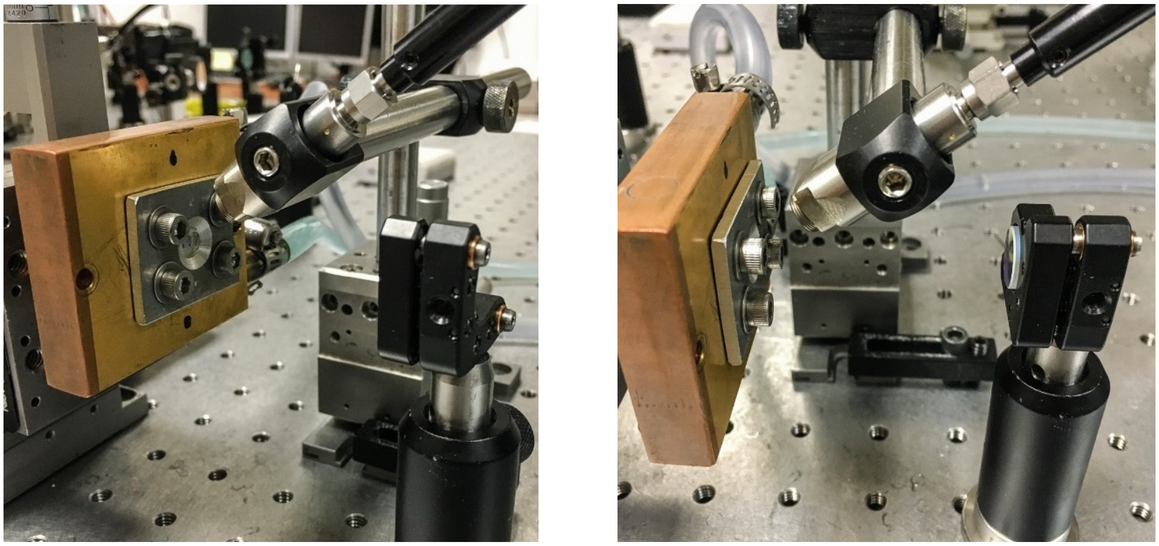

Figure 2.4 VECSEL linear cavity setup used for basic characterization.

2.3.1 Photoluminescence

The PL spectra are taken using a multimode fiber with one end connected to the optical spectrum analyzer (OSA) and the other end placed close, and normal, to the VECSEL chip surface. The spectra are captured at different pump powers to observe the gain peak shift. Figure 2.5 is an example of a surface PL spectra taken for a $1070\ nm$ chip at a few pump power levels. The two peaks at $\sim 1020\ nm$ and $\sim 1065\ nm$ correspond to microcavity resonances, while the small bump at $\sim 1045\ nm$ comes from the QWs gain peak. It is noticeable that at the lowest pump power the gain peak wavelength is at a shorter wavelength, whereas at high pump power the peak is red-shifted. This difference in wavelength between the low and high pump power peaks is called the detuning and it is purposefully incorporated into the VECSEL design. As mentioned previously, the spectral shift for the gain region varies differently from one for the microcavity resonance. The initial detuning allows for the gain peak to align with microcavity resonance at high pump power, thus the high output power lasing can occur before thermal rollover.

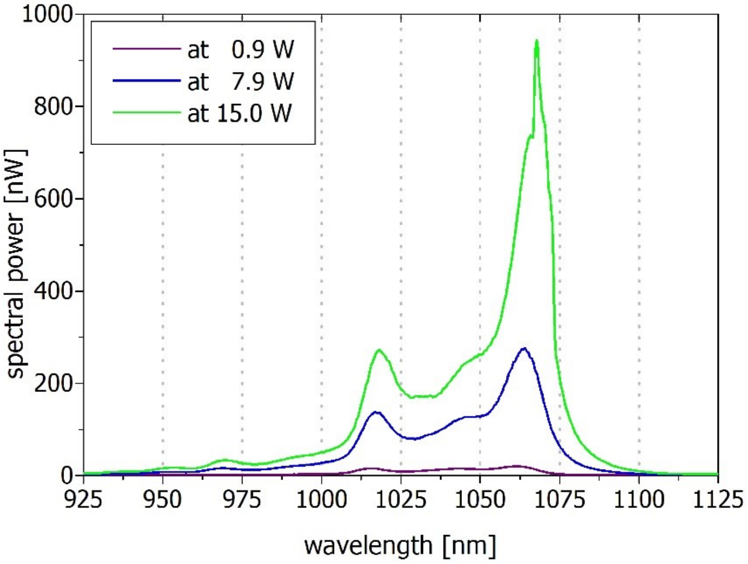

Figure 2.5 Surface PL spectra at different pump power levels.

2.3.2 Output power

The output power characterization is usually performed using the linear cavity VECSEL geometry. A curved mirror with transmission of $2-6\,\%$ serves as the output coupler (OC). Figure 2.6 presents an example of such measurements. The output power is plotted against the optical pump power absorbed on the chip at various temperatures of the copper heat sink. The lasing threshold is seen in the graph. As the temperature rises, the lasing threshold drops, but at the cost of the slope efficiency. This is caused by the initial gain detuning mentioned in the previous section. The slope and optical efficiencies can be calculated based on the acquired data. For a heatsink temperature of $15℃$, over $9.5\,W$ of output power was achieved for a $\sim 550\,\mu m$ diameter spot size and $3\,\%$ transmission $25\,cm$ ROC OC. The slope efficiency was ~44% and the optical efficiency at maximum power was $\sim 36\,\%$.

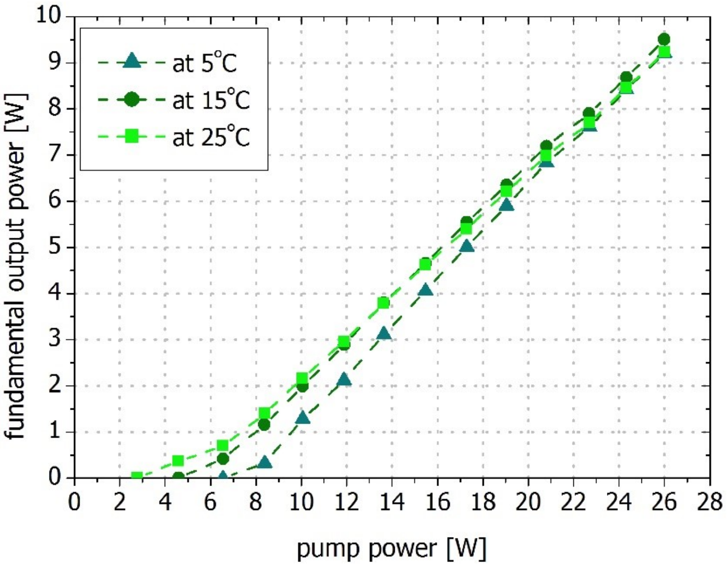

Figure 2.6 Output power at different heat sink temperatures from linear cavity with $3\,\%$ transmission output coupler.

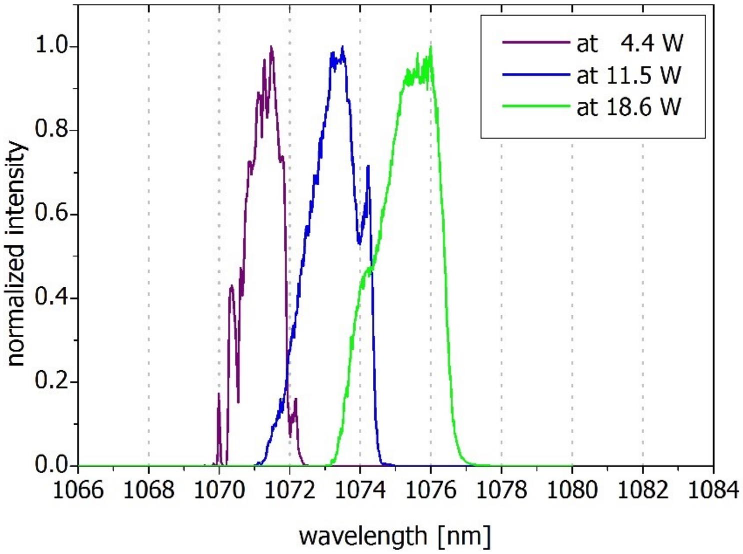

Figure 2.7 Lasing spectra at different pump powers from linear cavity.

2.3.3 Lasing spectra

The lasing spectra are measured in a similar manner to the PL spectra, but the fiber tip is placed in the beam path after the OC. A plot with spectra captured at different pump powers is shown in Figure 2.7. The lasing spectra correspond well with the previously collected PL spectra. Also, as expected, there is a red shift of several nanometers between the lasing wavelength peaks as the pump power rises.

2.3.4 Intracavity wavelength tuning

The two most common elements used for intracavity wavelength tuning are a Fabry-Perot etalon and a birefringent filter (BF). A brief explanation of their operating principles will be described below, starting with the etalon.

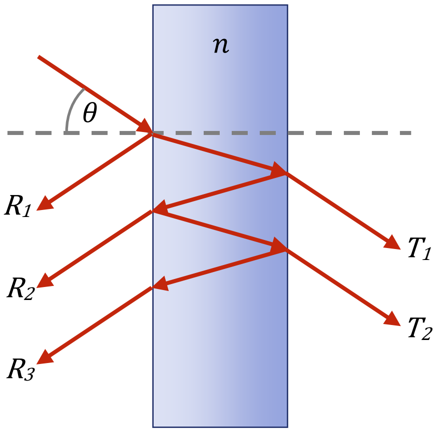

Figure 2.8 Schematic of light beam paths in a Fabry-Perot etalon.

A Fabry-Perot etalon consists of two optically flat partially reflective parallel surfaces separated by a certain distance [86], as illustrated in Figure 2.8. A light beam incident at angle θ on the first surface is partially reflected. The transmitted beam passes through the medium with refractive index n and is partially reflected of the second surface. With each round trip path of the beam, some light is reflected back and some is transmitted through the etalon. Due to these multiple reflections, a constructive interference occurs if the beams are in phase. As a result, the etalon transmission has high intensity peaks, which are described by a transmission function

$$T = \frac{(1-R)^2}{1+R^2-2R\cos\delta} \qquad (2.8)$$

where R is the surface reflectance and the phase difference upon each reflection is

$$\delta = \left(\frac{2\pi}{\lambda}\right) 2nL\cos(\theta) \qquad (2.9)$$

The etalon free spectral range (FSR) is defined by the separation between the adjacent transmission peaks, thus

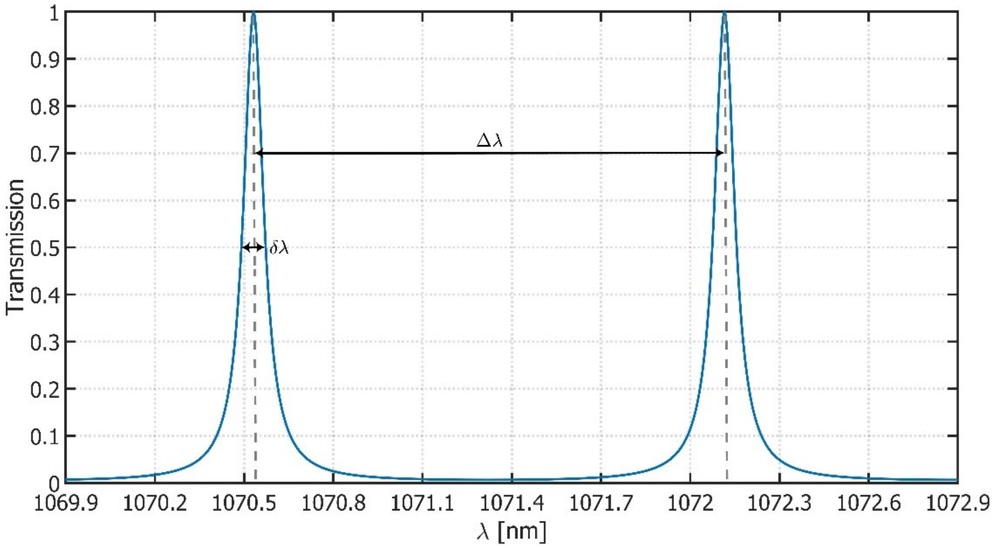

Figure 2.9 Transmission calculated for a $250\ \mu m$ thick fused silica etalon with $85\ \%$ reflectivity coatings on both facets.

$$FSR = \Delta\lambda = \frac{\lambda_0^2}{2nL\cos(\theta) + \lambda_0} \qquad (2.10)$$

where λ_0 is a nearest peak central wavelength. The commonly used parameter for describing an etalon is the finesse defined as

$$\mathcal{F} \approx \frac{\pi\sqrt{R}}{1-R} \qquad (2.11)$$

and it relates the FSR to the full width half maximum (FWHM = $\delta\lambda$) of the peak

$$\mathcal{F} = \frac{\Delta\lambda}{\delta\lambda} \qquad (2.12)$$

The transmission of a $250\ \mu m$ thick fused silica glass slide with $85\ \%$ reflectivity coatings on both facets serving as a Fabry-Perot etalon is shown in Figure 2.9. The linewidth of the peaks strongly depends on the finesse; the FSR and FWHM are marked on the graph.

The other common method of laser tuning is with the use of a birefringent filter. In the simplest case, the filter consists of a plate made of a uniaxial crystal (e.g. quartz) with its optical axis oriented parallel to the surface of the plate [87]. It is inserted into the cavity at Brewster's angle to the beam propagation direction, thus each of the plate surfaces acts as a partial linear polarizer. The ordinary and extraordinary components of the beam will experience different phase shifts

$$\Delta\phi = \frac{2\pi}{\lambda}(n_e - n_o)L \qquad (2.13)$$

where n_e and n_o are extraordinary and ordinary refractive indices, λ is the wavelength and L is the plate thickness along the beam. Then the transmission function is equal to

$$T = 2\cos^2\left(\frac{\Delta\phi}{2}\right) \qquad (2.14)$$

Now, the beam does not suffer any loss from the BF under the following condition

$$\Delta\phi = \frac{2\pi}{\lambda}[n_e(\theta')\cos(\theta_e) - n_o\cos(\theta_o)]d = 2m\pi \qquad (2.15)$$

where θ' is the angle between the direction of propagation and optical axis, θ_e and θ_o are the extraordinary and ordinary rays refraction angles inside the plate and d is plate thickness. Rotating the BF around its normal effectively changes the refractive index seen by extraordinary ray, thus shifting the peaks of the transmission function. In this way the VECSEL emission wavelength can be tuned. Moreover, the BF plate thickness determines the FSR and FWHM. A thinner plate will result in long FSR and wide FWHM, while a thicker one will provide shorter FSR and narrower FWHM. An example of a VECSEL tuned with BF is

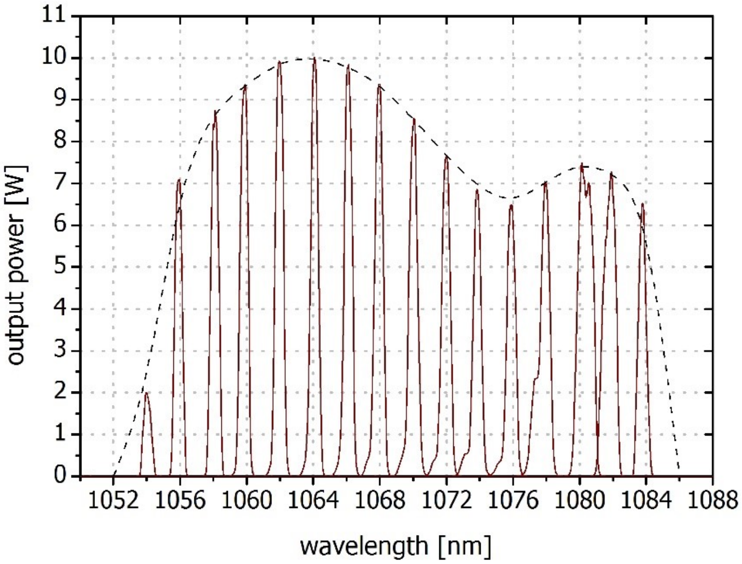

Figure 2.10 Wavelength tuning using a $2\ mm$ thick BF inserted in a linear cavity.

presented in Figure 2.10. A $2\ mm$ thick BF was placed intracavity and rotated. Every $1\ nm$ the optical spectrum was captured and the output power was measured. On the graph each spectral peak is normalized to the output power achieved at this wavelength and the dashed line marks the overall tuning trend.

2.3.5 Beam quality

The process of measuring the beam quality is described in detail in Chapter 3.5. Here, in Figure 2.11, is presented an example of measured beam properties. The computer software delivered with the scanning slit beam profiler DataRay Beam Map2 [88] allows us to determine the beam divergence, the M^2 beam quality factor, as well as the simulated image of the beam shape. Here, the average M^2 was ~ 1.29 for an output power of $\sim 9\ W$.

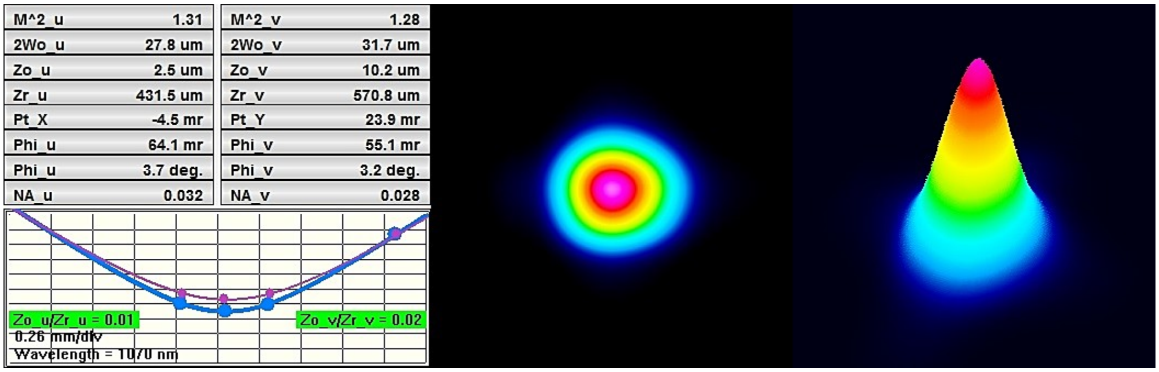

M^2_u	1.31	M^2_v	1.28
2Wo_u	27.8 um	2Wo_v	31.7 um
Zo_u	2.5 um	Zo_v	10.2 um
Zr_u	431.5 um	Zr_v	570.8 um
Pt_X	-4.5 mr	Pt_Y	23.9 mr
Phi_u	64.1 mr	Phi_v	55.1 mr
Phi_u	3.7 deg.	Phi_v	3.2 deg.
NA_u	0.032	NA_v	0.028

Zo_u/Zr_u = 0.01

Zo_v/Zr_v = 0.02

0.26 mm/div

Wavelength = 1070 nm

Figure 2.11 Measured beam quality, divergence and 3D beam profile.

Chapter 3 – VECSEL Resonator Cavity Design and Optimization

3.1 ABCD matrix and Gaussian beam q-parameter for cavity design

The resonant laser cavity geometry plays a crucial role in VECSELs efficient operation and flexibility. The choice of the size of the optical pump beam on the chip, mirror curvatures and distances between the cavity elements gives the freedom of design to obtain fundamental TEM_{00} mode lasing. This mode which propagates within the cavity is most desirable due to its high brightness and diffraction limited properties. The optical pump spot size determines the area of the gain being utilized for lasing but does not ensure the TEM_{00} mode operation. Therefore, higher order modes, or more than one mode, can be maintained in the cavity. By considering the cavity parameters in the design so that the calculated fundamental transverse mode diameter is slightly smaller than that of the optical pump spot, the optimal beam quality can be achieved.

We typically consider Gaussian beams propagating inside a laser resonator. This allows us to utilize a universal approach known as ABCD ray transfer matrix analysis to design the cavity [89]. In this method, an entering ray x_1 is considered as it passes through an optical element

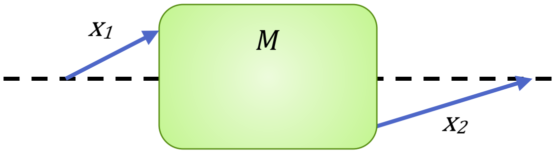

Figure 3.1 Schematic of the ABCD ray transfer matrix method.

described by a 2×2 matrix M. This matrix transforms the entry ray x_1 into exiting ray x_2. This concept is schematically shown in Figure 3.1. The correlation between the entry and exit rays is described by the following formula

$$\vec{x}_2 = \begin{bmatrix} x_2 \\ x_2' \end{bmatrix} = \begin{pmatrix} A & B \\ C & D \end{pmatrix} \times \begin{bmatrix} x_1 \\ x_1' \end{bmatrix} = M\vec{x}_1 \qquad (3.1)$$

where x_i and x_i' are the position and the slope of the ray, respectively. The equation is not limited to a single element case and the total ABCD matrix M can be a product of several single optical element M_n matrices, such that

$$M = M_n M_{n-1} \cdots M_2 M_1 \qquad (3.2)$$

Thus an arbitrary number of optical elements can be used as long as they can be suitable described by a ray matrix. The ray transfer matrices are predefined for simple optical components, thus the calculations remain fairly simple. The propagation of a beam through a medium of thickness t and constant refractive index n is described by

$$\begin{pmatrix} 1 & \frac{t}{n} \\ 0 & 1 \end{pmatrix} \qquad (3.3)$$

For refraction at an interface with radius of curvature R from a medium with refractive index n_1 transmitted into a medium with refractive index n_2 the matrix is equal to

$$\begin{pmatrix} 1 & 0 \\ \frac{n_1 - n_2}{R} & \frac{n_1}{n_2} \end{pmatrix} \qquad (3.3)$$

Reflection from a surface with radius of curvature R at an angle θ is described by

$$\begin{pmatrix} 1 & 0 \\ -\frac{2}{R_e} & 1 \end{pmatrix} \qquad (3.4)$$

where $R_e = R\cos\theta$ is the effective radius of curvature in the tangential plane and $R_e = R/\cos\theta$ is the effective radius of curvature in the sagittal plane. In addition to these matrices, the q-parameter is used to describe a beam with a fundamental Gaussian mode [89]

$$\frac{1}{q} = \frac{1}{R} - j\frac{\lambda}{\pi w^2} \qquad (3.5)$$

which is complex, with R the radius of curvature of the mode wavefront, w the radius of the mode (beam radius or size) and λ the wavelength of the propagating light. Based on the (3.5) it is noticeable that the wavefront radius of curvature relates to the real part of the q-parameter and mode radius to the imaginary part. Putting everything together, the Gaussian beam q_1 transformed by a complex system described by M will result in

$$q_2 = \frac{Aq_1 + B}{Cq_1 + D} \qquad (3.6)$$

In any design of a laser cavity, a stable resonator is required – the fundamental beam should remain unchanged after a single roundtrip. Thus, the input and output q-parameters have to be equal to each other such that

$$q_1 = \frac{Aq_1 + B}{Cq_1 + D} \qquad (3.7)$$

where A, B, C and D are elements of the M matrix describing one cavity roundtrip. Finding the roots for this equation and separating the imaginary part from the real part yields the solution for the beam radius

$$w = \sqrt{\frac{\lambda}{\pi}|B|\frac{1}{\sqrt{4-(A+D)^2}}} \qquad (3.8)$$

The beam radius has a special case where the Gaussian beam contracts to a minimum diameter and the wavefront becomes a plane ($R = \infty$). This is called a beam waist which has a diameter of $2w_0$. Moreover, one can ensure that the designed cavity is stable by making sure that the values of the ABDC transfer matrix fulfill the requirement

$$-1 < \frac{A+D}{2} < 1 \qquad (3.9)$$

A full description of any type of resonant cavity can be obtained from above equations, thus allowing the modeling of a large variety of VECSEL geometries. These various geometries will be examined in the following sections.

3.2 Linear cavity

The most basic resonator geometry for a VECSEL is a linear cavity as shown in Figure 3.2. A gain chip makes for a plane mirror and the cavity is enclosed by a curved mirror with radius of curvature R. Figure 3.3 shows the fundamental mode for Gaussian beam propagation in this type of cavity calculated in Matlab. It is noticeable from the figure that the beam waist is

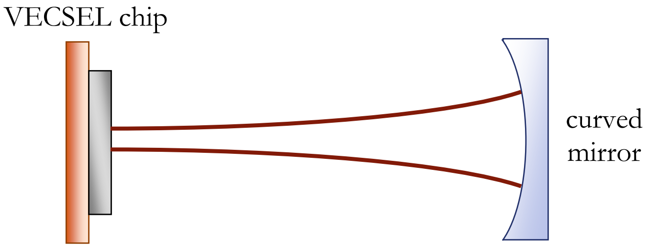

Figure 3.2 Schematic of a linear cavity VECSEL.

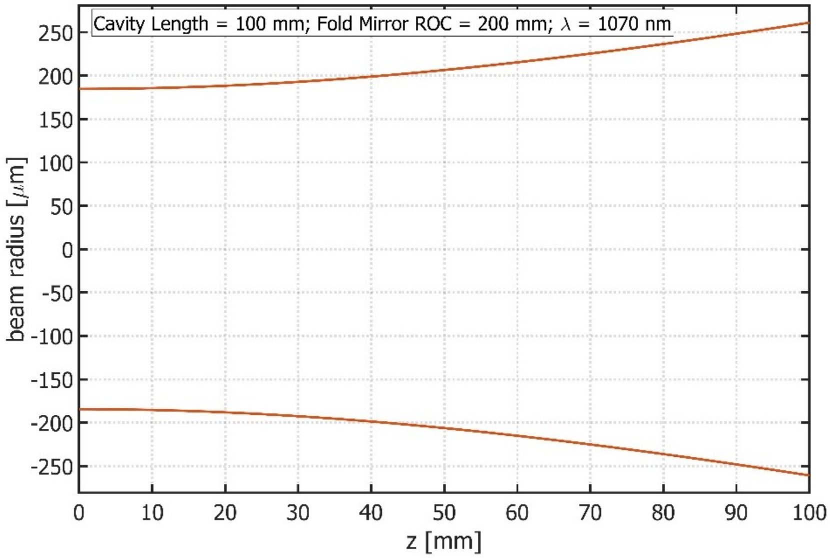

Figure 3.3 Gaussian beam propagation in a $10\ cm$ long linear cavity with $20\ cm$ ROC mirror.

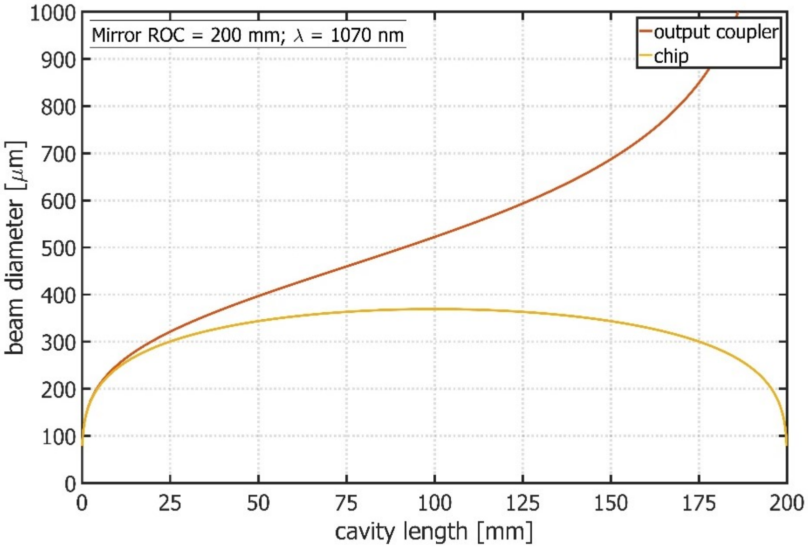

Figure 3.4 Beam size dependence on the linear cavity length with $20\ cm$ ROC fold mirror.

located at the chip DBR, since there has to be a plane wave at the flat mirror surface, and the beam diverges towards the curved mirror. Figure 3.4 depicts the dependence of the beam waist size at the chip surface and beam diameter on the curved mirror as the cavity length L changes. While the beam waist diameter on the chip has its maximum at $L = R/2$, the spot size on the mirror gets larger as the cavity length increases. Also, the cavity becomes unstable if $L > R$, resulting in the fundamental mode not being supported. Linear cavities are most commonly used for basic characterization of the VECSEL chips such as output power and lasing spectra.

3.3 V-cavity

Another type of a resonator commonly used with VECSELs is a so-called V-folded cavity (V-cavity), as shown in Figure 3.5. This cavity geometry is based on a VECSEL chip and two mirrors out of which at least one mirror is curved. Usually the curved mirror is the fold mirror and allows refocusing of the beam onto the end flat mirror. However, since the fold happens on the curved mirror, astigmatism is introduced and the Gaussian beam has both tangential (horizontal) and sagittal (vertical) components. Due its V shape, the cavity can be divided into two arms: the first arm between the chip and the fold mirror and the second arm between the fold mirror and the flat mirror. At first glance this geometry seems simplistic, however, this cavity provides huge flexibility on obtainable spot sizes on both the chip and the flat mirror. A full picture of how the spot sizes change with respect to the resonator arms lengths is shown in Figure 3.6. It is noticeable that there are some restrictions on distances between the cavity

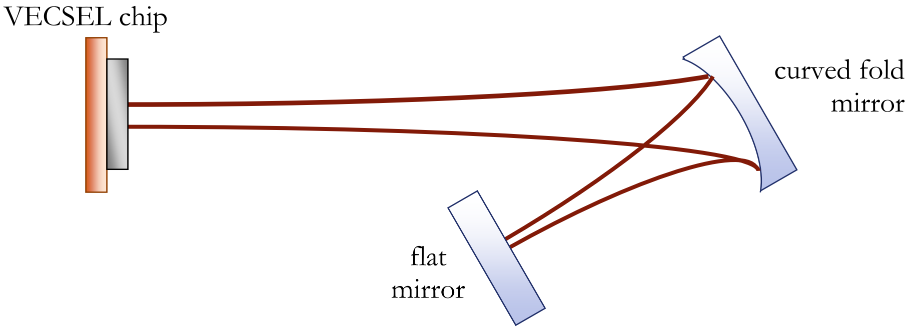

Figure 3.5 Schematic of a V-folded cavity VECSEL.

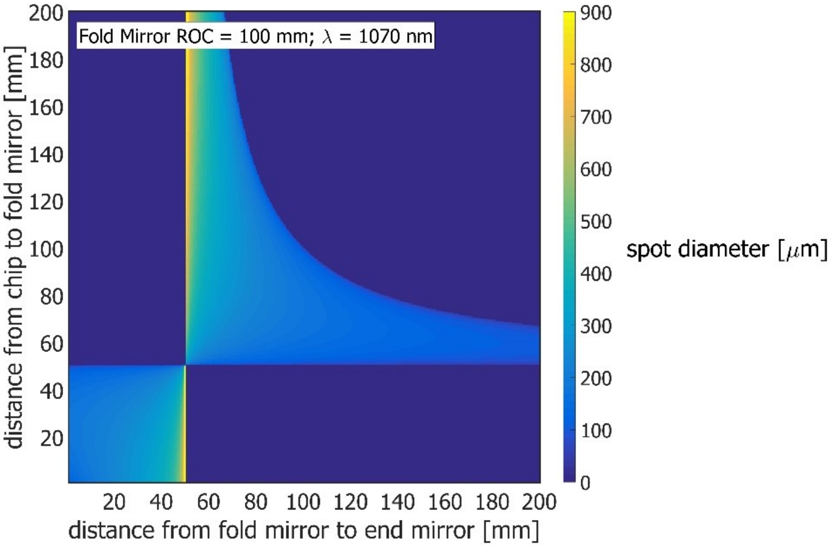

Figure 3.6 Spot size variation vs. arms lengths in V-cavity with $10\ cm$ ROC fold mirror.

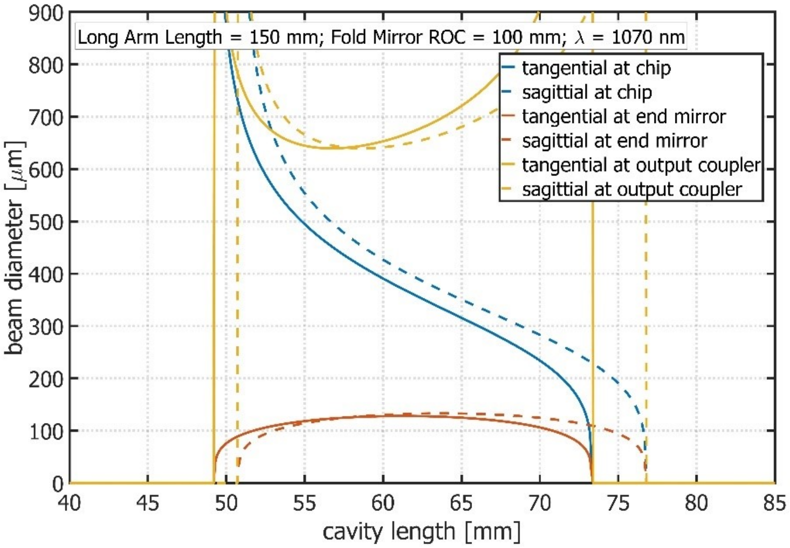

Figure 3.7 Spot sizes variation vs. one arm length change when the other arm length is fixed in a V-cavity with $10\ cm$ ROC fold mirror.

elements to maintain the system stability. The most striking feature is that there are asymptotes at $R/2$ which are the cutoffs for a stable resonator if one of the arm lengths is less than this value. The other characteristic clearly noticeable is that if one arm becomes longer, the choices for the second arm length become limited. The distance from the chip to the fold mirror has a great influence on the spot diameter on the end mirror, while the distance from the fold mirror to the end mirror mostly affects the spot size on the chip. This can be seen if the spot size variation is plotted against one arm length, while the other length is fixed, as presented on Figure 3.7. Here, the first arm is fixed and the dependence is shown with respect to the second arm. While the spot size on the end mirror varies slightly through most of stability region, the beam diameter at the chip sees a great change and becomes smaller for larger distances. Finally, a simulation of a Gaussian beam propagating in a V-cavity is shown in Figure 3.8. The location of the fold mirror is clearly demonstrated by the noticeable refocusing of the beam. As mentioned before, there is a difference between beam radii of the tangential and sagittal modes of the Gaussian beam due to the non-zero fold angle at the curved mirror. This difference is shown in Figure 3.8 for propagation through the cavity. In the most common case, one of the arms is much longer than the other, which is due to the most common application of V-cavity VECSEL: nonlinear frequency conversion [24-27]. A large beam diameter on the chip allows

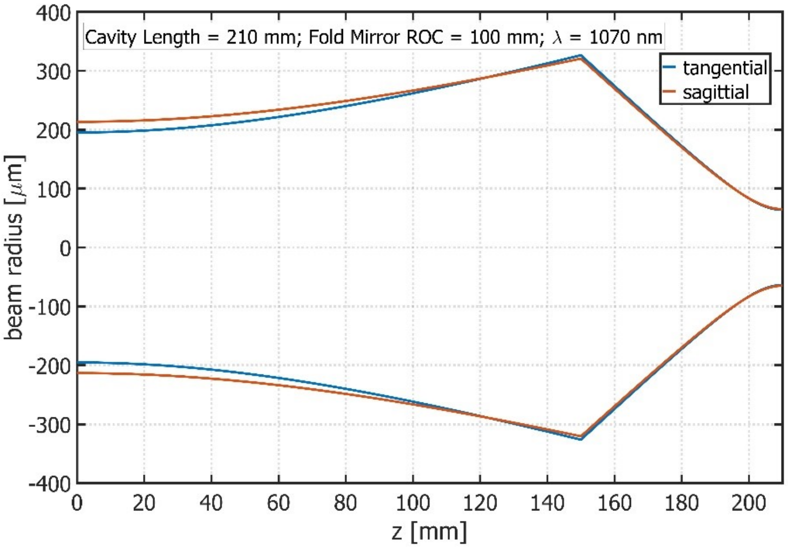

Figure 3.8 Gaussian beam propagation in V-cavity with 15 cm and 6 cm long arms, and 10 cm ROC fold mirror.

for utilization of a lot of gain area, while the small spot size on the nonlinear crystal positioned near the end mirrors ensures efficient conversion.

3.4 T-cavity

A patented T-cavity VECSEL [90] design utilizes two VECSEL chips lasing in a linear or V-cavity configuration, but merged into one setup by incorporating an intracavity polarizing beam splitter (PBS) or dichroic mirror. A simple T-cavity schematic is demonstrated in Figure 3.9. A lasing mode in the first cavity passes through a PBS or a dichroic mirror, while the second cavity is bent due to the reflection of said PBS (dichroic mirror). This results in a resonator geometry which consists of three distinct regions: two regions where the circulating modes from both chips are independent and one where those circulating beams are merged and collinear. The design and simulations of a T-cavity remain the same, because both VECSEL chips constitute the individual cavities. This VECSEL configuration provides collinear dual wavelength operation with access to the intracavity circulating power making it most suitable for nonlinear frequency conversion. While there are other means to obtain two

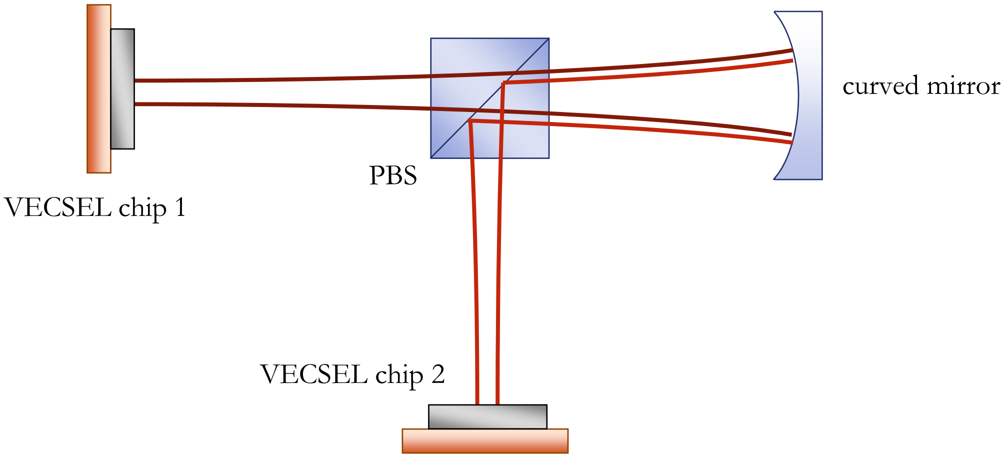

Figure 3.9 Schematic of a simple T-cavity VECSEL.

wavelength emission, such as an intracavity etalon for lasing mode selection or a gain medium engineered for quantum well emission at two different wavelengths [91, 92], the T-cavity allows for broadband tuning and freedom of lasing wavelength separation [77]. In case of the small wavelength separation the PBS is used in the cavity making the collinear beam's polarizations orthogonal, thus allowing for type II sum or difference frequency generation. If the wavelength separation is greater than $\sim 100\,nm$, a dichroic mirror designed for the lasing wavelengths is preferable. The collinear beam's polarizations can be the same or orthogonal, thus type I or II sum or difference frequency generation is possible.

3.5 Beam quality measurements

The quality of a laser beam is measured to ensure good TEM$_{00}$ mode operation. To qualitatively describe the beam quality, the M^2 factor is used, which can be defined as the ratio of a real beam to the ideal perfect Gaussian beam [93]. The most common methods of

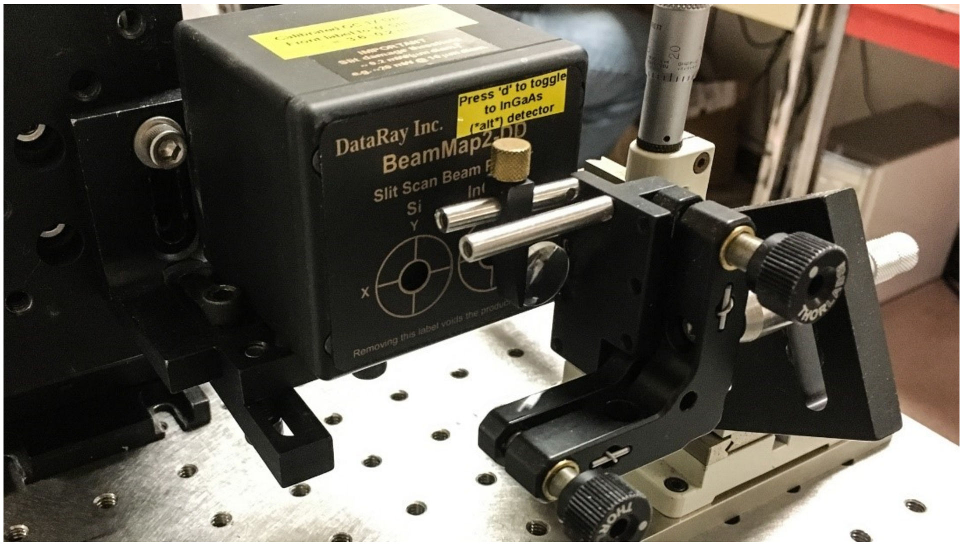

Figure 3.10 DataRay Beam Map2 scanning slit beam profiler setup used to characterize the beam quality.

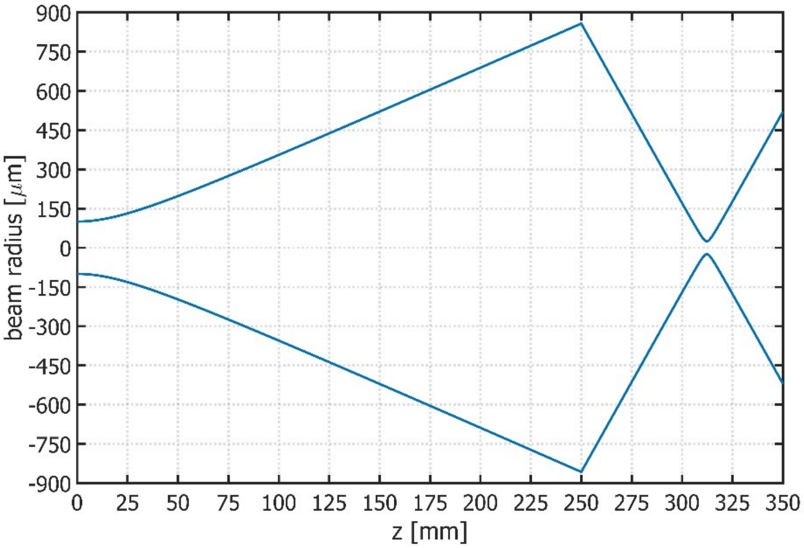

Figure 3.11 Gaussian beam propagation and focusing with $50\ mm$ into the DataRay Beam Map2 scanning slit beam profiler.

measuring M^2 values are by using a beam profiling CCD camera or a scanning slit beam profiler. For the purposes of this research, a DataRay Beam Map2 scanning slit beam profiler was used due to its high resolution and broad range of operating wavelengths from $190 - 2500\ nm$ [88]. There are certain restrictions on the power density allowed into the profiler, which along with beam power attenuation, need to be considered so the measurements will not be erroneous. Thus, the beam profile characterization cannot be done at very high output powers, and the power is ordinarily maintained below $15\ W$. Figure 3.10 shows a photo of the setup used to perform the measurements. The beam waist of a lasing mode has to be refocused into the beam profiler using a preferably short focal length lens to obtain a small beam diameter and large divergence at the device, which is required by the beam profiler to ensure an accurate measurement. A simple simulation of the beam propagation was calculated in Matlab, as presented in Figure 3.11, to make sure the chosen lens and distances were correct. The software provided with the device gathered all of the beam parameters and calculated the M^2 values. The beam profiles of visible and infrared lasing modes can be characterized this way, and in the case of the T-cavity, the collinear emission and mode overlap can be confirmed.

Chapter 4 – Nonlinear Frequency Conversion with Gaussian Beams

---

4.1 Review of Nonlinear Optical Processes

Nonlinear optical phenomena are the consequence of high intensity light interacting with a material and modifying its optical properties. Since the first demonstration of second harmonic generation (SHG) by Franken, Hill, Peters and Weinreich in 1961 [48], nonlinear optics became its own field of grand scale, with many of applications [94]. Nonlinear frequency conversion turned out to be a way to develop laser sources with emission in spectral ranges for which the material gain does not exist or is of very low efficiency. For example, frequency doubled and quadrupled solid state Nd:YAG lasers became sources for green ($532\,nm$) and UV ($266\,nm$) light which are being used in areas such as medical surgeries, dermatology and ophthalmology [95-97]. With respect to VECSELs, their open cavity design and high intensity circulating light fields, have made them become a great platform for nonlinear frequency conversion.

Nonlinear effects are described by the dependence of the material polarization $P(t)$ on the strength of the applied optical field $E(t)$ [94, 98]. In the case of the linear processes, the induced polarization is linearly related to the optical field strength and can be described by

$$P(t) = \epsilon_0 \chi^{(1)} E(t) \qquad (4.1)$$

where ϵ_0 is free space permittivity and $\chi^{(1)}$ is linear susceptibility. In nonlinear optics, this equation is generalized by expressing polarization as a power series in the field strength

$$P(t) = \epsilon_0\left[\chi^{(1)}E(t) + \chi^{(2)}E(t) + \chi^{(3)}E(t) + \cdots\right]$$
$$\equiv P^{(1)}(t) + P^{(2)}(t) + P^{(3)}(t) + \cdots \qquad (4.2)$$

where $\chi^{(2)}$ and $\chi^{(3)}$ are the second- and third-order nonlinear susceptibilities. $P^{(2)}(t)$ and $P^{(3)}(t)$ are referred to as second- and third-order nonlinear polarizations. Polarization can be split into the linear and nonlinear components

$$\vec{P} = \vec{P}^{(1)} + \vec{P}^{NL} \qquad (4.3)$$

Since the nonlinear frequency conversion processes are of second-order, only the second-order polarization and susceptibility values are considered, because $P^{(3)}(t)$ is very small.

Light propagating in a nonlinear medium can be described with the wave equation. We start with the Maxwell's equations for a medium containing no free charges and no free currents

$$\nabla \cdot \vec{D} = 0 \qquad (4.4)$$

$$\nabla \cdot \vec{B} = 0 \qquad (4.5)$$

$$\nabla \times \vec{E} = -\frac{\partial \vec{B}}{\partial t} \qquad (4.6)$$

$$\nabla \times \vec{H} = \frac{\partial \vec{D}}{\partial t} \qquad (4.7)$$

Then the wave equation can be derived from the above equations and is written as

$$\nabla^2 \vec{E} - \frac{\epsilon^1}{c^2}\frac{\partial^2 \vec{E}}{\partial t^2} = \frac{1}{\epsilon_0 c^2}\frac{\partial^2 \vec{P}^{NL}}{\partial t^2} \qquad (4.8)$$

where ϵ^1 is a scalar dielectric tensor and c is the speed of light. This equation can be used to describe the specific nonlinear conversions and has to be satisfied for all frequency components.

4.1.1 Sum Frequency Generation

A schematic of sum frequency generation (SFG) and its energy diagram are presented in Figure 4.1. All of the waves are propagating in the same direction z. Two incident waves with frequencies ω_1 and ω_2 are interacting with a medium with nonlinear coefficient d_{eff} and length L, which results in a sum frequency output wave with frequency ω_3. The amplitudes of the waves can be described with a slowly varying function of z and are denoted as $A_j(z)$, where $j = 1,2,3$. The electric field of the sum frequency wave is described by

$$E_3(z,t) = A_3 e^{i(k_3 z - w_3 t)} \tag{4.9}$$

and the polarization is equal to

$$P_3(z,t) = 4\epsilon_0 d_{eff} A_1 A_2 e^{i[(k_1+k_2)z - \omega_3 t]} \tag{4.10}$$

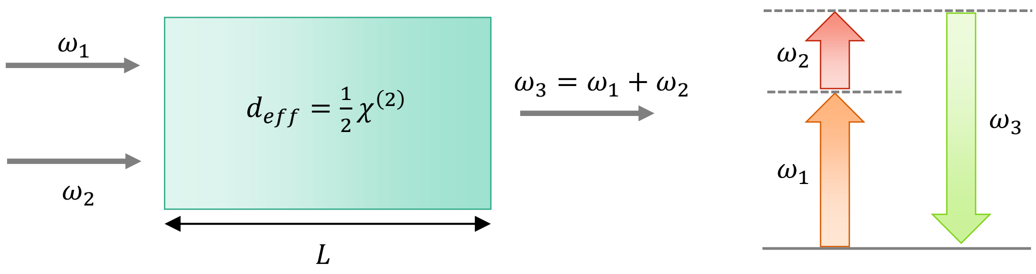

Figure 4.1 Sum frequency generation schematic and its energy diagram.

where

$$k_1 = \frac{n_1 \omega_1}{c} \text{ and } n_1 = \sqrt{\epsilon^{(1)}(\omega_1)} \qquad (4.11a)$$

$$k_2 = \frac{n_2 \omega_2}{c} \text{ and } n_2 = \sqrt{\epsilon^{(1)}(\omega_2)} \qquad (4.11b)$$

$$k_3 = \frac{n_3 \omega_3}{c} \text{ and } n_3 = \sqrt{\epsilon^{(1)}(\omega_3)} \qquad (4.11c)$$

The above equations are plugged into the wave equation, which then is solved by utilizing the slowly varying amplitude approximation. As a result, three coupled amplitude equations are obtained

$$\frac{dA_1}{dz} = \frac{2id_{eff}\omega_1^2}{k_1 c^2} A_3 A_2^* e^{-i\Delta kz} \qquad (4.12)$$

$$\frac{dA_2}{dz} = \frac{2id_{eff}\omega_2^2}{k_2 c^2} A_3 A_1^* e^{-i\Delta kz} \qquad (4.13)$$

$$\frac{dA_3}{dz} = \frac{2id_{eff}\omega_3^2}{k_3 c^2} A_1 A_2 e^{-i\Delta kz} \qquad (4.14)$$

where

$$\Delta k = k_1 + k_2 - k_3 \qquad (4.15)$$

is the wavevector mismatch or momentum conservation equation.

The intensity of the ω_3 wave can be simply calculated if the amplitudes A_1 and A_2 are considered constant. The integration of the (4.14) and replacing amplitudes with intensities results in

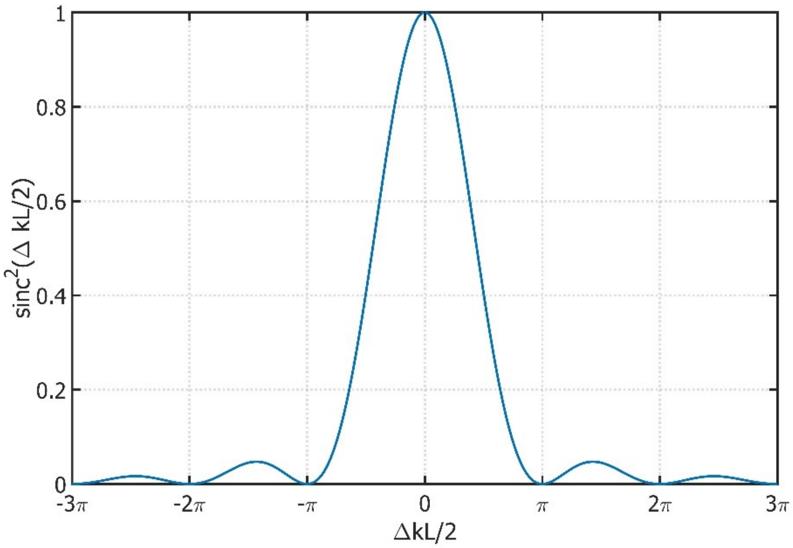

Figure 4.2 Sum frequency generation efficiency dependence on wavevector mismatch.

$$I_3 = \frac{8d_{eff}\omega_3^2 I_1 I_2 L^2}{n_1 n_2 n_3 \epsilon_0 c^2}\text{sinc}^2\left(\frac{\Delta kL}{2}\right) \qquad (4.16)$$

The sinc factor in the above equation is called the phase mismatch factor and it relates the efficiency of the three wave mixing to the ΔkL as shown in Figure 4.2. The efficiency increases with the crystal length for $\Delta k = 0$ and a coherence length can be defined as

$$L_{coh} = \frac{2}{\Delta k} \qquad (4.17)$$

at which point the output wave is out of phase with its driving polarization.

4.1.2 Second Harmonic Generation

The process of second harmonic generation (SHG) is schematically shown in Figure 4.3 together with its energy diagram. Through a nonlinear interaction process, the input wave of

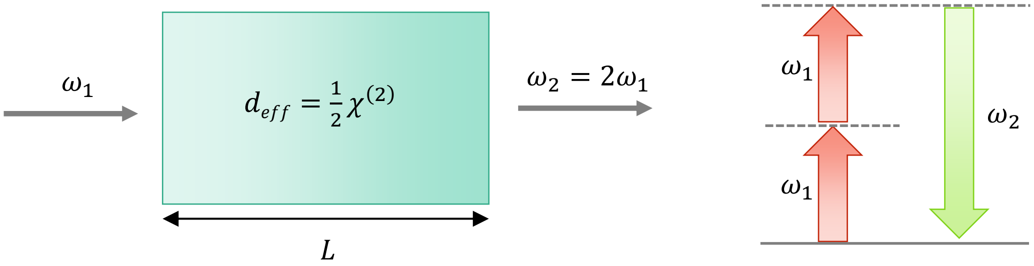

Figure 4.3 Second harmonic generation schematic and its energy diagram.

frequency ω_1 generates an output field with frequency $\omega_2 = 2\omega_1$. A derivation process similar to the one for SFG can be carried out to obtain the coupled amplitude equations for the case of SHG:

$$\frac{dA_1}{dz} = \frac{2id_{eff}\omega_1^2}{k_1c^2}A_1A_1^*e^{-i\Delta kz} \qquad (4.17)$$

$$\frac{dA_2}{dz} = \frac{id_{eff}\omega_2^2}{k_2c^2}A_1^2e^{i\Delta kz} \qquad (4.18)$$

where the wavevector mismatch is now equal to

$$\Delta k = 2k_1 - k_2 \qquad (4.19)$$

4.1.3 Difference Frequency Generation

Lastly, Figure 4.4 illustrates a difference frequency generation process (DFG) schematic and its energy diagram. The nonlinear interaction of two incident waves of frequencies ω_1 and ω_3 within a medium results in an output wave with a difference frequency ω_2. In this case, the ω_3 field is assumed to be strong, thus the amplitude A_3 can be considered constant. Again,

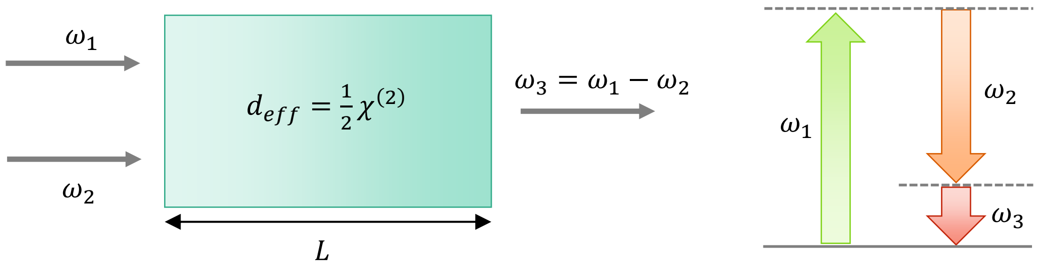

Figure 4.4 Difference frequency generation schematic and its energy diagram.

with the method analogous to the previous cases, the coupled amplitude equations describing DFG can be determined and described as

$$\frac{dA_1}{dz} = \frac{2id_{eff}\omega_1^2}{k_1c^2}A_3A_2^*e^{i\Delta kz} \qquad (4.20)$$

$$\frac{dA_2}{dz} = \frac{id_{eff}\omega_2^2}{k_2c^2}A_3A_1^*e^{i\Delta kz} \qquad (4.21)$$

where

$$\Delta k = k_3 - k_2 - k_1 \qquad (4.22)$$

4.2 Phase matching

The coupled amplitude equations serve as a basis to calculate the intensity of the generated light. In this dissertation, nonlinear optical interactions with Gaussian laser beams are discussed. The following section will be dedicated to the topic considering the power of light generated through nonlinear conversion with Gaussian beams. Since the frequency conversion efficiency is dependent on the wavevector mismatch and drastically decreases if $\Delta k = 0$ is not fulfilled, the various phase matching conditions will be discussed first. The condition for perfect phase matching with collinear beams is defined by

$$n_1(\omega_1)\omega_1 + n_2(\omega_2)\omega_2 = n_3(\omega_3)\omega_3 \qquad (4.23)$$

and it is assumed that $\omega_1 \leq \omega_2 \leq \omega_3$ and energy is conserved through $\hbar\omega_1 + \hbar\omega_2 = \hbar\omega_3$. Clearly, the (4.22) cannot ordinarily be satisfied as the refractive index changes monotonically with the frequency. To overcome this issue, material birefringence can be utilized by which the refractive index depends on the direction of polarization of the optical field. Thus, in order to achieve phase matching, the highest frequency wave has to be polarized in the direction which sees the lower refractive index, while at least one of the lower frequency waves has to be polarized in the direction of the higher refractive index. A birefringent crystal is characterized by principal indices n_x, n_y and n_z, which correspond to the axis. In the case of uniaxial crystals, $n_x = n_y \neq n_z$ and the ordinary index is $n_o = n_x = n_y$, while the extraordinary index is $n_z = n_e$. On the other hand, for biaxial crystals, all of the refractive indices are different: $n_x \neq n_y \neq n_z$. Moreover, the birefringent crystals can be positive or negative, which corresponds to which principal indices are the highest, as presented in Table 4.1.

	Uniaxial crystal	Biaxial crystal
Positive	$n_x = n_y < n_z$	$n_x < n_y < n_z$
Negative	$n_x = n_y > n_z$	$n_x > n_y > n_z$

Table 4.1 Summary of principal refractive indices for uniaxial and biaxial crystals.

4.2.1 Temperature phase matching

The refractive index is also temperature dependent and in some crystals this effect is strong enough that it can be utilized in phase matching. The temperature of a nonlinear crystal can be varied so the values of refractive indices seen by the interacting beams will fulfill the phase matching condition.

4.2.2 Angle phase matching

Angle phase matching refers to the case when a nonlinear crystal is precisely oriented with respect to the light propagation direction in such way that the refractive indices seen by the polarized beams satisfies the phase matching condition. Thus, is it clear that the collinear beams will experience different refractive indices based on the incident angle with respect to the crystal axis. Here, the general case for collinear phase matching in biaxial crystals, which is

SHG	Type I	$n_{pump}^{(fast)}\omega_{pump} = 2n_{signal}^{(slow)}\omega_{signal}$
	Type II	$n_{pump}^{(fast)}\omega_{pump} = n_{signal}^{(slow)}\omega_{signal} + n_{signal}^{(fast)}\omega_{signal}$
SFG	Type I	$n_{pump}^{(fast)}\omega_{pump} = n_{signal}^{(slow)}\omega_{signal} + n_{idler}^{(slow)}\omega_{idler}$
	Type II	$n_{pump}^{(fast)}\omega_{pump} = n_{signal}^{(fast)}\omega_{signal} + n_{idler}^{(slow)}\omega_{idler}$
		$n_{pump}^{(fast)}\omega_{pump} = n_{signal}^{(slow)}\omega_{signal} + n_{idler}^{(fast)}\omega_{idler}$
DFG	Type I	$n_{idler}^{(slow)}\omega_{idler} = n_{pump}^{(fast)}\omega_{pump} - n_{signal}^{(fast)}\omega_{signal}$
	Type II	$n_{idler}^{(slow)}\omega_{idler} = n_{pump}^{(fast)}\omega_{pump} - n_{signal}^{(slow)}\omega_{signal}$
		$n_{idler}^{(fast)}\omega_{idler} = n_{pump}^{(fast)}\omega_{pump} - n_{signal}^{(slow)}\omega_{signal}$

Table 4.2 Summary of phase matching methods for SHG, SFG and DFG for all crystal types.

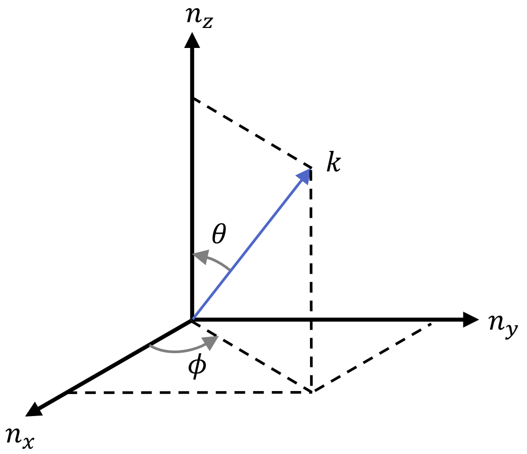

Figure 4.5 Principal refractive indices for a biaxial crystal with wave vector incident at arbitrary angle.

based on [99], will be presented. For both uniaxial and biaxial crystals, there are two different refractive indices for a single direction of propagation, thus they will be referred to as "fast" and "slow" indices and always $n_{fast} < n_{slow}$. Since uniaxial crystals have ordinary and extraordinary indices, they will be renamed accordingly to simplify the notation. Now, let's also redefine the frequency naming to be consistent for all nonlinear conversion schemes such that $\omega_{pump} \geq \omega_{signal} \geq \omega_{idler}$. Thus, the possible phase matching conditions considering the slow and fast refractive indices, regardless of crystal type, can be easily summarized. Table 4.2 represents these possibilities for SHG, SFG and DFG. The beams will be incident on the crystal at a certain angle, thus the crystal axis has to be considered. Figure 4.5 shows principal refractive indices for the general case of a biaxial crystal, with an incident k vector in an arbitrary direction. The refractive index $n(\hat{s})$ in any given direction $\hat{s} = (s_x, s_y, s_z)$ can be found using Fresnel's equation of wave normals in terms of the crystal principal dielectric axes [4.6]

$$\frac{s_x^2}{n^{-2}(\hat{s})-n_x^{-2}} + \frac{s_y^2}{n^{-2}(\hat{s})-n_y^{-2}} + \frac{s_z^2}{n^{-2}(\hat{s})-n_z^{-2}} = 0 \qquad (4.24)$$

where

$$\hat{s} = \begin{pmatrix} \sin\theta\cos\phi \\ \sin\theta\sin\phi \\ \cos\theta \end{pmatrix}_{x,y,z} \tag{4.25}$$

and n_x, n_y and n_z are the principal refractive indices at a given wavelength. The above equation can be solved for $n(\hat{s})$, which gives solution for both fast and slow polarizations

$$n_{fast} = \left[\frac{2}{B+(B^2-4C)^{1/2}}\right]^{1/2} \tag{4.26}$$

$$n_{slow} = \left[\frac{2}{B-(B^2-4C)^{1/2}}\right]^{1/2} \tag{4.27}$$

with

$$B = \left[s_x^2\left(\frac{1}{n_y^2}+\frac{1}{n_z^2}\right)+s_y^2\left(\frac{1}{n_z^2}+\frac{1}{n_x^2}\right)+s_z^2\left(\frac{1}{n_x^2}+\frac{1}{n_y^2}\right)\right] \tag{4.28}$$

and

$$C = \left[\frac{s_x^2}{n_y^2 \cdot n_z^2}+\frac{s_y^2}{n_z^2 \cdot n_x^2}+\frac{s_z^2}{n_x^2 \cdot n_y^2}\right] \tag{4.29}$$

With this set of equations the phase matching condition can be found for any of the cases listed in Table 4.2. Since it is the most general case, any type of nonlinear crystal can be chosen and its values of principal refractive indices can be found with Sellmeier equations. Once the desired wavelengths (frequencies) and nonlinear process type is decided, the fast and slow refractive indices can be calculated, thus the phase matching condition can be solved numerically for any angle ϕ or θ. The type II SFG in a negative biaxial lithium triborate crystal is used as example of calculated phase matching angles θ when $\phi = 90°$ for the input wavelength range of $800 - 1500\ nm$ as presented in Figure 4.6. After the phase matching angles

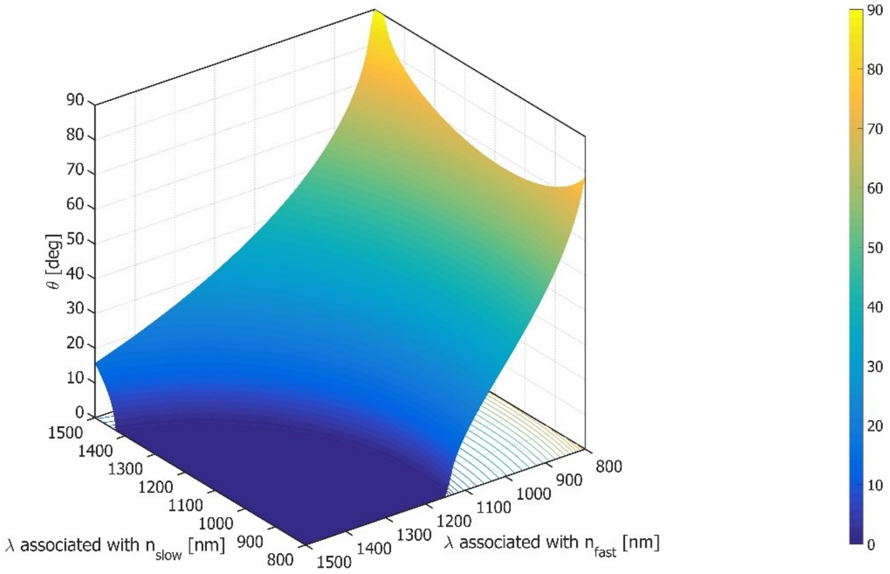

Figure 4.6 Phase matching angle θ for type II SFG in a LBO crystal ($\phi = 90°$) for input wavelengths range of $800 - 1500\ nm$.

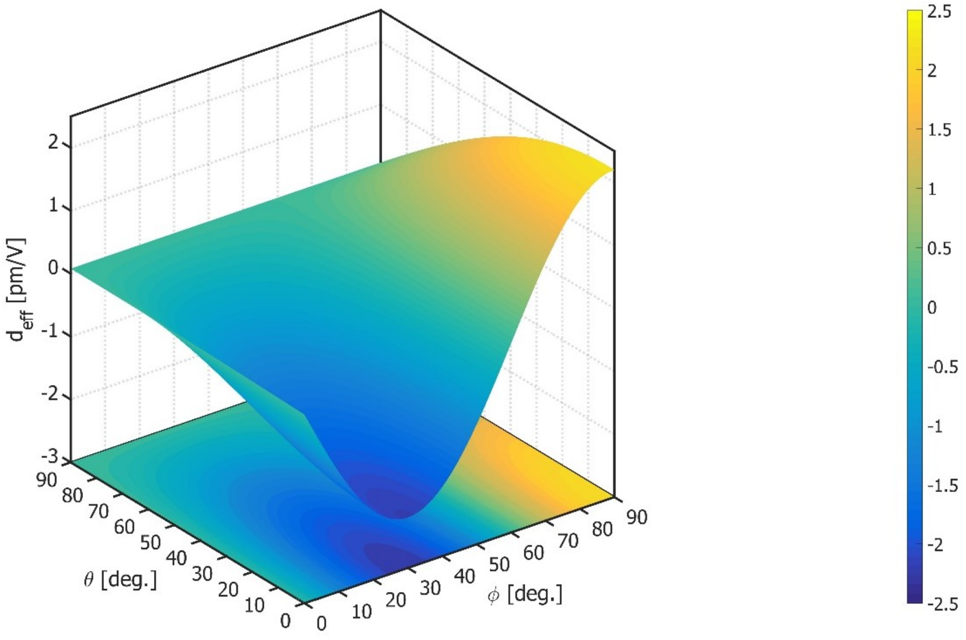

Figure 4.7 All possible d_{eff} values for type I SFG in a BBO crystal.

are found, the nonlinear coefficient can be calculated based on the tabulated d_{eff} equations provided for specific nonlinear crystals [100]. On the other hand, d_{eff} can be calculated for all the possible angles for the chosen phase matching type. Figure 4.7 illustrates all possible d_{eff} values for negative uniaxial beta-barium borate crystal for type I SFG.

4.2.3 Quasi phase matching

For cases when the crystal birefringence is insufficient or the nonlinear coefficient is not large enough, the quasi phase matching technique can be used. The method utilizes a periodically poled nonlinear crystal which is fabricated in a way such that the orientation of one of the crystalline axes is inverted periodically along the propagation direction. This allows

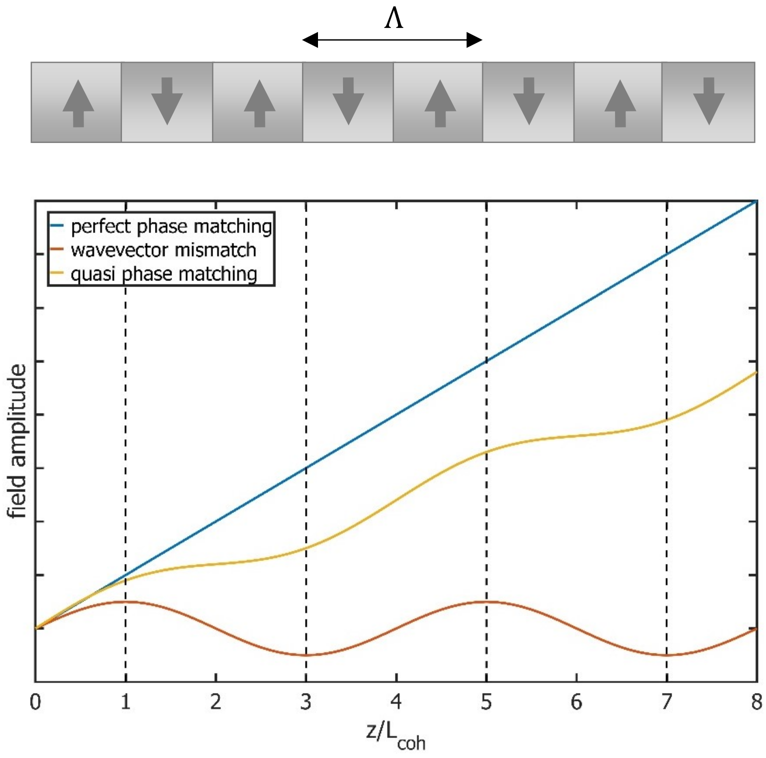

Figure 4.8 Schematic of a periodically poled crystal with corresponding field amplitude along the propagation distance.

for inversion of the sign of the nonlinear coefficient, thus the periodic variation of the d_{eff} sign compensates for a nonzero wavevector mismatch Δk. The schematic of such a nonlinear crystal is shown in Figure 4.8 along with the graph showcasing the quasi phase matching effect on the field amplitude. The poling period is chosen to fulfill the following requirement

$$\Lambda = 2L_{coh} = \frac{2\pi}{\Delta k} \qquad (4.30)$$

and Δk is the wavevector mismatch for any type of three wave mixing.

4.3 Focusing Gaussian beam into nonlinear crystals

The Gaussian beam propagating within the VECSEL laser cavity is focused into a nonlinear crystal to increase its intensity and hence the efficiency of the nonlinear conversion. Boyd and Kleinman, in their extensive paper [101], derive the optimal conditions for which the generated wave has the maximum power. The efficiency of the conversion is related to the focusing parameter which is defined as

$$\xi = \frac{L}{b} \qquad (4.31)$$

where

$$b = \frac{2\pi n w_0^2}{\lambda} \qquad (4.32)$$

is the confocal parameter for a Gaussian beam with a beam waist w_0 and wavelength λ propagating in a medium with refractive index n. A new function, which contains the optimizable parameters phase mismatch σ and focusing strength ξ, is introduced. In the more general case of the walk-off, material absorption and focal position are also included. Here, the walk-off and material absorption are considered negligible and the Gaussian beam is assumed to be focused at the center of the crystal. This function directly relates the power of the input waves to the new wave output power and is written as

$$h_m(\xi, \sigma) = \frac{1}{4\pi}\left(\int_{-\xi}^{\xi} \frac{\cos\sigma\tau + \tau\sin\sigma\tau}{1+\tau^2} d\tau\right)^2 \qquad (4.33)$$

where τ is an integration variable describing the Gaussian beam position away from its focus point in the nonlinear crystal and the phase mismatch parameter is equal to

$$\sigma = \frac{1}{2} b\Delta k \qquad (4.34)$$

For the case of SHG, the optimization process allows determination of the maximum value of the h_m function for certain values of ξ and σ. Surprisingly, the highest intensity of the generated wave is obtained for a non-zero value of the wavevector mismatch. This is due to the π phase shift experienced by the beam after passing through its focus point, which has to be compensated, so the nonlinear polarization can couple to the generated wave amplitude. The h_m function with optimal value of σ plotted against ξ is shown in Figure 4.9. The peak value of 1.068 is achieved for $\xi = 2.84$. This value of focusing parameter can be plugged into equation (4.31) and the optimal Gaussian beam waist can be found for a chosen crystal length. Also, in the case of the SHG the output power of the second harmonic wave is equal to

$$P_{pump} = \frac{16\,\pi^2 d_{eff}^2 L}{\epsilon_0 c n_{signal}^2 \lambda_{signal}^3} h_m(\xi) P_{signal}^2 \qquad (4.35)$$

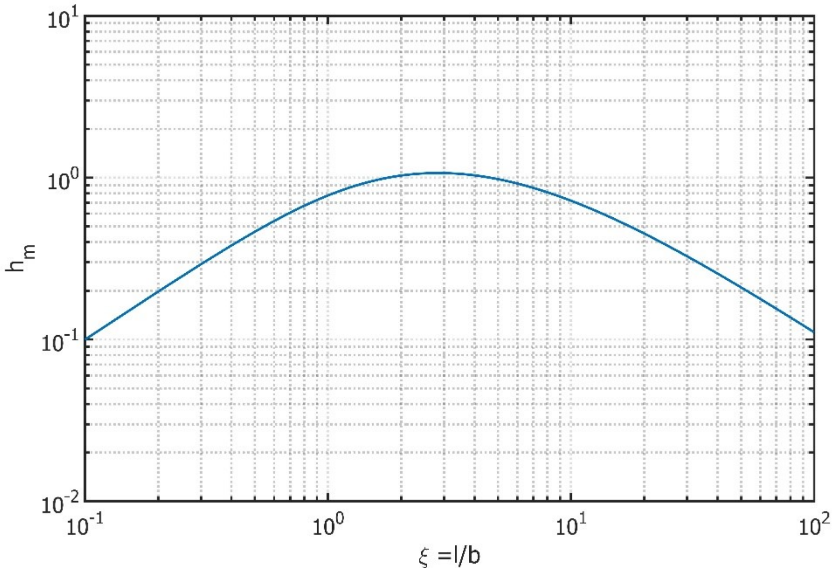

Figure 4.9 Function $h_m(\xi)$ plotted for optimum phase matching condition.

where P_{signal} is the input power of the fundamental wave. In the [101] Boyd and Kleinman state that the h function can be used and optimized to describe the cases of SFG and DFG. Then, the output power of the sum frequency wave is described by

$$P_{pump} = \frac{32\,\pi^2 d_{eff}^2 L}{\epsilon_0 c n_{pump} \lambda_{pump}^2 (n_{signal}\lambda_{idler} + n_{idler}\lambda_{signal})} P_{signal} P_{idler} \qquad (4.36)$$

where the P_{signal} and P_{idler} are similarly the powers of the two fundamental waves.

The case of difference frequency generation has been further expanded in [102, 103], with the h function extended for two input wavelengths

$$h(\mu,\xi) = \frac{1}{2\xi}\int_0^{\xi} d\tau' \int_{-\xi}^{\xi} d\tau \frac{1+\tau\tau'}{(1+\tau\tau')^2 + \frac{1}{4}\left(\frac{1+\mu}{1-\mu} + \frac{1-\mu}{1+\mu}\right)^2 (\tau-\tau')^2} \qquad (4.37)$$

where τ and τ' are integration variables describing both fundamental Gaussian beams positions away from their focus point in the crystal and

$$\mu = \frac{k_{signal}}{k_{pump}} \qquad (4.38)$$

The h function plotted for a few values of μ is presented in Figure 4.10. The peak value occurs for $\xi = 1.3$ and is dependent on the pump and signal wavelengths. The output power of the difference frequency wave is equal to

$$P_{idler} = \frac{(2\omega_{idler}d_{eff})^2 L}{\epsilon_0 \pi c^3 n_{pump} n_{signal} n_{idler}} \frac{h(\mu,\xi)}{k_{signal}^{-1} + k_{pump}^{-1}} P_{signal} P_{pump} \qquad (4.39)$$

Moreover, for sum and difference frequency generation, the conversion efficiency is the highest if the confocal parameters of input beams are equal. In addition, the new wave will have the same confocal parameter as the input waves, thus it is valid for all the cases that

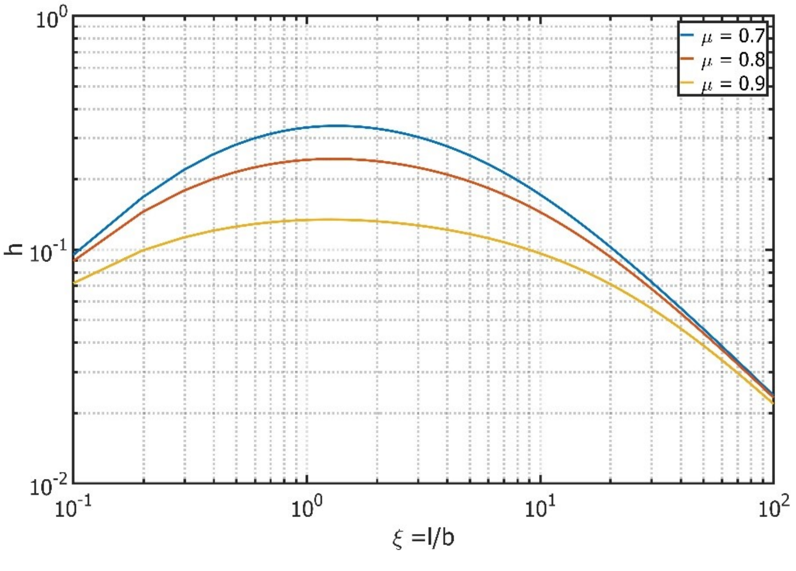

Figure 4.10 Function $h(\xi)$ plotted for the DFG case for a few values of μ.

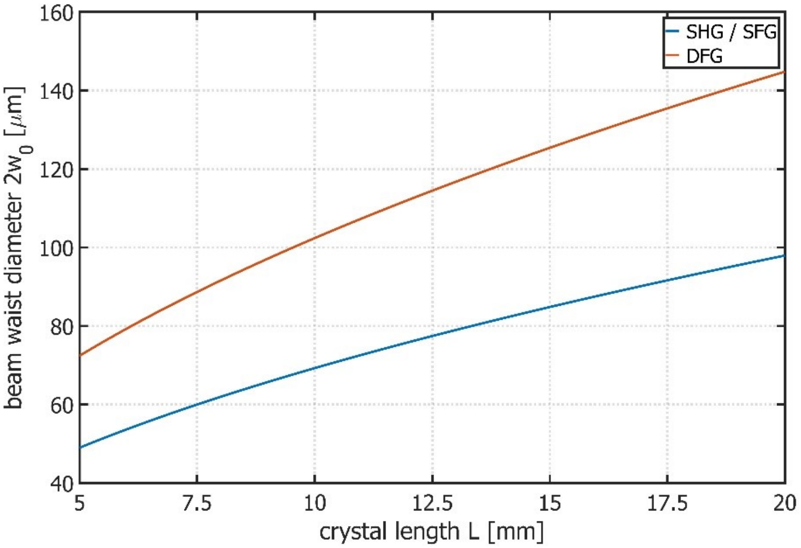

Figure 4.11 Beam waist diameter for various crystal lengths for $\lambda = 1070\ nm$.

$$b = \frac{2\pi n_{pump} w_{0pump}^2}{\lambda_{pump}} = \frac{2\pi n_{signal} w_{0signal}^2}{\lambda_{signal}} = \frac{2\pi n_{idler} w_{0idler}^2}{\lambda_{idler}} \quad (4.40)$$

To summarize, since the beam focusing and crystal length can be controlled, the dependence of optimal beam waist radius on crystal length is described by:

$$w_0 = \sqrt{\frac{L\lambda}{2.84 \cdot 2\pi n}} \quad (4.41)$$

for SHG and SFG, and

$$w_0 = \sqrt{\frac{L\lambda}{1.3 \cdot 2\pi n}} \quad (4.42)$$

for DFG. Figure 4.11 illustrates the preferable beam waist diameter for various nonlinear crystal lengths at $\lambda = 1070\ nm$.

4.4 Nonlinear crystals

In order for a nonlinear crystal to be suitable for the desired application, it has to fulfill the phase matching conditions at the desired wavelengths and have a large enough nonlinear coefficient for efficient frequency conversion. In case of VECSELs, additional two requirements are crucial: high damage threshold and very high transparency at fundamental wavelengths. The nonlinear crystal has to operate within the laser cavity, where the circulating field power is of the order of hundreds of Watts, thus a high damage threshold prevents possible damaging of the crystal. Since the VECSEL is a low gain laser, any loss added to the system can drastically decrease the performance efficiency, thus a crystal with a very low absorption coefficient at the fundamental wavelength is necessary. In addition, any absorption will result in heating of the nonlinear crystal, thus destabilizing the phase-matching condition. Moreover, the absorption at the generated wavelength should be low as well for its effective extraction.

For the purposes of second harmonic and sum frequency generation, well established lithium triborate (LBO) crystals are utilized. It has an absorption coefficient of $\sim 0.00035\ cm^{-1}$ and $d_{eff} \approx 0.8\ pm/V$ in the wavelength range of $900 - 1200\ nm$ [100]. In the experiments it is used for type I SHG to blue and green and for type II SFG to green. For further down conversion to the UV range, a beta barium borate (BBO) crystal is used. Its absorption coefficient is $\sim 0.01\ cm^{-1}$ for visible light and $d_{eff} \approx 1.4\ pm/V$ [100]. In case of the DFG to reach the mid-IR range, silver thiogallate (AGS) is utilized. For the fundamental wavelengths the absorption coefficient of AGS is $\sim 0.01\ cm^{-1}$ and it provides a large nonlinear coefficient of $> 11\ pm/V$ [100]. Finally, a magnesium oxide doped periodically poled lithium niobate crystal (MgO_2:PPLN) is used in attempt to generate THz radiation. The absorption coefficient is $\sim 0.002\ cm^{-1}$ in the fundamental wavelength range [4.8], but is very in the THz range, thus usually the idler beam is propagated perpendicular to the direction of the fundamental beams. The nonlinear coefficient is $\approx 20\ pm/V$ along the optical axis of the PPLN crystal [100].

Chapter 5 – High Power Second Harmonic Generation to Visible Spectrum

The intracavity second harmonic generation in VECSEL lasers allows achievement of high power, tunable outputs with excellent beam quality. Here, semiconductor chips with MQWs designed for emission at $\sim 970\,nm$ and $\sim 1070\,nm$ are utilized for frequency conversion to blue and green radiation, respectively. In both cases a folded V-cavity geometry was used with an intracavity birefringent filter for tuning purposes. An LBO crystal served as the nonlinear element for SHG.

5.1 Green VECSEL

5.1.1 Setup design

In the experiment a VECSEL heterostructure grown using metal oxide chemical vapor deposition (MOCVD), designed to emit at $\sim 1070\,nm$, was used. The active region consists of 12 compressively strained $8\,nm$ thick InGaAs quantum wells with GaAs pump absorbing barriers and a layer of GaAsP between each QW for strain compensation. On top of the multi-quantum wells are 25 pairs of alternating AlGaAs/AlAs grown to serve as a high reflectivity ($\sim 99.9\,\%$) distributed Bragg reflector at the emission wavelength. The specific thickness and composition of the heterostructure layers were designed to achieve resonant periodic gain. The VECSEL chip was fabricated using the processes described in Chapter 3

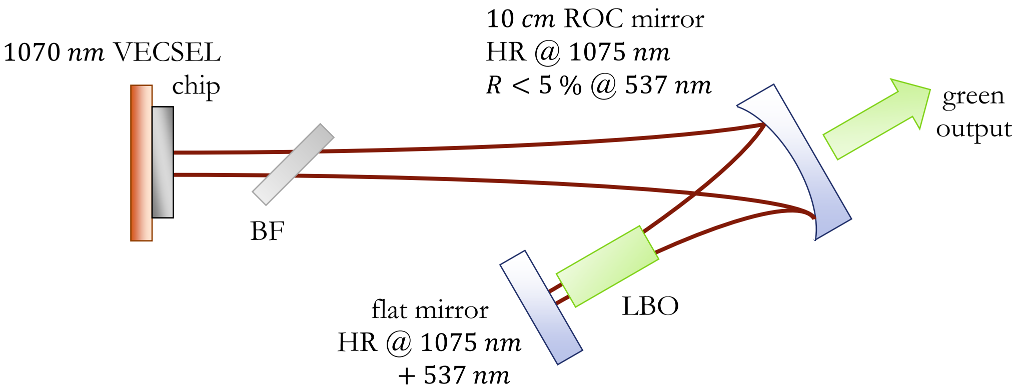

Figure 5.1 V-cavity VECSEL setup for SHG to green output.

and served as one of the end mirrors in a V-cavity configuration. A spherical concave mirror with radius of curvature equal to 10 cm served as a folding mirror, while a flat mirror served as the other end mirror, as illustrated in Figure 5.1. Both mirrors were high reflectivity coated for 1075 nm while the flat mirror was also HR coated for 535 nm. This allows all of the green light to be extracted through the fold mirror which had a low reflectivity (< 5 %) coating at 537 nm. The optical pumping delivered by the fiber-coupled 808 nm pump diode resulted in a pump spot with a diameter of ~550 μm on the chip surface. The beam spot size on the end mirror was chosen to provide optimal conversion efficiency in the nonlinear crystal. Since a 1.5 cm long crystal is used, the mode diameter was estimated to be ~80 μm. To ensure fundamental TEM_{00} operation while mode matching to the optical pump spot and maintaining the appropriate beam size at the nonlinear crystal, the distance between the chip and curved mirror was ~20 cm and the distance from the curved mirror to the flat mirror was ~6 cm. LBO crystals with dimensions of $3 \times 3 \times 15\ mm^3$ and both facets AR coated for both 1075 nm and 537 nm were placed in the proximity of the end mirror. The LBO was cut for type I angular phase-matching at angles $\theta = 90°$ and $\phi = 11°$. Also, a 3 mm thick BF was inserted for linewidth and tunability purposes. Lastly, during the experiment, the copper heat sink was maintained at 10°C.

5.1.2 Experimental results

Before proceeding with the SHG, the fundamental operation of the VECSEL chip was first characterized. The same cavity configuration was used, except all of the intracavity elements were not yet in place and the flat mirror was switched to a $96.5\ \%$ reflective output coupler. Figure 5.2 presents the output power with respect to the absorbed pump power. A maximum output power of $\sim 27.1\ W$ was achieved. The slope efficiency value was near $50\ \%$ and the optical efficiency was $\sim 35\ \%$ at highest power level. The free lasing spectra is shown in Figure 5.3 at various pump levels with the peak power wavelength at $\sim 1077\ nm$. To inspect the gain tunability, the BF was placed into the long arm part of the cavity. While maintaining the pump power at $\sim 59\ W$, tuning measurements were performed. In steps of $1\ nm$ between

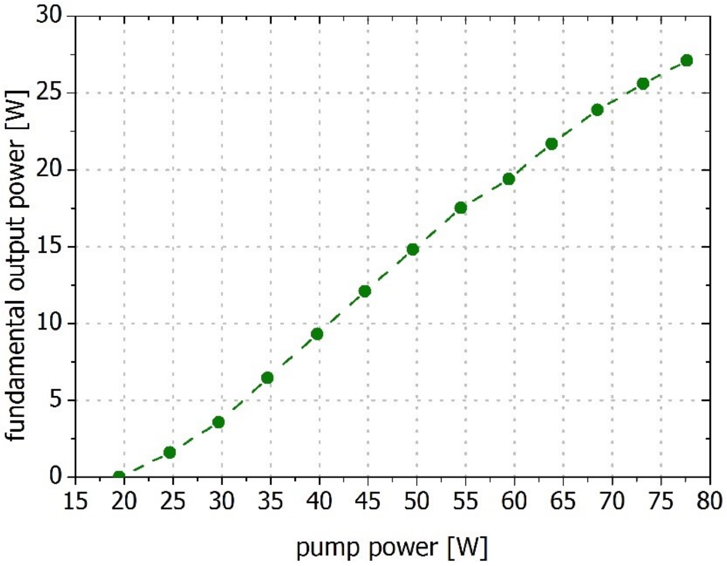

Figure 5.2 Fundamental output power characteristics of the V-cavity with $3.5\ \%$ transmission output coupler.

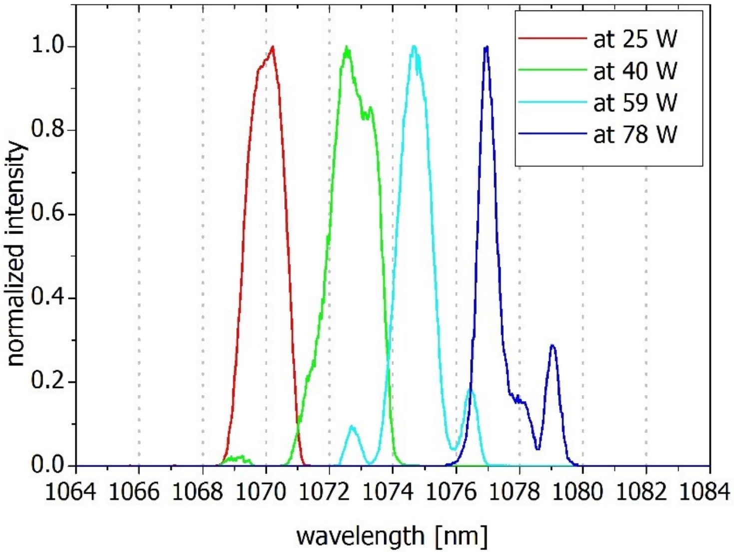

Figure 5.3 Fundamental free lasing spectra from V-cavity VECSEL.

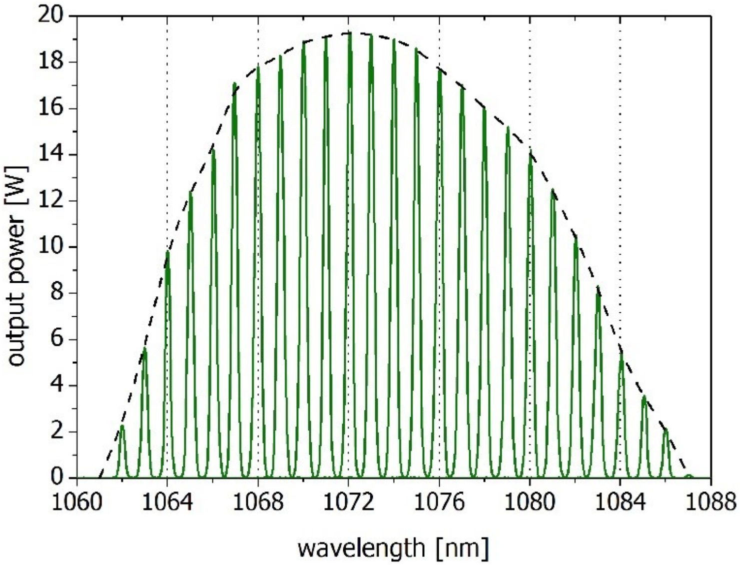

Figure 5.4 Fundamental output tuning with $3\ mm$ thick BF at a pump power level of $\sim 59\ W$. Each peak is normalized to the output power obtained at the corresponding wavelength.

the peaks, each wavelength spectrum was captured and the output power was measured to demonstrate the gain tunability curve. These spectral peaks were normalized to the corresponding output power and this data is presented in Figure 5.4. Based on the graph, the tunability range was $24\ nm$ and the linewidth of each peak was less than $0.15\ nm$.

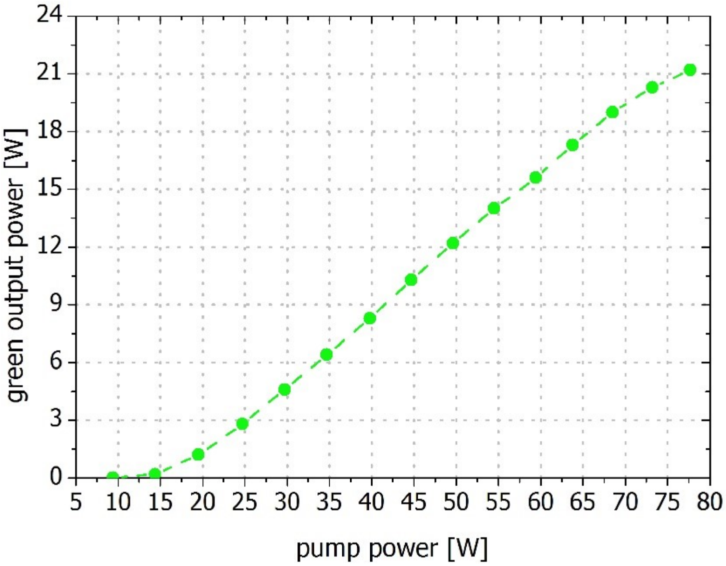

Figure 5.5 Green output power characteristics of V-cavity VECSEL with $1.5\ cm$ long LBO crystal.

After characterizing the fundamental operation of the chip, the flat end mirror was replaced with the one that was HR coated at $1075\ nm$ and $537\ nm$ to achieve a high Q cavity. The LBO crystal was introduced into the cavity and the BF was adjusted to maximize the green output power. Figure 5.5 presents the green output power versus the absorbed pump power, with the highest power of $\sim 21.2\ W$ at $537\ nm$. The optical conversion efficiency from the $808\ nm$ pump diode to green output was $\sim 27\ \%$ at maximum output and the overall slope efficiency was $\sim 34\ \%$. The process of tuning the green output was similar as in the fundamental wavelength case. As the BF was adjusted, the spectral peaks were captured and the output power was measured at each step. The data taken at a pump power of $\sim 64\ W$ is shown in Figure 5.6. Again, the graph presents the spectral peaks versus the output power. The linewidths of the green spectral peaks were maintained below $0.15\ nm$, while the tunability range was $15\ nm$.

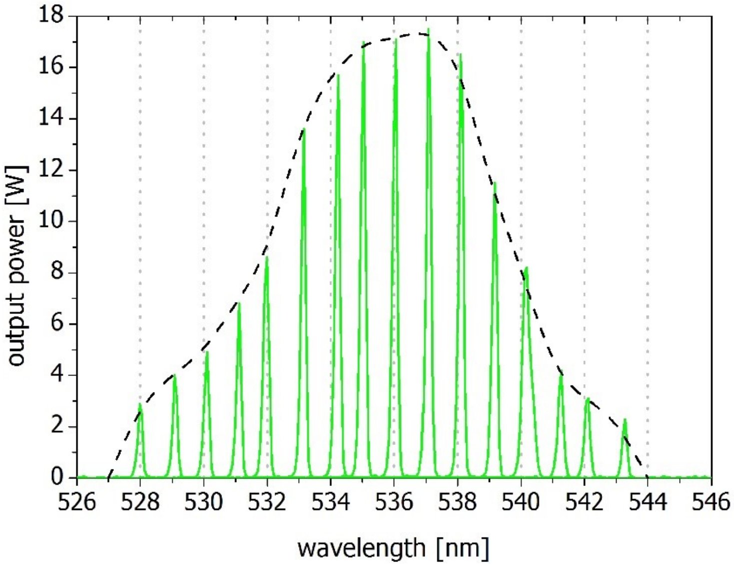

Figure 5.6 Green output tuning with $3\ mm$ thick BF at pump power level of $\sim 64\ W$. Each peak is normalized to the output power obtained at the corresponding wavelength.

Lastly, to ensure the TEM_{00} operation of the laser, the beam profiles for both fundamental and second harmonic emission were characterized in a manner described in Chapter 3. The M^2 value of the fundamental beam was measured for output power at $\sim 15\ W$ and at $\sim 7\ W$ for the green beam. The 3D profiles of both beams are represented in Figure 5.7. The M^2 values were ~ 1.8 and ~ 1.4 for the fundamental and the green beams, respectively. Based on these results, even at the maximum green power level, the beam quality M^2 value should

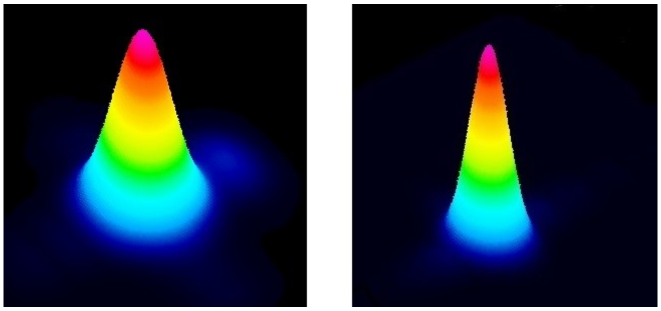

Figure 5.7 The profiles of the fundamental (left) and green (right) beams, with the M^2 values of ~ 1.8 and ~ 1.4, respectively.

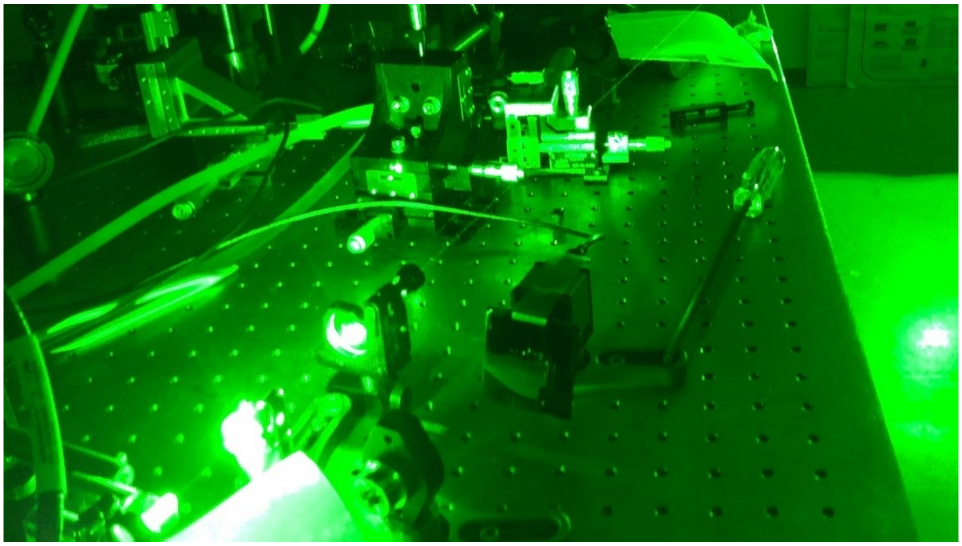

Figure 5.8 The picture of green output from VECSEL SHG setup.

stay below 2. The picture taken of the high power green VECSEL setup during operation is presented in Figure 5.8.

VECSELs are capable of outputs exceeding $20\,W$ in green emission by the means of second harmonic generation. The visible light can maintain good beam quality at high power levels and the output can be tunable over a broad range. Further power scaling, up to a possible $30\,W$ of cw green output power, can be achieved by increasing the optical pump spot size on the chip and using a longer nonlinear crystal.

5.2 Blue VESCEL

5.2.1 Experimental setup

The VECSEL setup used for SHG of blue light is very similar to the one used for green generation. Here, all of the cavity elements used are designed for fundamental emission at

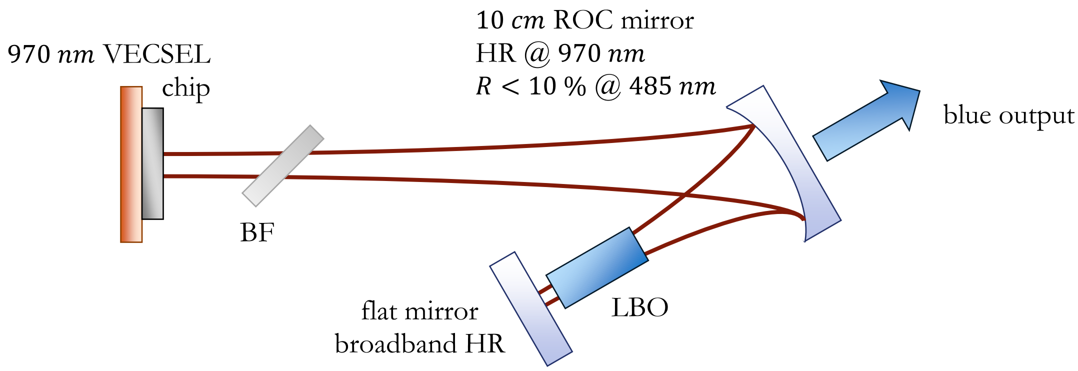

Figure 5.9 V-cavity VECSEL setup for SHG to blue output.

$\sim 970\ nm$ and for generation and extraction of the emission at $\sim 485\ nm$ as illustrated in Figure 5.9. The VECSEL chip was of the same structural design, also with twelve $8\ nm$ thick MQWs. The same fabrication process was also applied. Due to the wavelength difference, the V-cavity lengths were slightly different with a $\sim 20\ cm$ long arm and a $\sim 5.5\ cm$ short arm. The optical pump spot size stayed the same, but the spot diameter on the flat end mirror was reduced to $\sim 75\ \mu m$, thus the cavity length was adjusted to support fundamental TEM_{00} operation. The $10\ cm$ ROC fold mirror was HR coated at $\sim 970\ nm$, and at $\sim 485\ nm$ the reflectivity was $< 10\ \%$. For blue output generation, the $15\ mm$ long LBO crystal was used and had $3 \times 3\ mm^2$ facets, AR coated for the fundamental and corresponding second harmonic wavelength. For the nonlinear crystal to be properly cut, the angle phase-matching requirement was $\theta = 90°$ and $\phi = 17°$.For the initial fundamental wave power characteristics, the flat end mirror was $96\ \%$ reflective. This was later replaced with a broadband HR flat mirror.

5.2.2 Experimental results

Figure 5.10 presents the output power characteristics for the fundamental emission with no intracavity elements. The maximum output of ~$26.8\ W$ was obtained with optical efficiency ~$31\ \%$ at the highest power and the calculated slope efficiency value was near $47\ \%$. In

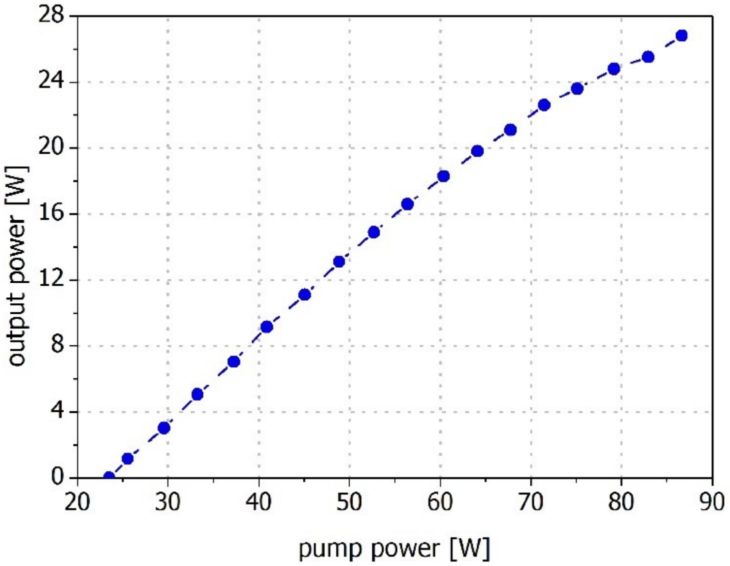

Figure 5.10 Fundamental output power characteristics of V-cavity with $3.5\ \%$ transmission output coupler.

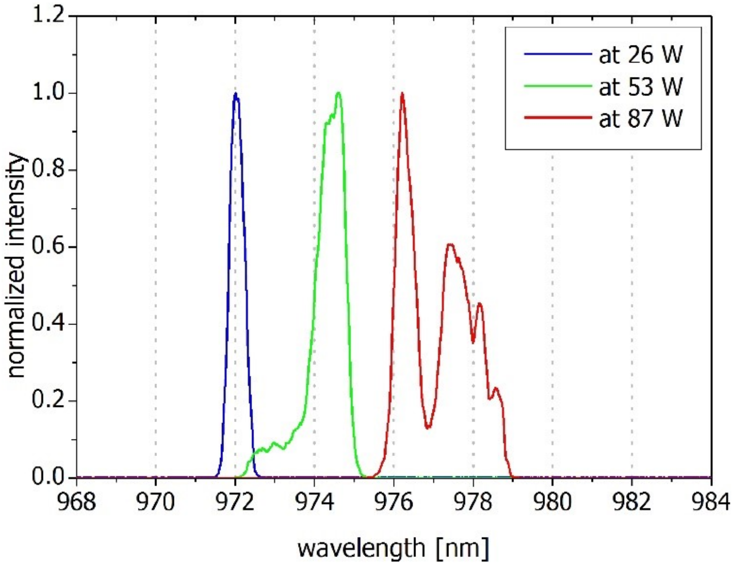

Figure 5.11 Fundamental free lasing spectra from V-cavity VECSEL.

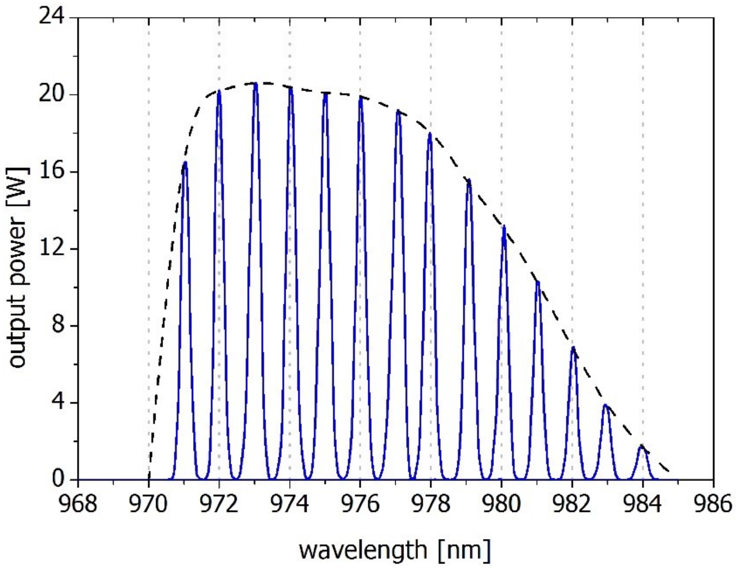

Figure 5.12 Fundamental output tuning with $3\ mm$ thick BF at pump power level of $\sim 67.8\ W$. Each peak is normalized to the output power obtained at the corresponding wavelength.

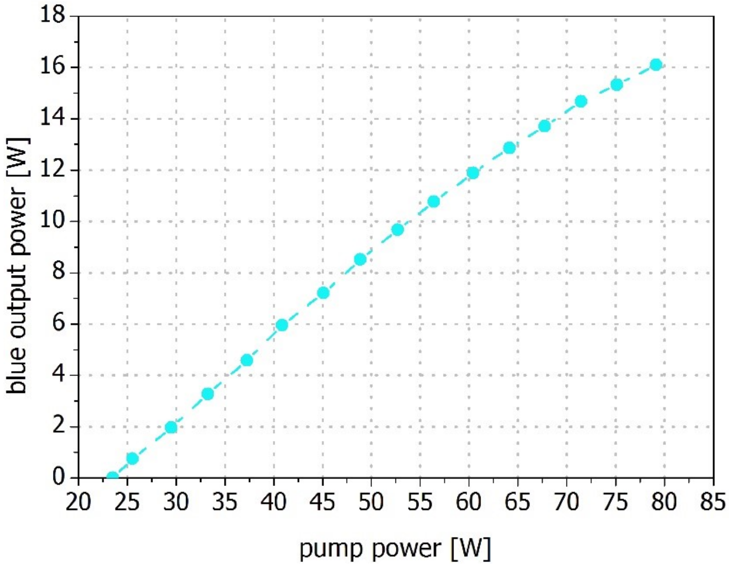

Figure 5.13 Blue output power characteristics of V-cavity VECSEL with $1.5\ cm$ long LBO crystal.

Figure 5.11 the free lasing spectra at various pump levels is shown, with the peak power wavelength at $\sim 976\ nm$. Similarly to the previous VECSEL setup, the $3\ mm$ thick BF was inserted in the cavity to perform the gain tuning. Figure 5.12 shows the tunability curve at

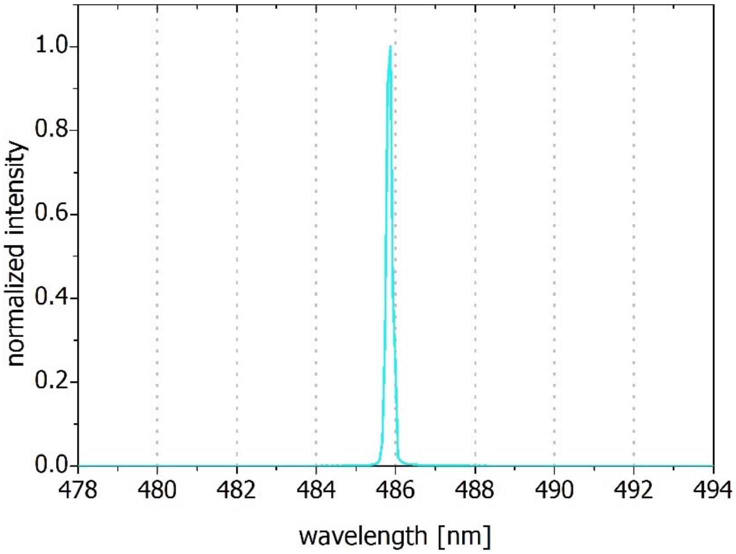

Figure 5.14 The blue output coherent spectrum at pump power level of $\sim 64\,W$.

$67.8\,W$ pump power with captured spectral peaks normalized to the output power measured at the corresponding wavelength. The spectral peaks had FWHM of less than $0.15\,nm$ and the overall tuning range was $\sim 13\,nm$.

The results of the SHG are shown on the output power curve in Figure 5.13. With the optical conversion efficiency of $\sim 20\,\%$, the maximum output was $\sim 16.1\,W$ and the slope efficiency was $\sim 29\,\%$. The blue spectrum is presented in Figure 5.14. The SHG lead to emission at $\sim 486\,nm$.

Again, beam quality measurements were performed for both fundamental and blue output. Figure 5.15 showcases the 3D profiles of both beams captured at $\sim 10\,W$ and $\sim 5\,W$ for fundamental and blue output powers, respectively. The M^2 value was ~ 1.5 for the $\sim 972\,nm$ emission and ~ 1.4 for the $\sim 486\,nm$ emission. These results are a good indication that the beam can preserve its high brightness at high output power levels. A photo of the blue VECSEL setup was also captured and is presented in Figure 5.16.

The VECSEL can deliver cw high output power in blue spectral regions as well. Over $16\ W$ at $\sim 486\ nm$ was achieved with good beam quality. Similar power scaling measures can be taken in this case as well, and outputs beyond $25\ W$ could be reached

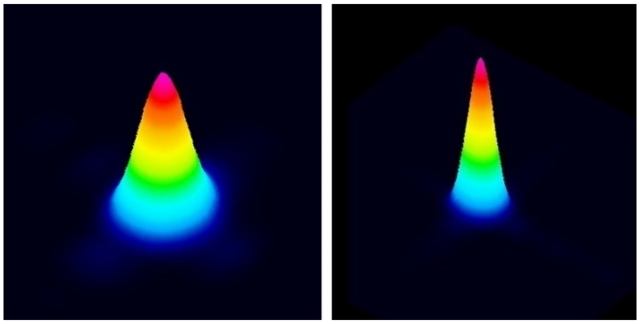

Figure 5.15 The profiles of the fundamental (left) and blue (right) beams, with the M^2 values of ~ 1.5 and ~ 1.4, respectively.

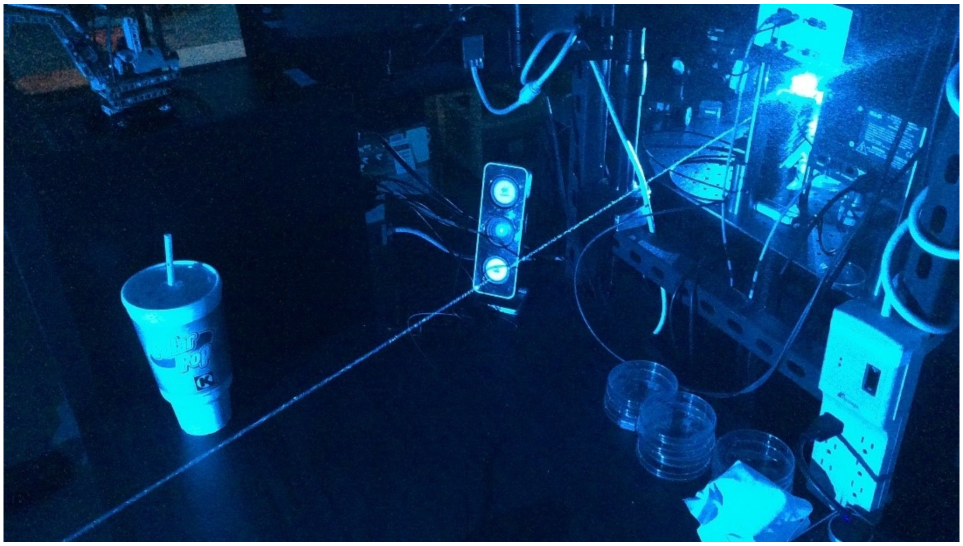

Figure 5.16 The picture of blue output from the VECSEL SHG setup.

Chapter 6 – Sum Frequency Generation in T-cavity VECSEL

The T-cavity geometry expands the VECELs flexibility even further, allowing for type I or type II sum frequency generation to the visible spectrum. With the possibility to independently tune each of two gain chips, the overall tuning range can be greatly extended. Here, a T-cavity with a set of chips lasing at ~980 *nm* and ~1180 *nm* is used for the conversion to green radiation by the means of type II SFG. In addition, a slight modification to the cavity allowed simultaneous achievement of SHG and SFG with a collinear output of blue and green light.

6.1 SFG to Green Output

6.1.1 Setup design

A set of two chips from different wafer growths was used in the experiment. The first structure (~980 *nm*) consisted of 14 compressively strained 8 *nm* thick InGaAs quantum wells, which were surrounded by GaAsP strain compensation layers and GaAs pump absorbing barriers. The 25 alternating $Al_{0.2}Ga_{0.8}As/AlAs$ pairs grown on top of the active region constituted the distributed Bragg reflector layer. The RPG was also incorporated into the design. The second chip (~1180 *nm*) was cleaved from a heterostructure with a gain stack consisting of 10 compressively strained 7 *nm* thick InGaAs QWs, also surrounded by GaAsP

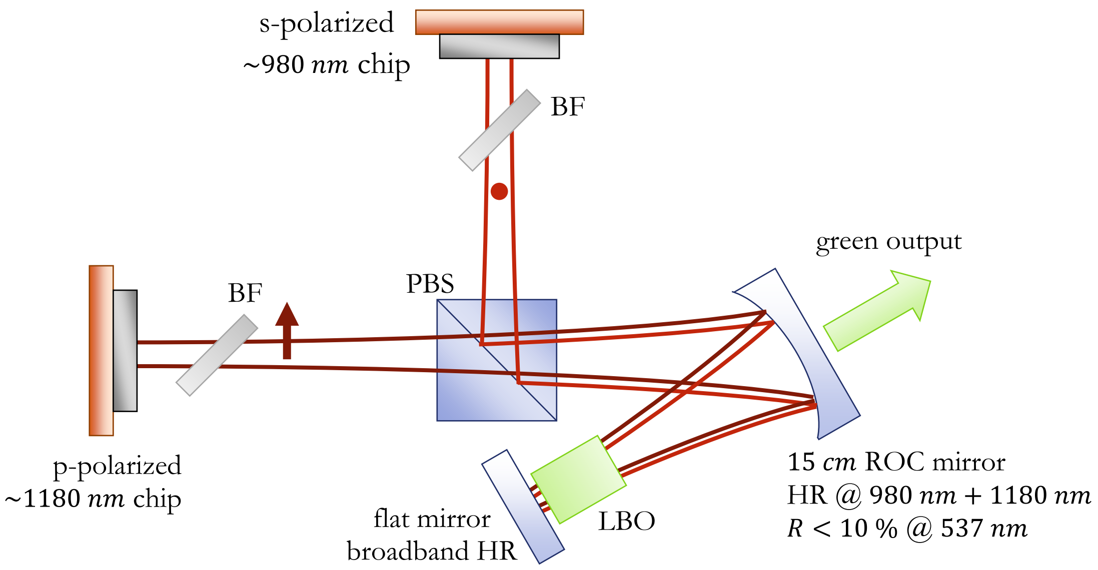

Figure 6.1 Schematic of a folded T-cavity VECSEL used for type II SFG.

strain compensation layers and pump absorbing GaAs barriers. The RPG design was utilized as well. The DBR stack was made of 21 pairs of GaAs/AlAs layers. Both chips were fabricated using the techniques described in Chapter 3.

The T-cavity had to be adjusted to allow for the beam to refocus into a nonlinear crystal. The original output coupler became a fold mirror and a flat end mirror is added as shown in Figure 6.1, thus the common part of the setup resembles the V-cavity. The polarizing beam splitter defines the linear polarization of cavity regions. All of the sides of the PBS are AR coated for the fundamental wavelengths and the intracavity losses introduced by it are estimated to be ~0.5 % and ~2 % for ~980 nm and ~1180 nm wavelengths, respectively. The ~1180 nm chip is part of the p-polarized cavity, which also includes a 2 mm thick BF. The other arm of the T-cavity consisted of the ~980 nm chip and another 2 mm thick BF which was oriented to match the s-polarized circulating field. The shared fold mirror had a 15 cm ROC and was positioned ~17 cm away from the two chips. The distance from the fold mirror to the end mirror was ~10 cm, which resulted in ~ 200 μm diameter spot on the flat end mirror, while the pump spot diameter on each chip was ~ $500\ \mu m$. The curved mirror was HR coated for fundamental wavelengths and low reflection ($< 5\ \%$) coated for the visible spectrum. The flat mirror had a HR broadband coating applied. For the purpose of type II SFG, the $3 \times 3 \times 10\ mm^2$ LBO crystal was introduced into the laser cavity. The crystal was cut at angles $\theta = 35.6°$ and $\phi = 90°$ and its facets were AR coated for fundamental and green wavelengths. This cut provides an effective nonlinear coefficient of $0.54\ pm/V$. During the experiment both chips were mounted to copper heat sinks and maintained at 15℃ temperature.

6.1.2 Experimental results

The efficiency of SFG depends on two beams overlapping in the nonlinear crystal, thus the collinearity of fundamental beams was ensured by characterizing their profiles. The beams were refocused onto a DataRay BeamMap2 beam profiler and the measurements were performed for three cases: only with the ~$1180\ nm$ chip lasing, only with the ~$980\ nm$ chip lasing, and with both chips lasing simultaneously. The 3D beam profiles for all cases are shown in Figure 6.2 and for each case the M^2 values were < 1.4, thus confirming the collinear alignment of the beams. Next the output power of generated green emission was

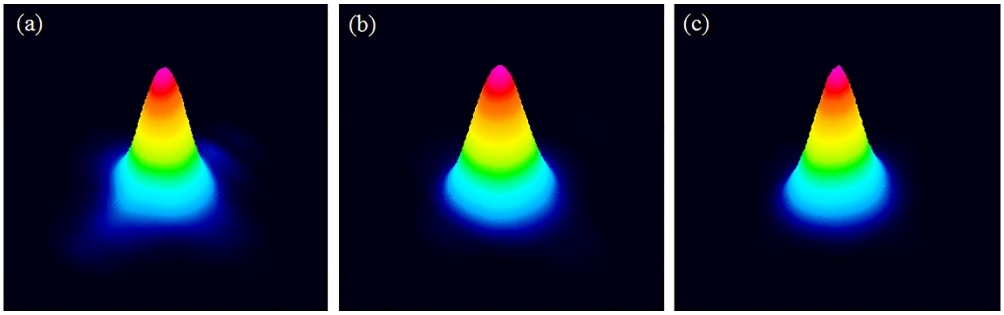

Figure 6.2 Beam profiles in the T-cavity VECSEL: (a) only ~$980\ nm$ output; (b) only ~$1180\ nm$ output; (c) collinear combined lasing modes. In all cases $M^2 < 1.4$.

characterized. The measurements were taken when the absorbed $808\ nm$ pump power was the same on each chip as illustrated graphically in Figure 6.3. A maximum of $2\ W$ was achieved. The green output tuning was accomplished by adjusting the birefringent filters in both arms

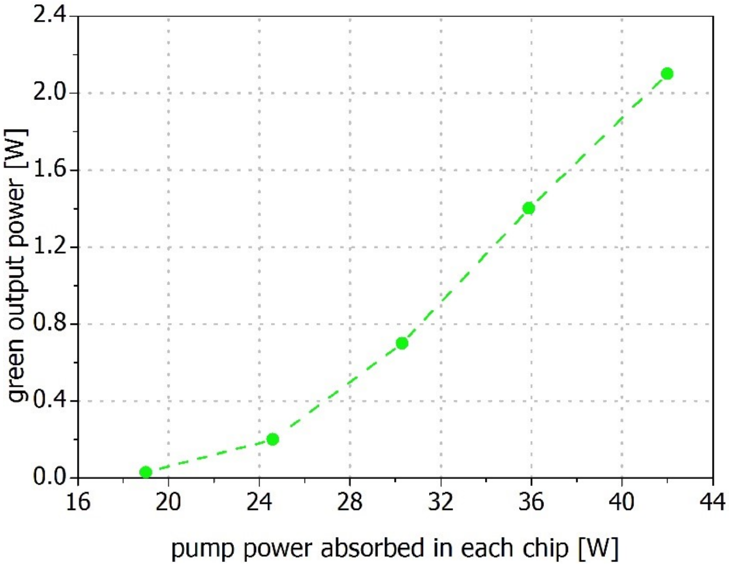

Figure 6.3 The type II SFG green output power characteristics in T-cavity VECSEL.

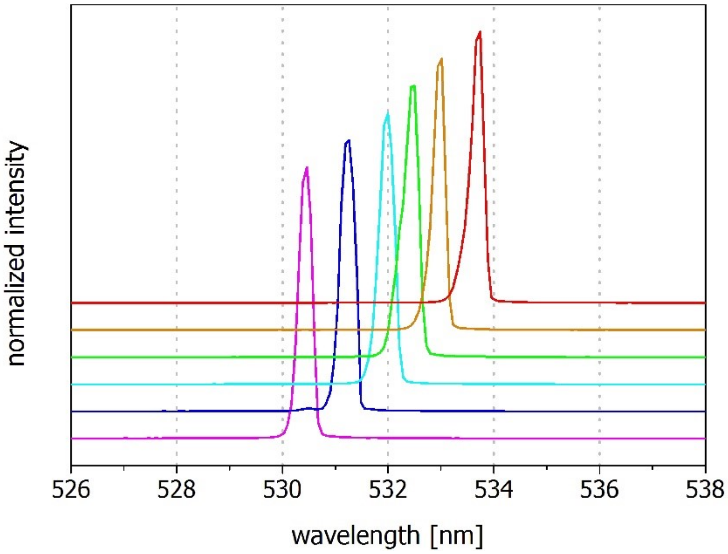

Figure 6.4 The green output tuning performed by adjusting the $2\ mm$ thick BF in both arms of the T-cavity.

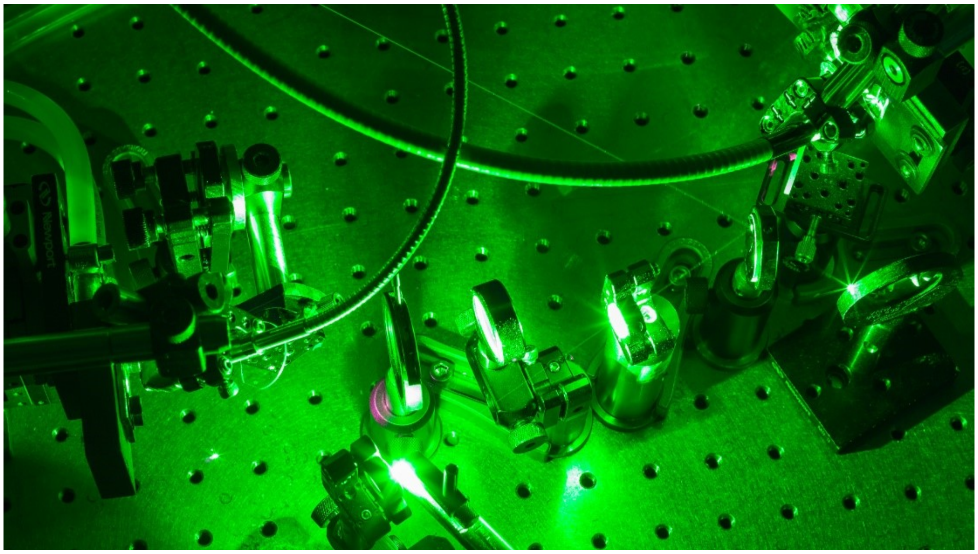

Figure 6.5 The picture of the SFG green output from T-cavity.

of the T-cavity. The T-cavity's tuning range of $5\ nm$ is presented in Figure 6.4. The picture of the VECSEL delivering green output is showcased in Figure 6.5.

6.2 Simultaneous SFG and SHG within T-cavity

6.2.1 Setup design

The exact same setup was modified to allow for simultaneous conversion to blue wavelengths via type I SHG and to green wavelengths via type II SFG. The altered setup is presented in Figure 6.6. About $1\ cm$ way from the flat end mirror, a thin etalon partially coated for $\sim 1180\ nm$ is inserted. It acts as a simple filter for the $\sim 980\ nm$ circulating mode and as a $\sim 99\ \%$ reflective mirror for the $\sim 1180\ nm$ beam. Thus, a small region of high intensity $\sim 980\ nm$ mode exists. On the other hand, the circulating $\sim 1180\ nm$ lasing mode suffers an additional $1\ \%$ loss. An LBO crystal was cut at angles $\theta = 90°$ and $\phi = 17°$ for blue generation with its

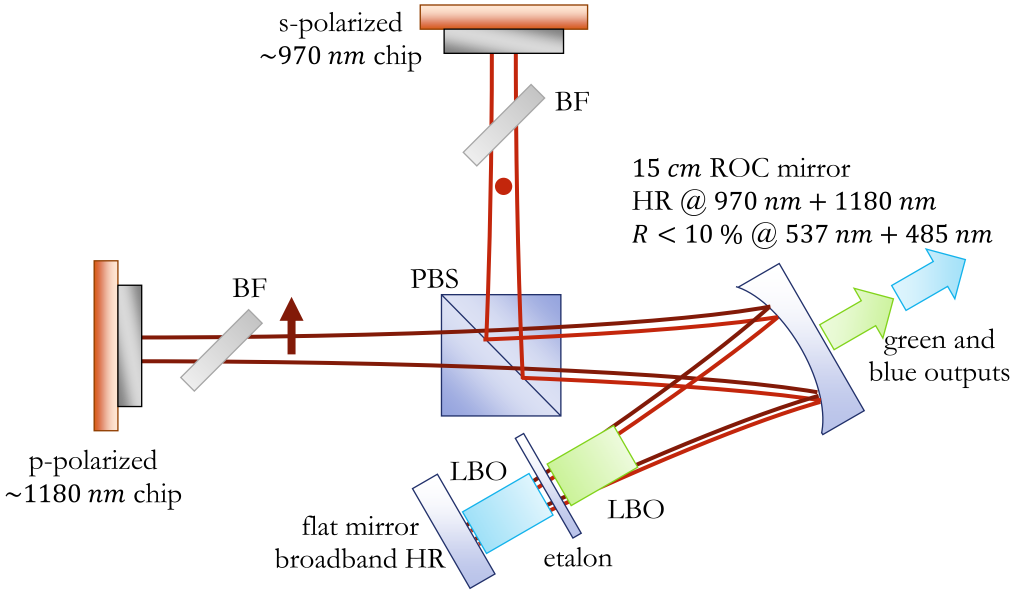

Figure 6.6 Schematic of a folded T-cavity VECSEL used for collinear type I SHG and type II SFG.

facets AR coated for fundamental and second harmonic wavelengths. This crystal was inserted between the end mirror and the etalon. On the other side of the etalon, the previously used LBO crystal was inserted. In this manner the circulating s-polarized fundamental mode can interact with both LBO crystals, while the p-polarized fundamental modes interacts only with the LBO designed for type II SFG.

6.2.2 Experimental results

For the optical pump power of $\sim 30\ W$ absorbed in each chip, the combined output of blue and green emission exceeded $450\ mW$. The lasing spectra of two simultaneous visible wavelengths is shown in Figure 6.7 with peaks at $\sim 490\ nm$ and $\sim 536\ nm$. The TEM$_{00}$ mode profiles of the generated beam are shown in Figure 6.8. A beam quality factor of $M^2 < 1.4$ for each individual beam was measured and the profile of the combined beams proves the

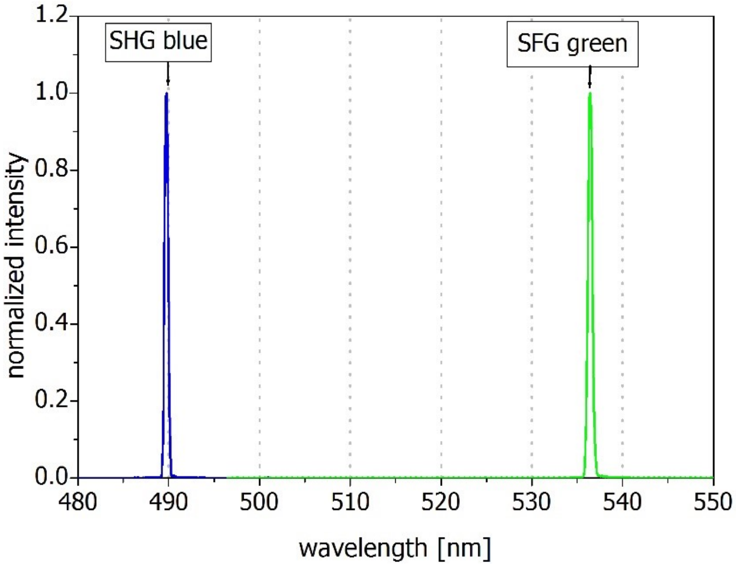

Figure 6.7 Spectra of simultaneous and collinear type I SHG blue and type II SFG green outputs.

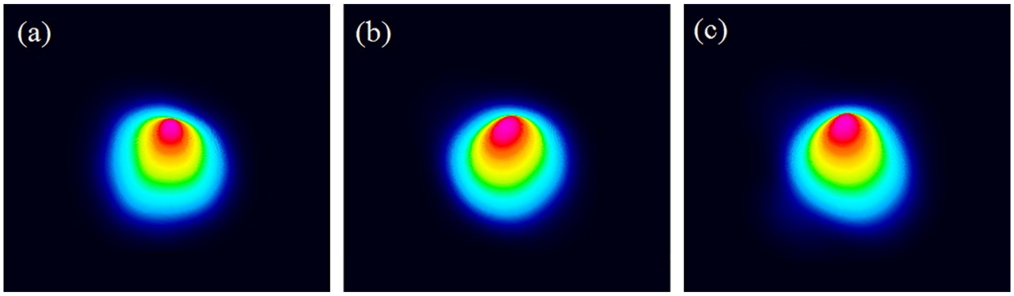

Figure 6.8 Beam profiles of (a) only blue output; (b) only green output; (c) collinear combined blue and green lasing modes, which were generated in T-cavity VECSEL.

collinear output was maintained. To showcase the mutlicolor operation of this cavity, three pictures were taken when: only the SFG crystal was inserted, only the SHG crystal was inserted and with both crystals were inserted. Figure 6.9 provides these captured images and blue, green and mixed blue and green (cyan) beams are visible.

The green output powers and tuning shown in these two experiments are not as satisfying as for the case of SHG described in previous chapter. There are a few factors which had a

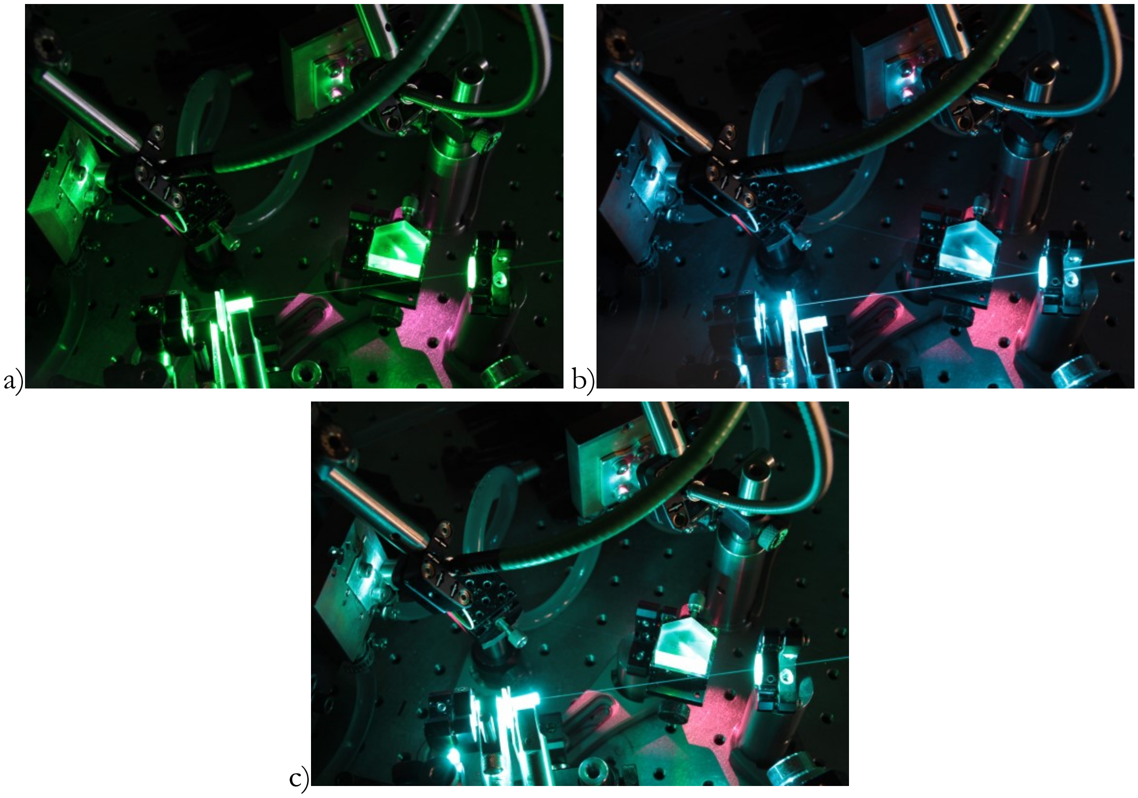

Figure 6.9 Pictures of the modified T-cavity VECSEL when: a) only the SFG crystal is inserted, b) only the SHG crystal is inserted, c) both crystals are inserted.

large influence on these results. Firstly, the chips used here come from an older wafer design with lower overall performance. Secondly, at the time of the experiment, a fold mirror with a proper radius of curvature was unavailable, thus the beam waist size at the LBO crystal was not optimal. And lastly, the d_{eff} for type II SFG is almost two times lower than that for SHG. However, with more efficient VECEL chips and optimized cavity design, a much improved result should be achievable.

Chapter 7 – Difference Frequency Generation in T-cavity VECSEL

In the previous chapter, the operation and flexibility of a folded T-cavity VECSEL was demonstrated with the example of sum frequency generation. Here, the main application for this cavity geometry is discussed. The fundamental pump and signal sources with wavelengths at $\sim 980\,nm$ and $\sim 1180\,nm$ are used for type II difference frequency generation with a silver thiogallate crystal as the nonlinear medium. A tunable mid-IR output around $\sim 5.4\,\mu m$ was achieved. Additionally, a setup with VECSEL chips, for which the wavelength separation was $\sim 1\,nm$, was utilized in an attempt to generate THz radiation in a periodically poled lithium triborate crystal.

7.1 Mid-infrared VECSEL

7.1.1 Setup design

In the experiment, a set of two VECSEL chips with active regions engineered to emit at $\sim 980\,nm$ and $\sim 1180\,nm$ was used. These chips come from the same wafers as in the SFG experiment, thus their structure design description can be found in Chapter 6. The copper heat sinks, to which the chips were clamped, were maintained at a temperature of $10℃$.

The T-cavity schematic is illustrated in Figure 7.1. Here, the polarizing beam splitter is replaced with a dichroic mirror, which was AR coated for $\sim 980\,nm$ and HR coated at $10°$

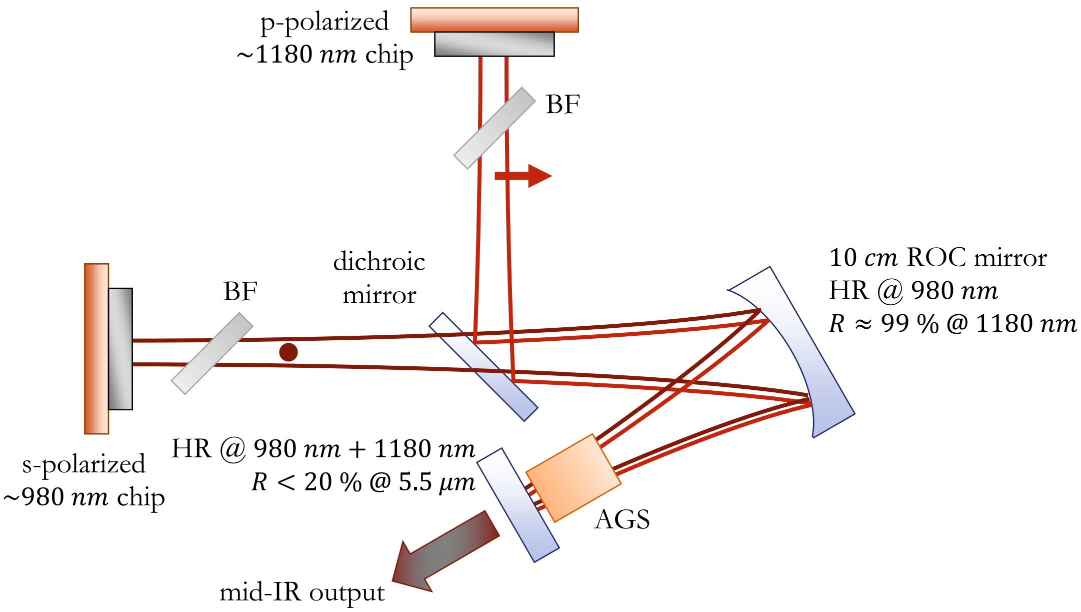

Figure 7.1 Schematic of a folded T-cavity VECSEL used for type II DFG.

incident angle for $\sim 1180\,nm$. During VECSEL operation, the intracavity losses introduced by the dichroic mirror are estimated to be $\sim 1\,\%$ and $\sim 0.5\,\%$ for $\sim 980\,nm$ and $\sim 1180\,nm$, respectively. The optical pumping was delivered by fiber coupled $808\,nm$ laser diodes, which were focused into the chips to a spot size diameter of $\sim 530\,\mu m$. The common fold mirror was broadband HR coated to cover both fundamental wavelengths and had $10\,cm$ ROC. The flat end mirror, which enclosed the cavity, was made of calcium fluoride (CaF_2) glass to ensure mid-IR transmission. The surface was HR coated for $\sim 980\,nm$, $\sim 99\ \%$ at $\sim 1180\,nm$ and $\sim 20\ \%$ reflective at $\sim 5.4\,\mu m$. The distance between each chip and the curved mirror was $\sim 15\ cm$, thus providing a beam waist diameter at the flat mirror of $\sim 120\,\mu m$ for both fundamental modes. The length of the shorter arm was $\sim 6\,cm$, so that the beam size on the chips would match the pump spot size, thus ensuring fundamental TEM_{00} mode lasing operation. Each independent arm of the T-cavity contained $1\,mm$ thick birefringent filters, which were oriented in s-polarization and p-polarization for $\sim 980\,nm$ and $\sim 1180\,nm$ beams, respectively. The BFs allowed for wavelength narrowing and independent wavelength tuning. The nonlinear element in the cavity was a silver thiogallate crystal placed in the collinear region of the cavity, near the beam waist of the Gaussian beams. The AGS crystal dimensions were $5 \times 5 \times 5\ mm$ and its facets were AR coated for pump and signal wavelengths. A $< 10\ \%$ reflective coating for the mid-IR wavelength was also applied. The type II DFG phase-matching required the crystal to be cut at the angle $\theta = 47°$ which resulted in $d_{eff} = 11.7\ pm/V$.

7.1.2 Experimental results

As in the previous case, the first step was to use the beam profiler to ensure collinear operation of the T-cavity. Figure 7.2 shows the profiles of the individual beams as well as both beams overlapping. In all cases the high beam quality was confirmed, with $M^2 < 1.4$.

The mid-IR wave in the AGS crystal was generated in both directions because of the double-pass of the fundamental waves, which is the same as in the SFG case. However, due to the mirrors used to construct the cavity, essentially only the beam coupled out through the CaF_2 mirror is utilized in the measurements. The output idler beam was then collimated with a CaF_2 lens and redirected into an optical spectrum analyzer to confirm that the wavelength

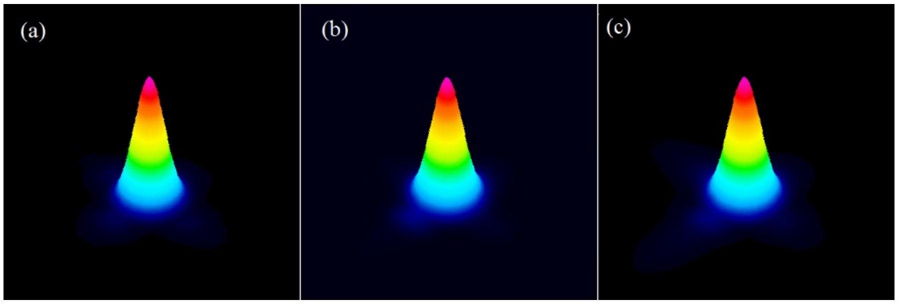

Figure 7.2 Beam profiles in T-cavity VECSEL: (a) only ~$980\ nm$ output; (b) only ~$1180\ nm$ output; (c) collinear combined lasing modes. In all cases $M^2 < 1.4$.

was the result of difference frequency generation. A high-resolution Bristol Instruments 721B XIR mid-IR laser spectrum analyzer was used, with a specified range of $2 - 12\,\mu m$ and a resolution of $\pm 1\, ppm$ [104], which was very well suited for the measurements. The spectra of the fundamental lasing modes were measured first to ensure proper separation between pump and signal wavelengths. The plot in Figure 7.3 demonstrates the fundamental peaks at $\sim 967\, nm$ and $\sim 1180\, nm$, which lead to a difference of $\sim 213\, nm$. With the emission fixed at these wavelengths, the spectrum of the mid-IR wave was captured. Figure 7.4 showcases emission at $\sim 5358\, nm$, which matches the expected value.

Before measuring the output power, it was also necessary to reject any remaining fundamental power leaking through the flat end mirror, while preserving high transmission for the mid-IR output. A germanium (Ge) filter was the best choice due its high absorption at the pump and signal wavelengths. Additionally, an AR coating for $4 - 12\,\mu m$ range allowed the filter to transmit $\sim 95\,\%$ of the DFG output wave. The Ge filter was placed after the CaF_2 lens and the idler beam power was measured without being altered by the collinear pump and signal

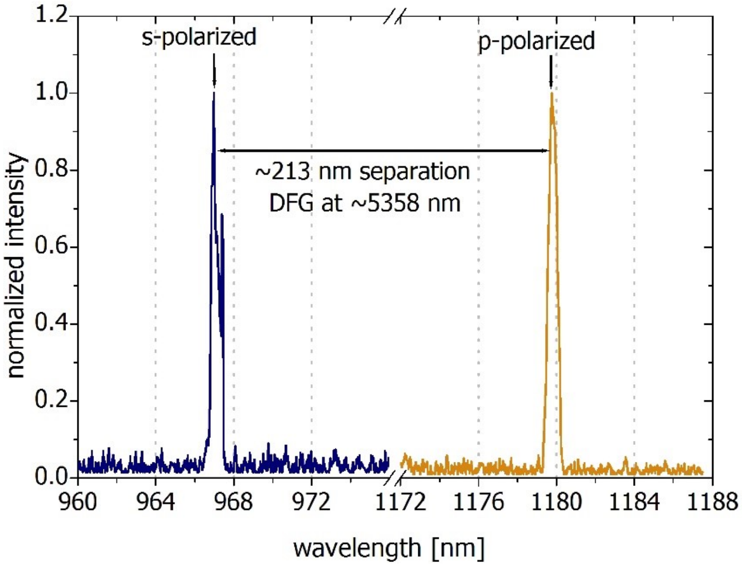

Figure 7.3 The independently tunable s-polarized pump and p-polarized signal spectra utilized for type II DFG.

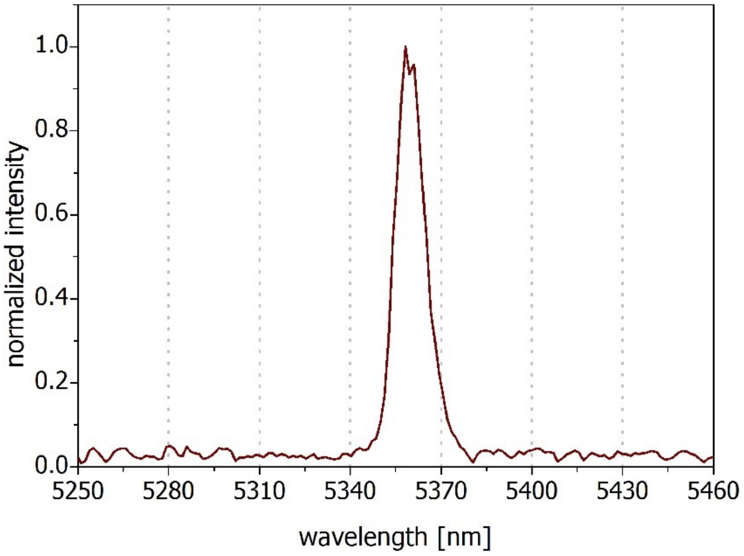

Figure 7.4 Mid-IR emission at $\sim 5358\ nm$ corresponding to $\sim 213\ nm$ separation of the fundamental waves.

beams. A high sensitivity thermopile detector was used to obtain the data points. The power characteristics are presented in Figure 7.5, where the mid-IR output is plotted against the pump power absorbed in each chip. A maximum value of over $5\ mW$ was achieved at $\sim 30\ W$ optical pump power. The circulating intracavity power could be estimated by measuring the residual power leaking through the HR mirror. This allowed determination of the power of the pump and signal waves interacting in the nonlinear crystal. Thanks to this, equation 4.39 in Chapter 4 was used to estimate the idler power generated in the AGS crystal. In the Figure 7.5, the plotted theoretical curve takes into account that the experimental values are $\sim 50\ \%$ smaller than the estimated ones as previously reported in [105]. The mid-IR beam saw multiple losses from the output coupler mirror, along with Fresnel reflections at the CaF_2 lens and Ge filter, which were estimated to be $\sim 40\ \%$. If this is considered, the new wavelength power generated in the AGS crystal, which is also plotted in Figure 7.5, is in reasonable agreement with the computed values.

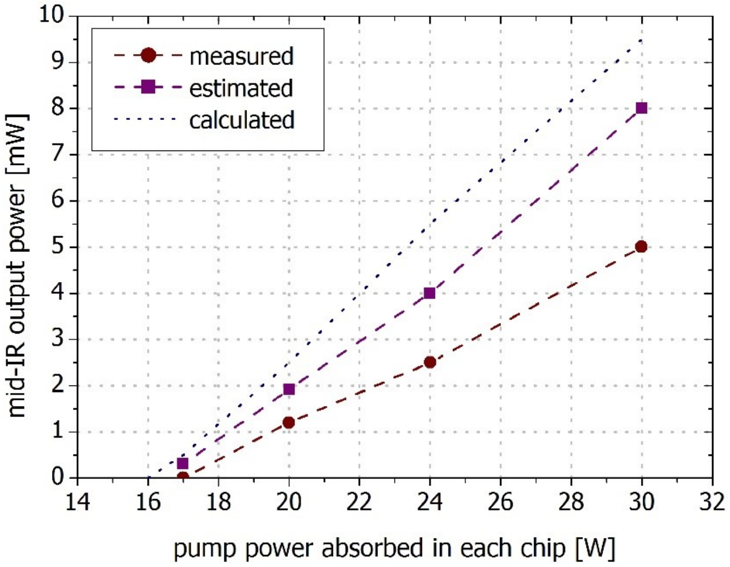

Figure 7.5 The ~$5358\ nm$ measured output power compared to the power generated in AGS crystal considering ~$40\ \%$ losses and the calculated theoretical output.

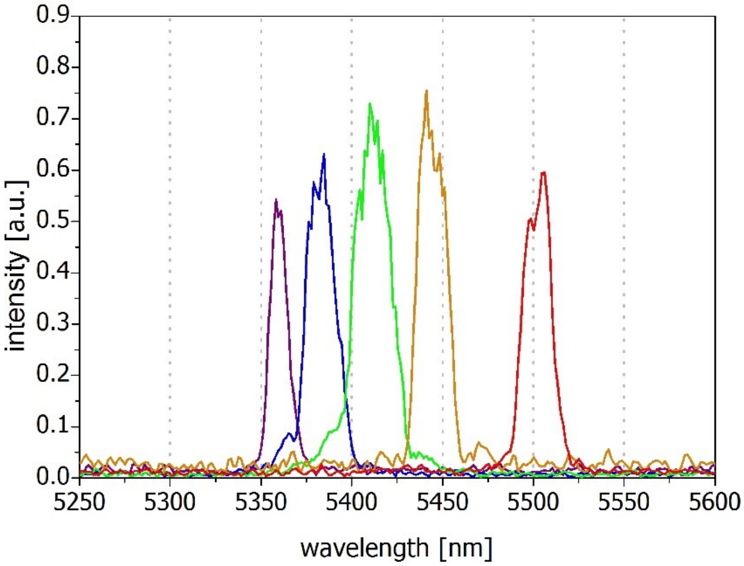

Figure 7.6 Tunability of the mid-IR output from the T-cavity VECSEL.

Lastly, the BFs in both the pump and signal wavelength arms are rotated in order to obtain the tuning spectra of the DFG wavelength. Figure 7.6 presents the mid-IR lasing peaks when ~$30\ W$ pump power was absorbed into each chip. The idler wavelength values ranged from

$\sim 5.35\,\mu m - 5.5\,\mu m$, thus continuous tunability over a $150\,nm$ range was achieved. The photo of the whole setup used it this experiment is shown in Figure 7.7. The T-cavity VECSEL is at the bottom of the picture, the collimating lens and two flat silvered mirrors used to direct the mid-IR beam into the spectrum analyzer are all also visible.

The tunable mid-IR output power delivered via type II DFG in the folded T-cavity VECSEL demonstrated here was obtained with available optical elements which were far from optimal. All of the coatings on the mirrors and AGS crystal did not allow extraction of the $\sim 5.4\,\mu m$ beam efficiently. In addition, for efficient frequency conversion, the $5\,mm$ long nonlinear crystal requires a much smaller beam waist compared to the one used in this experiment.

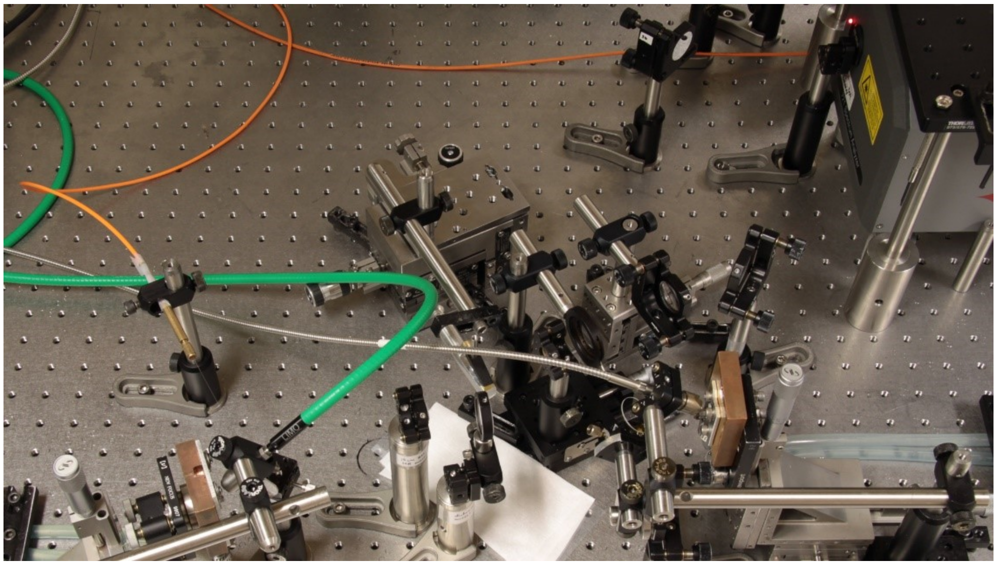

Figure 7.7 Picture of the setup used in the mid-IR VECSEL experiment: T-cavity at the bottom of the picture followed by additional optics and spectrum analyzer used for wavelength characterization.

7.2 THz VECSEL

7.2.1 Setup design

Difference frequency generation to the THz region requires fundamental wavelength separation of just a few nanometers, thus the two chips used in this experiment were cleaved from the $\sim 980\ nm$ wafer of the same design as previously mentioned. In order to separate the pump and signal arms of the T-cavity, a polarizing beam splitter had to be used. Here, full advantage of the PBS is taken, since it is the only way to make two VECSEL sources with a small wavelength gap independently tunable. Thus, the cavity geometry is very similar to the one presented in Figure 7.1, or the one used for SFG in Chapter 6. Both chips were maintained at $15℃$ while optically pumped with an $808\ nm$ laser diode. The spot diameter on each chip was $\sim 380\ \mu m$, and in the common region of the cavity, the collinear beams were refocused to $\sim 200\ \mu m$ diameter beam waist. The use of a $15\ cm$ ROC fold mirror required the longer arm

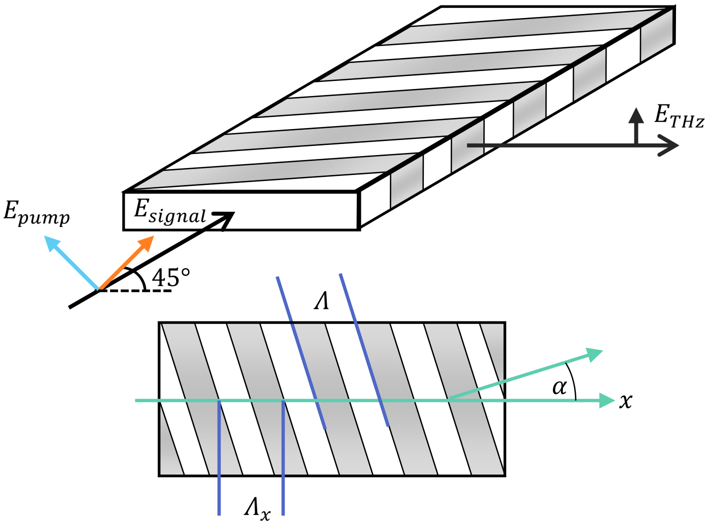

Figure 7.8 Schematic of the periodically poled crystal with incident beams polarized at $45°$ and the perpendicular emission of the THz beam; the top view shows the defined poling angle and poling period.

of the cavity to be $\sim 15\ cm$ and the shorter arm to be $\sim 11\ cm$ to support these spot sizes. Both the fold mirror and the flat end mirror were HR coated for $\sim 980\ nm$ to obtain high circulating power. Due to the low absorption coefficient at the fundamental wavelength, magnesium oxide doped periodically poled lithium niobate nonlinear crystal was used. While this material provides a large nonlinear coefficient, the high absorption in the THz region requires that the idler emission is collected perpendicular to the circulating fundamental modes. Since the pump and signal are orthogonally polarized with respect to each other, type II DFG has to be utilized. This puts an additional requirement for the fundamental waves to have their polarizations at $45°$ from the y-direction. The propagation and polarization of pump, signal, and idler beams in the MgO:PPLN is schematically shown in Figure 7.8. In this case the effective nonlinear coefficient was calculated to be $6.5\ pm/V$. To fulfill the phase-matching, the MgO:PPLN crystal had a poling period of $\Lambda = 57.2\ \mu m$ and a poling angle of $\alpha = 67°$, as defined in Figure 7.8. Once again, the alignment of the fundamental beams was confirmed with the scanning-slit beam profiler.

7.2.2 Experimental results

As the MgO:PPLN crystal was inserted into the common region of the cavity, with the use of the BFs, the pump wavelength was set to $\sim 979\ nm$ while the signal wavelength was tuned to $\sim 982\ nm$. The lasing spectra of the fundamental beams are shown in Figure 7.9. The obtained $\sim 3\ nm$ separation corresponded to the new DFG frequency of $\sim 0.93\ THz$.

The output power was measured using a Gentec THz thermopile power meter detector calibrated in the THz spectral range [106]. In order to prevent the measurement of any stray light, the power meter was cover with black polyethylene plastic, which is highly absorptive in

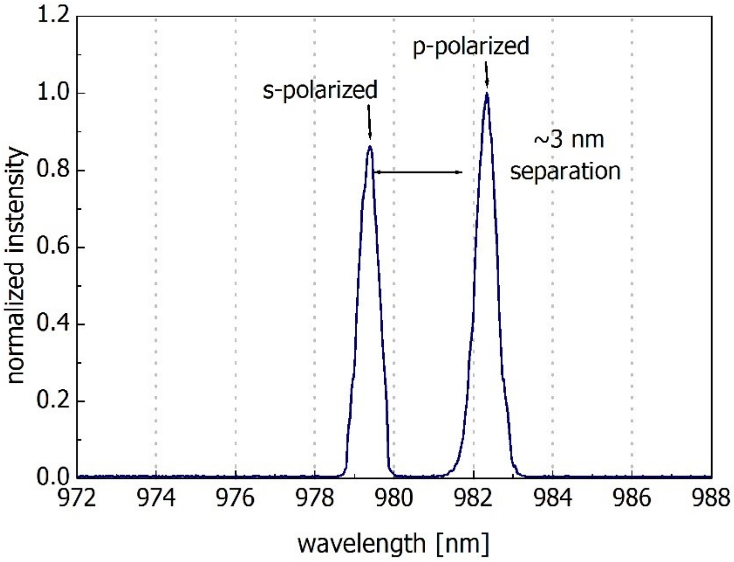

Figure 7.9 The pump and idler wavelength spectra with separation of $\sim 3\ nm$, used for difference frequency generation of $\sim 0.93\ THz$ output.

the IR range but transmits THz. The detector was placed in close proximity to the nonlinear crystal and oriented such that the THz beam would be at normal incidence to the detector's surface. During all of the measurements, the pump power of $\sim 28\ W$ and $\sim 24\ W$ was absorbed into the s-polarized and p-polarized chips, respectively. A directional output of $4.42\ mW$ was measured. To ensure the emission was propagating from the crystal, the power meter was passed over the crystal causing the measured power to drop. This, however, was not the THz output power as the detector is very sensitive to the thermal heat generated by the optical pumping of the VECSEL chips. A series of tests were performed in order to verify type II DFG in the MgO:PPLN crystal. When the s-polarized cavity arm was blocked with an aperture to shut off the lasing, the power reading dropped to $2.8\ mW$. Similarly, when the p-polarized cavity was blocked while the s-polarized mode was lasing, the power meter indicated $3.03\ mW$. In addition, the T-cavity was purposely misaligned to reduce the beam overlap at the nonlinear crystal, which resulted in the decrease of the power measured by the THz detector. These effects prove the DFG interaction occurred, though the accurate measurement of the THz beam power could not be performed, due to the high thermal sensitivity of the detector and the complicated orientation of the MgO:PPLN crystal. On the other hand, based on the estimated intracavity circulating power of $300\,W$, the expected idler output power could be calculated. At this power level, the THz output should have exceeded $500\,\mu W$.

To summarize, the two chip T-cavity VECSEL is capable of difference frequency generation to a tunable mid-IR or THz region based on the set of chips utilized in the setup. The chips used in the described experiments were cleaved from the older wafers whose performance was lacking as mentioned previously in Chapter 2. If the newer wafers were available at the time of the experiments, the results should have been more encouraging.

Chapter 8 – Fourth Harmonic Generation in modified T-cavity VECSEL

Fourth harmonic generation can be utilized to achieve emission in the UV spectral range for the case when the fundamental wavelength is in the IR region. This first lasing in the visible spectrum, which in the case of VECSELs is obtained by intracavity SHG. Next, in most cases, the visible light is coupled into an external bowtie cavity, which contains a nonlinear crystal for further up-conversion into UV radiation. Efficient coupling requires a locking technique to actively stabilize the bowtie cavity [23]. Thus, additional electronic equipment is required, adding bulk to the whole setup. Here, a modified T-cavity geometry with a single VECSEL chip is used. An intracavity polarizing beam splitter allows extraction of the second harmonic green light from the fundamental beam and provides a simple resonant cavity for green radiation buildup. Thus, conversion to the deep UV is accomplished.

8.1 Setup design

This experiment involves a VECSEL chip cleaved from a $1070\ nm$ wafer. The fabrication steps remained the same as previously described. The active region consisted of 12 compressive strained $8\ nm$ thick InGaAs MQWs, with a GaAsP strain compensating layer. Since the "bottom emitter" design is used, 25 pairs of alternating AlGaAs/AlAs layers were grown on top of the active region and served as a high reflectivity (~$99.9\ \%$) DBR. Resonant periodic gain was also supported. The chip was mounted to a water cooled copper heat sink and was kept at $10℃$.

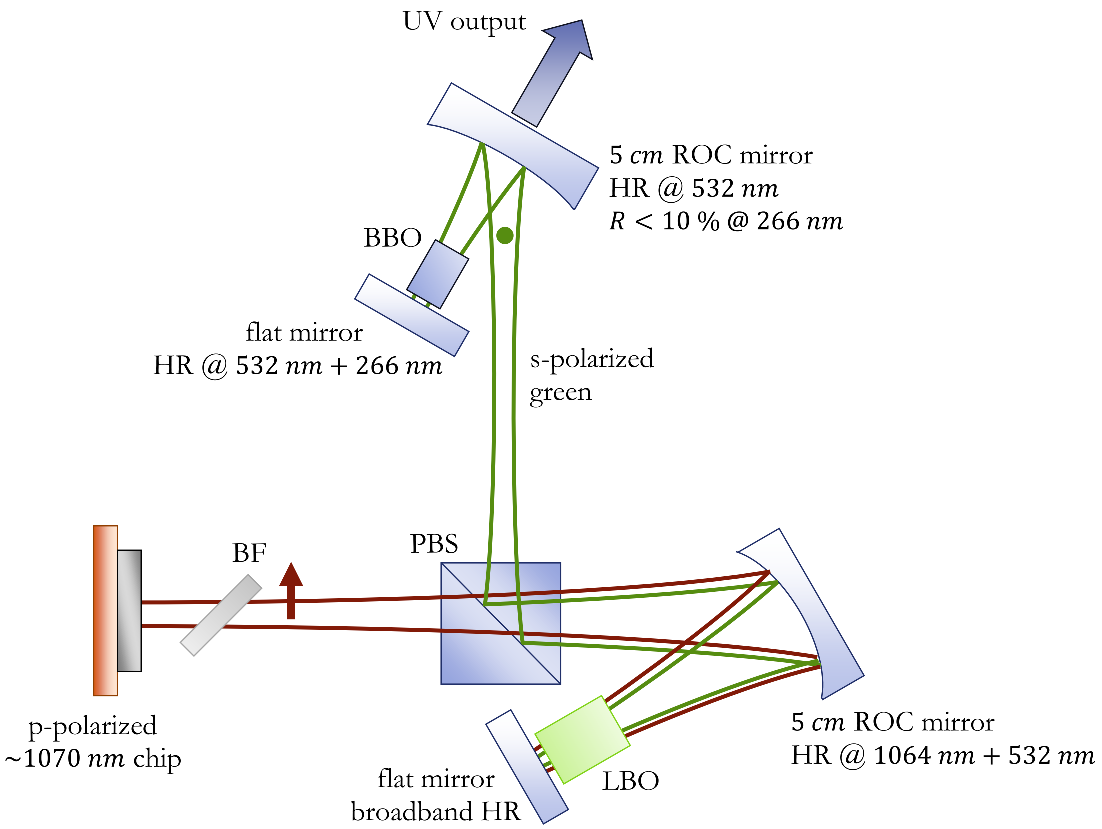

Figure 8.1 Schematic of modified T-cavity VECSEL used for type FHG to UV.

The schematic of the setup used is shown in Figure 8.1. The fundamental cavity utilized a V-folded geometry with a $5\ cm$ ROC fold mirror HR coated for both $1064\ nm$ and $532\ nm$ wavelengths. A flat broadband HR mirror enclosed the resonator. The $808\ nm$ pump spot diameter on the chip was $\sim 400\ \mu m$. To ensure a TEM_{00} circulating mode, the longer cavity arm was $\sim 9\ cm$ long, whereas the shorter arm was $\sim 3\ cm$ long. In addition, these resonator dimensions provided optimal focusing for the nonlinear crystal placed in proximity to the flat end mirror, where the beam waist diameter was $\sim 80\ \mu m$. A $3\ mm$ thick birefringent filter was utilized for maintaining p-polarization and wavelength narrowing of the fundamental mode. A $3 \times 3 \times 15\ mm^2$ lithium triborate crystal with both facets AR coated for fundamental and second harmonic wavelengths was utilized. The phase matching angles $\theta = 90°$ and $\phi = 11°$

were chosen to realize type I SHG, which resulted in an effective nonlinear coefficient of $0.8\ pm/V$. During the conversion process, the new wave obtains a polarization orthogonal to the one of the input waves, thus the polarizing beam splitter can be used as the output coupler for the green light. The PBS with all of its sides broadband AR coated was placed in the fundamental cavity. While the $\sim 1070\, nm$ p-polarized field could pass unhindered through the PBS, the $\sim 535\, nm$ s-polarized mode was reflected off to the side.

A second resonant cavity was built for this green lasing mode. A second mirror with $5\, cm$ ROC was used to refocus the green beam onto the flat mirror which enclosed the cavity. To utilize the double pass through the UV nonlinear crystal, the flat mirror was HR coated for both $532\, nm$ and $266\, nm$, whereas the fold mirror was HR coated for both $532\, nm$ and low reflectivity ($R < 10\ \%$) coated at $266\, nm$. The distance separating the two curved mirrors was $\sim 14\, cm$, whereas the second fold mirror and the flat end mirror were $\sim 2.5\, cm$ apart. These dimensions were chosen to maintain the green transverse mode size at the fundamental cavity end mirror, whereas at the second flat mirror the green beam waist was $\sim 70\, \mu m$ in diameter. At this position a $3 \times 3 \times 10\, mm^3$ beta barium borate crystal was placed. The cut for type I SHG from $532\, nm$ to UV required angles $\theta = 47°$ and $\phi = 0°$ and the crystal facets were AR coated for these wavelengths to minimize the losses. The nonlinear coefficient in this case was $1.8\ pm/V$.

8.2 Experimental results

The first step in the experiment was to achieve optimal conversion to green in the LBO crystal. The output power of green light was measured after the reflection of the PBS and it was equal to $\sim 12\, W$ for an optical pump power of $\sim 48\, W$. After the green resonant cavity

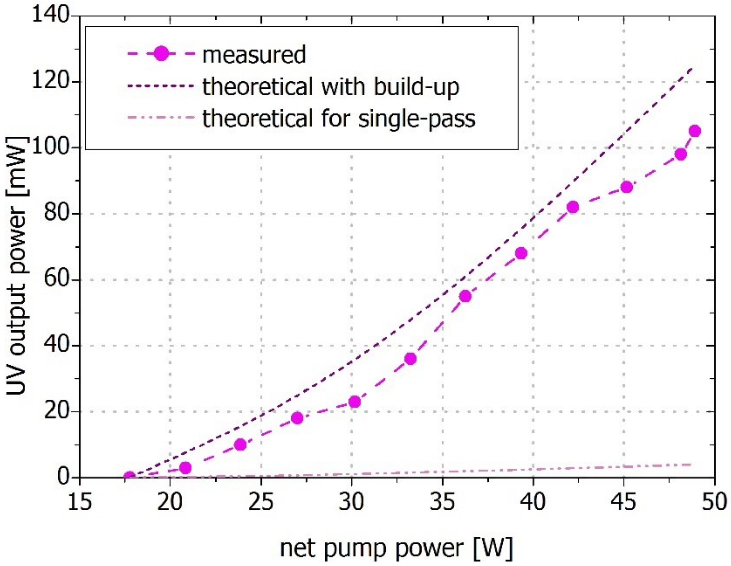

Figure 8.2 The characteristics of the UV output power achieved via fourth harmonic generation in T-cavity VECSEL.

was adjusted, the residual power leaking through the flat end mirror was measured with a thermal power detector in order to estimate the buildup of the circulating green light. Since the system lacked of any stabilization scheme, the measured power was not stable, but the estimated circulating power of $\sim 48\ W$ was consistent, thus resulting in a four times buildup of the green.

The UV output power characteristics are presented in Figure 8.2. The measured UV power is plotted against the $808\,nm$ pump power absorbed in the chip. The maximum cw power exceeded $100\ mW$ at $265\ nm$. In addition, Figure 8.2 presents the theoretical values of output power calculated based on the equations provided in Chapter 4. The experimental results stand in good agreement with the estimated power. Also, for comparison, the estimated UV power is plotted for the case of a single pass through the crystal with a beam of similar characteristics. It is noticeable that even without any stabilization, the green cavity provides much better results. At the maximum power level, the conversion efficiency from the optical pump to UV

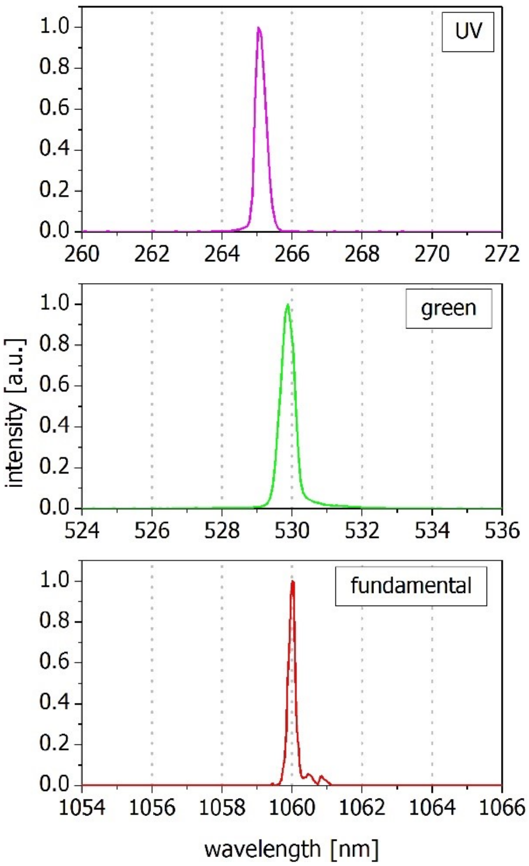

Figure 8.3 The optical spectra of the fundamental, second harmonic and fourth harmonic signals in T-cavity VECSEL.

was $\sim 0.25\ \%$. Such low efficiency is mostly due to lack of any type of stabilization as well as a lack of single frequency operation of the green wave. Moreover, the available mirrors did not allow achievement of an optimal beam waist size for the green Gaussian beam at the BBO crystal.

Finally, as a proof of proper frequency conversion, Figure 8.3 illustrates the optical spectra measured for fundamental, second harmonic and fourth harmonic wavelengths. As expected, the fundamental wavelength of $\sim 1060\ nm$ resulted in $\sim 265\ nm$ in the UV region.

A modified, single chip T-cavity VECSEL was demonstrated as a bowtie cavity alternative to achieve UV outputs by the means of fourth harmonic generation. Over $100\ mW$ of cw output at $265\ nm$ was produced. If a stabilization method is introduced, the second harmonic light buildup should be an order of magnitude higher, thus increasing the UV conversion efficiency into tens of percent [23]. As in previous cases, the flexibility of VECSELs allows for further power scaling, usage of different gain materials to reach different UV wavelengths, single frequency operation with an additional Fabry-Perot etalon, or tunable UV output. Moreover, the stabilized and fully optimized VECSEL geometry of this sort should make deep UV laser sources exceeding $1\ W$ of output power feasible.

Chapter 9 – Conclusion and Future Work

Since the first demonstration of a linear cavity VECSEL in 1997, their complexity has been greatly expanded. In the past 20 years it has been confirmed that high power operation with high fundamental beam quality is achievable, thanks to power scaling, lasing cavity optimization, and careful gain chip fabrication. A wide range of available group III-V semiconductor compounds allows for bandgap engineering to achieve emission in the desired wavelength spectrum. Moreover, the ability to utilize nonlinear optical effects in VECSELs expands the range of applications even further. Novel designs of VECSEL cavities, utilizing various nonlinear frequency conversion techniques, have been extensively investigated in this dissertation.

The folded T-cavity geometry was presented as a flexible foundation for every type of nonlinear frequency generation. The pair of VECSEL gain chips utilized in the setup can be chosen freely, thus the wavelength separation between fundamental emission wavelengths can range from sub-nanometer to a few hundreds of nanometers. Here, bottom emitter VECSEL structures designed to operate at wavelengths of $\sim 980\, nm$ and $\sim 1180\, nm$ were used. The frequency separation between these heterostructures was exploited and type II difference frequency generation to provide mid-IR output at $\sim 5.4\, \mu m$ was demonstrated. By reducing the wavelength difference to a few nanometers, the first attempt to produce a signal in THz range was presented. On the opposite side of frequency spectrum, a $\sim 1070\, nm$ emission single chip modified T-cavity was utilized to demonstrate fourth harmonic generation to the UV range. This compact setup could be a viable alternative for commonly used bowtie cavity laser setups used for UV generation. In addition, upon acquiring new, more efficient VECSEL wafers designed for fundamental lasing at $\sim 970\ nm$ and $\sim 1070\ nm$, well optimized folded V-cavities were capable of delivering over $16\ W$ and $21\ W$ of cw type I second harmonic generated blue and green output power, respectively.

The unique properties of the two chip T-cavity VECSEL design has the most potential in the case of difference frequency generation although current performance is low. As the result of the two separated regions in the T-cavity, the capability to independently tune both fundamental wavelengths has a great advantage over other laser sources. This feature could allow development of a THz laser source that is continuously tunable over tens of THz. In case of mid-IR emission, with new nonlinear crystals, such as orientation patterned gallium phosphate, a laser source covering the range up to $12\ \mu m$ is in sight. Moreover, since the wavelength separation can be tailored to be in the tens of microns, the far IR region could be fully accessible. With more efficient gain chips and optimized conversion in the nonlinear crystal, watt levels of mid-IR output and hundreds of milliwatts THz output should be realizable.

The single chip T-cavity VECSEL, modified to enable fourth harmonic generation for deep UV emission with an incorporated stabilization technique, should allow achievement of Watt levels of output power. The birefringent filter or etalon intracavity elements could be utilized as well, if single frequency or tunable output is desired.

In the case of the visible light generation, the system could be expanded to a multiple chip cavity and longer nonlinear crystals could be introduced. If the VECSEL structures are further optimized to a specific task, visible output powers far beyond $50\ W$ should be attainable.

Additionally, all of these cavity geometries can be further expanded to provide pulsed operation. The free-space laser resonator design leaves room to incorporate saturable absorber mirrors into the cavity for mode-locking purposes. Mode-locking has been a well-established technique for achieving femtosecond or picosecond pulses from IR VECSELs, although it has not yet been used simultaneously with DFG or FHG.

Overall, the flexibility which comes from both the cavity and heterostructure design of the VECSELs makes them a laser source with operational features that can be tailor-made to provide a solution to specific applications. The nonlinear frequency conversion techniques incorporated in the VECSEL platform increase the range of possibilities even further.

References

[1] Coldren, L.A., Corzine, S.W. and Mashanovitch, M.L., 2012. *Diode lasers and photonic integrated circuits* (Vol. 218). John Wiley & Sons.

[2] Kuznetsov, M., Hakimi, F., Sprague, R. and Mooradian, A., 1997. High-power (> 0.5-W CW) diode-pumped vertical-external-cavity surface-emitting semiconductor lasers with circular TEM_{00} beams. *Photonics Technology Letters, IEEE*, *9*(8), pp.1063-1065.

[3] Kuznetsov, M., Hakimi, F., Sprague, R. and Mooradian, A., 1999. Design and characteristics of high-power (> 0.5-W CW) diode-pumped vertical-external-cavity surface-emitting semiconductor lasers with circular TEM_{00} beams. *Selected Topics in Quantum Electronics, IEEE Journal of*, *5*(3), pp.561-573.

[4] Agrawal, G.P. and Dutta, N.K., 1986. *Long wavelength semiconductor lasers*.

[5] Zory, P.S., 1993. *Quantum well lasers*. Academic Press.

[6] Soda, H., Iga, K.I., Kitahara, C. and Suematsu, Y., 1979. GaInAsP/InP surface emitting injection lasers. *Japanese Journal of Applied Physics*, *18*(12), p.2329.

[7] Jewell, J.L., Harbison, J.P., Scherer, A., Lee, Y.H. and Florez, L.T., 1991. Vertical-cavity surface-emitting lasers: design, growth, fabrication, characterization. *IEEE Journal of Quantum Electronics*, *27*(6), pp.1332-1346.

[8] Diehl, R. ed., 2003. *High-power diode lasers: fundamentals, technology, applications* (Vol. 78). Springer Science & Business Media.

[9] Crump, P., Wenzel, H., Erbert, G. and Tränkle, G., 2012, February. Progress in increasing the maximum achievable output power of broad area diode lasers. In *SPIE LASE* (pp. 82410U-82410U). International Society for Optics and Photonics.

[10] Pfeil, A.V. and von Freyhold, T., 2002, April. Beam shaping of broad-area diode lasers: principles and benefits. In *Symposium on Integrated Optoelectronic Devices* (pp. 82-90). International Society for Optics and Photonics.

[11] Kapon, E., 1999. *Semiconductor Lasers II: Materials and Structures*. Academic Press.

[12] Grabherr, M., Miller, M., Jäger, R., Michalzik, R., Martin, U., Unold, H.J. and Ebeling, K.J., 1999. High-power VCSELs: single devices and densely packed 2-D-arrays. *Selected Topics in Quantum Electronics, IEEE Journal of*, *5*(3), pp.495-502.

[13] Wilmsen, C.W., Temkin, H. and Coldren, L.A., eds. 1999. Vertical-cavity surface-emitting lasers. *Cambridge University Press.*

[14] Chilla, J., Shu, Q.Z., Zhou, H., Weiss, E., Reed, M. and Spinelli, L., 2007, February. Recent advances in optically pumped semiconductor lasers. In *Lasers and Applications in Science and Engineering* (pp. 645109-645109). International Society for Optics and Photonics.

[15] Ranta, S., Tavast, M., Leinonen, T., Van Lieu, N., Fetzer, G. and Guina, M., 2013. 1180 nm VECSEL with output power beyond 20 W. *Electronics Letters*, *49*(1), pp.59-60.

[16] Wang, T.L., Heinen, B., Hader, J., Dineen, C., Sparenberg, M., Weber, A., Kunert, B., Koch, S.W., Moloney, J.V., Koch, M. and Stolz, W., 2012. Quantum design strategy pushes high-power vertical-external-cavity surface-emitting lasers beyond 100 W. *Laser & Photonics Reviews*, *6*(5), pp. L12-L14.

[17] Bedford, R.G., Dang, T. and Tomich, D., 2012, February. Recent VECSEL developments for sensors applications. In *SPIE LASE* (pp. 82420W-82420W). International Society for Optics and Photonics.

[18] Chilla, J.L., Butterworth, S.D., Zeitschel, A., Charles, J.P., Caprara, A.L., Reed, M.K. and Spinelli, L., 2004, July. High-power optically pumped semiconductor lasers. In *Lasers and Applications in Science and Engineering* (pp. 143-150). International Society for Optics and Photonics.

[19] Fan, L., Fallahi, M., Hader, J., Zakharian, A.R., Moloney, J.V., Stolz, W., Koch, S.W., Bedford, R. and Murray, J.T., 2007. Linearly polarized dual-wavelength vertical-external-cavity surface-emitting laser. *Applied physics letters*, *90*(18), p.181-124.

[20] Hastie, Jennifer E., et al. "High power CW red VECSEL with linearly polarized TEM_{00} output beam." *Optics Express* 13.1 (2005): 77-81.

[21] Hopkins, J.M., Maclean, A.J., Burns, D., Riis, E., Schulz, N., Rattunde, M., Manz, C., Köhler, K. and Wagner, J., 2007. Tunable, Single-frequency, Diode-pumped 2.3 μm VECSEL. *Optics express*, *15*(13), pp.8212-8217.

[22] Khiar, A., Rahim, M., Fill, M., Felder, F., Hobrecker, F. and Zogg, H., 2010. Continuously tunable monomode mid-infrared vertical external cavity surface emitting laser on Si. *Applied Physics Letters*, *97*(15), p.151104.

[23] Kaneda, Y., Yarborough, J.M., Li, L., Peyghambarian, N., Fan, L., Hessenius, C., Fallahi, M., Hader, J., Moloney, J.V., Honda, Y. and Nishioka, M., 2008. Continuous-wave all-solid-state 244 nm deep-ultraviolet laser source by fourth-harmonic generation of an

optically pumped semiconductor laser using CsLiB 6 O 10 in an external resonator. *Optics letters*, *33*(15), pp.1705-1707.

[24] Kim, T., Yoo, J., Kim, K., Lee, S., Lim, S., Kim, G., Kim, J., Cho, S., Lee, J. and Park, Y., 2006, February. 2 W continuous wave operation of optically pumped blue VECSEL with frequency doubling. In *Integrated Optoelectronic Devices 2006* (pp. 61320K-61320K). International Society for Optics and Photonics.

[25] Lee, J., Lee, S., Kim, T. and Park, Y., 2006. 7 W high-efficiency continuous-wave green light generation by intracavity frequency doubling of an end-pumped vertical external-cavity surface emitting semiconductor laser.*Applied physics letters*, *89*(24), p.1107.

[26] Hessenius, C., Guinet, P.Y., Lukowski, M., Moloney, J. and Fallahi, M., 2012, February. 589-nm single-frequency VECSEL for sodium guidestar applications. In *SPIE LASE* (pp. 82420E-82420E). International Society for Optics and Photonics.

[27] Kantola, E., Leinonen, T., Penttinen, J.P., Korpijärvi, V.M. and Guina, M., 2015. 615 nm GaInNAs VECSEL with output power above 10 W. *Optics express*, *23*(16), pp.20280-20287.

[28] Lukowski, M., Hessenius, C., Bedford, R. and Fallahi, M., 2015. Tunable type II intracavity difference frequency generation at 5.4 μm in a two chip vertical external cavity surface emitting laser. *Optics letters*, *40*(17), pp.4174-4177.

[29] Lukowski, M., Hessenius, C. and Fallahi, M., 2015. Widely Tunable High-Power Two-Color VECSELs for New Wavelength Generation. *Selected Topics in Quantum Electronics, IEEE Journal of*, *21*(1), pp.432-439.

[30] Hoogland, S., Dhanjal, S., Tropper, A.C., Roberts, J.S., Häring, R., Paschotta, R., Morier-Genoud, F. and Keller, U., 2000. Passively mode-locked diode-pumped surface-emitting semiconductor laser. *Photonics Technology Letters, IEEE*, *12*(9), pp.1135-1137.

[31] Scheller, M., Wang, T.L., Kunert, B., Stolz, W., Koch, S.W. and Moloney, J.V., 2012. Passively modelocked VECSEL emitting 682 fs pulses with 5.1 W of average output power. *Electronics letters*, *48*(10), p.1.

[32] Rudin, B., Wittwer, V.J., Maas, D.J.H.C., Hoffmann, M., Sieber, O.D., Barbarin, Y., Golling, M., Südmeyer, T. and Keller, U., 2010. High-power MIXSEL: an integrated ultrafast semiconductor laser with 6.4 W average power. *Optics express*, *18*(26), pp.27582-27588.

[33] Wilcox, K.G., Tropper, A.C., Beere, H.E., Ritchie, D.A., Kunert, B., Heinen, B. and Stolz, W., 2013. 4.35 kW peak power femtosecond pulse mode-locked VECSEL for supercontinuum generation. *Optics express*, *21*(2), pp.1599-1605.

[34] Keller, U. and Tropper, A.C., 2006. Passively modelocked surface-emitting semiconductor lasers. *Physics Reports*, *429*(2), pp.67-120.

[35] Gaafar, M., Möller, C., Wichmann, M., Heinen, B., Kunert, B., Rahimi-Iman, A., Stolz, W. and Koch, M., 2014. Harmonic self-mode-locking of optically pumped semiconductor disc laser. *Electronics Letters*, *50*(7), p.551.

[36] Kornaszewski, L., Maker, G., Malcolm, G.P.A., Butkus, M., Rafailov, E.U. and Hamilton, C.J., 2012. SESAM-free mode-locked semiconductor disk laser. *Laser & Photonics Reviews*, *6*(6), pp.L20-L23.

[37] Jacquemet, M., Domenech, M., Dion, J., Strassner, M., Lucas-Leclin, G., Georges, P., Sagnes, I. and Garnache, A., 2006, April. Single-frequency high-power continuous-wave oscillation at 1003 nm of an optically pumped semiconductor laser. In *Photonics Europe,* pp. 61841X-61841X.

[38] Holm, M.A., Burns, D., Ferguson, A.I. and Dawson, M.D., 1999. Actively stabilized single-frequency vertical-external-cavity AlGaAs laser. *Photonics Technology Letters, IEEE*, *11*(12), pp.1551-1553.

[39] Demtröder, W., 2013. *Laser spectroscopy: basic concepts and instrumentation*. Springer Science & Business Media.

[40] Berlien, H.P., Breuer, H., Müller, G.J., Krasner, N., Okunata, T. and Sliney, D., 2012. *Applied laser medicine*. Springer Science & Business Media.

[41] Okhotnikov, O.G. ed., 2010. *Semiconductor disk lasers: physics and technology*. John Wiley & Sons.

[42] Baker, C.E., 1968. Laser display technology. *Spectrum, IEEE*, *5*(12), pp.39-50.

[43] Raja, M.Y.A., Brueck, S.R., Osinski, M., Schaus, C.F., McInerney, J.G., Brennan, T.M. and Hammons, B.E., 1989. Resonant periodic gain surface-emitting semiconductor lasers. *Quantum Electronics, IEEE Journal of*, *25*(6), pp.1500-1512.

[44] Jones-Bey, H.A., 2001. Vertical cavity lasers-NECSEL technology unveiled at OFC.

[45] McInerney, J.G., Mooradian, A., Lewis, A., Shchegrov, A.V., Strzelecka, E.M., Lee, D., Watson, J.P., Liebman, M., Carey, G.P., Cantos, B.D. and Hitchens, W.R., 2003. High-

power surface emitting semiconductor laser with extended vertical compound cavity. *Electronics Letters*, *39*(6), p.1.

[46] Lutgen, S., Albrecht, T., Brick, P., Reill, W., Luft, J. and Späth, W., 2003. 8-W high-efficiency continuous-wave semiconductor disk laser at 1000 nm.*Applied Physics Letters*, *82*(21), pp.3620-3622.

[47] Tropper, A.C. and Hoogland, S., 2006. Extended cavity surface-emitting semiconductor lasers. *Progress in Quantum Electronics*, *30*(1), pp.1-43.

[48] Franken, P.A., Hill, A.E., Peters, C.E. and Weinreich, G., 1961. Generation of optical harmonics. *Physical Review Letters*, *7*(4), p.118.

[49] Glenn, W.E., 1997, January. Solid-State Light Sources for Color Projection. In *Advanced Solid State Lasers* (p. VL1). Optical Society of America.

[50] Kogure, T., Karasawa, S., Araki, T., Saito, K., Kinjo, M. and Miyawaki, A., 2006. A fluorescent variant of a protein from the stony coral Montipora facilitates dual-color single-laser fluorescence cross-correlation spectroscopy. *Nature biotechnology*, *24*(5), pp.577-581.

[51] Mayrhofer, R. and Welch, M., 2007, April. A human-verifiable authentication protocol using visible laser light. In *Availability, Reliability and Security, 2007. ARES 2007. The Second International Conference on* (pp. 1143-1148). IEEE.

[52] Wall, K. and Sanchez, A., 1990. Titanium sapphire lasers. *The Lincoln laboratory journal*, *3*(3), pp.447-462.

[53] Wheeland, R.G., 1995. Clinical uses of lasers in dermatology. *Lasers in surgery and medicine*, *16*(1), pp.2-23.

[54] Kojima, T., Fujikawa, S. and Yasui, K., 1999. Stabilization of a high-power diode-side-pumped intracavity-frequency-doubled CW Nd: YAG laser by compensating for thermal lensing of a KTP crystal and Nd: YAG rods. *IEEE journal of quantum electronics*, *35*(3), pp.377-380.

[55] Ling, Z., Yi, Y., Yang, Z. and Quan, Z., 2014. All-solid-state dual end pumped YVO4:Nd/LBO blue laser with 21.8 W output power at 457 nm. *Optics and Spectroscopy*, *116*(3), pp.470-472.

[56] Konno, S., Kojima, T., Fujikawa, S. and Yasui, K., 2000. High-brightness 138-W green laser based on an intracavity frequency doubled diode side pumped Q-switched Nd:YAG laser. *Optics letters*, *25*(2), pp.105-107.

[57] Metcalf, H.J. and Straten, P., 2007. *Laser cooling and trapping of neutral atoms*. Wiley-VCH Verlag GmbH & Co. KGaA.

[58] Kitai, M.S., Popkov, V.L., Semchischen, V.A. and Kharizov, A.A., 1991. The physics of UV laser cornea ablation. *IEEE journal of quantum electronics*,*27*(2), pp.302-307.

[59] Lin, B.J., 1975. Deep UV lithography. *Journal of Vacuum Science & Technology*, *12*(6), pp.1317-1320.

[60] Waynant, R.W., Ilev, I.K. and Gannot, I., 2001. Mid–infrared laser applications in medicine and biology. *Philosophical Transactions of the Royal Society of London A: Mathematical, Physical and Engineering Sciences*, *359*(1780), pp.635-644.

[61] Tittel, F.K., Richter, D. and Fried, A., 2003. Mid-infrared laser applications in spectroscopy. In *Solid-State Mid-Infrared Laser Sources* (pp. 458-529). Springer Berlin Heidelberg.

[62] Godard, A., 2007. Infrared (2–12 μm) solid-state laser sources: a review. *Comptes Rendus Physique*, *8*(10), pp.1100-1128.

[63] Ebrahim-Zadeh, M. and Sorokina, I.T., 2008. *Mid-infrared coherent sources and applications*. Springer Science & Business Media.

[64] Tacke, M., 2001. Lead–salt lasers. *Philosophical Transactions of the Royal Society of London A: Mathematical, Physical and Engineering Sciences*,*359*(1780), pp.547-566.

[65] Yao, Y., Hoffman, A.J. and Gmachl, C.F., 2012. Mid-infrared quantum cascade lasers. *Nature Photonics*, *6*(7), pp.432-439.

[66] Seddon, A.B., Tang, Z., Furniss, D., Sujecki, S. and Benson, T.M., 2010. Progress in rare-earth-doped mid-infrared fiber lasers. *Optics express*,*18*(25), pp.26704-26719.

[67] Chen, W., Cousin, J., Poullet, E., Burie, J., Boucher, D., Gao, X., Sigrist, M.W. and Tittel, F.K., 2007. Continuous-wave mid-infrared laser sources based on difference frequency generation. *Comptes Rendus Physique*, *8*(10), pp.1129-1150.

[68] Federici, J.F., Schulkin, B., Huang, F., Gary, D., Barat, R., Oliveira, F. and Zimdars, D., 2005. THz imaging and sensing for security applications—explosives, weapons and drugs. *Semiconductor Science and Technology*,*20*(7), p.S266.

[69] Song, H.J. and Nagatsuma, T., 2011. Present and future of terahertz communications. *IEEE Transactions on Terahertz Science and Technology*,*1*(1), pp.256-263.

[70] Mantsch, H.H. and Naumann, D., 2010. Terahertz spectroscopy: The renaissance of far infrared spectroscopy. *Journal of Molecular Structure*,*964*(1), pp.1-4.

[71] Woodward, R.M., Cole, B.E., Wallace, V.P., Pye, R.J., Arnone, D.D., Linfield, E.H. and Pepper, M., 2002. Terahertz pulse imaging in reflection geometry of human skin cancer and skin tissue. *Physics in medicine and biology*, *47*(21), p.3853.

[72] Tonouchi, M., 2007. Cutting-edge terahertz technology. *Nature photonics*,*1*(2), pp.97-105.

[73] Crowe, T.W., Porterfield, D.W., Hesler, J.L., Bishop, W.L., Kurtz, D.S. and Hui, K., 2005, May. Terahertz sources and detectors. In *Defense and Security* (pp. 271-280). International Society for Optics and Photonics.

[74] Sowade, R., Breunig, I., Mayorga, I.C., Kiessling, J., Tulea, C., Dierolf, V. and Buse, K., 2009. Continuous-wave optical parametric terahertz source. *Optics express*, *17*(25), pp.22303-22310.

[75] Lee, A.W.M., Kao, T.Y., Burghoff, D., Hu, Q. and Reno, J.L., 2012. Terahertz tomography using quantum-cascade lasers. *Optics letters*, *37*(2), pp.217-219.

[76] Scheller, M., Paul, J.R., Laurain, A., Young, A., Koch, S.W. and Moloney, J.V., 2014, March. Terahertz generation by difference frequency conversion of two single-frequency VECSELs in an external resonance cavity. In *SPIE LASE*(pp. 89660E-89660E). International Society for Optics and Photonics.

[77] Lukowski, M., Hessenius, C. and Fallahi, M., 2015. Widely Tunable High-Power Two-Color VECSELs for New Wavelength Generation. *Selected Topics in Quantum Electronics, IEEE Journal of*, *21*(1), pp.432-439.

[78] Kuznetsov, M., Hakimi, F., Sprague, R. and Mooradian, A., 1997. High-power (> 0.5-W CW) diode-pumped vertical-external-cavity surface-emitting semiconductor lasers with circular TEM/sub 00/beams. *Photonics Technology Letters, IEEE*, *9*(8), pp.1063-1065.

[79] Bückers, C., Imhof, S., Thränhardt, A., Hader, J., Moloney, J.V. and Koch, S.W., 2009. Microscopic modeling of quantum well gain media for VECSEL applications. *Selected Topics in Quantum Electronics, IEEE Journal of*, *15*(3), pp.984-992.

[80] Hader, J., Moloney, J.V., Koch, S.W. and Chow, W.W., 2003. Microscopic modeling of gain and luminescence in semiconductors. *Selected Topics in Quantum Electronics, IEEE Journal of*, *9*(3), pp.688-697.

[81] Bückers, C., Thränhardt, A., Koch, S.W., Rattunde, M., Schulz, N., Wagner, J., Hader, J. and Moloney, J.V., 2008. Microscopic calculation and measurement of the laser gain in a (GaIn) Sb quantum well structure. *Applied Physics Letters*, *92*(7), p.071107.

[82] Bückers, C., Blume, G., Thränhardt, A., Schlichenmaier, C., Klar, P.J., Weiser, G., Koch, S.W., Hader, J., Moloney, J.V., Hosea, T.J.C. and Sweeney, S.J., 2007. Microscopic electroabsorption line shape analysis for Ga (AsSb) / GaAs heterostructures. *Journal of applied physics*, *101*(3), p.033118.

[83] Raja, M.Y.A., Brueck, S.R., Osinski, M., Schaus, C.F., McInerney, J.G., Brennan, T.M. and Hammons, B.E., 1989. Resonant periodic gain surface-emitting semiconductor lasers. *Quantum Electronics, IEEE Journal of*, *25*(6), pp.1500-1512.

[84] Houghton, D.C., Davies, M. and Dion, M., 1994. Design criteria for structurally stable, highly strained multiple quantum well devices. *Applied physics letters*, *64*(4), pp.505-507.

[85] http://e6cvd.com/us/application/thermal.html

[86] Hodgson N and Horst W., 2005. *Laser resonators and beam propagation*.

[87] Svelto, O., 2010. *Principles of lasers*. Science+Business Media

[88] http://www.dataray.com/beammap2-4xy-scanning-slit-beam-profiler.html

[89] Kogelnik, H. and Li, T., 1966. Laser beams and resonators. *Applied optics*, *5*(10), pp. 1550-1567.

[90] Fallahi, M., Hessenius, C. and Lukowski, M.L., The Arizona Board of Regents On Behalf of the University of Arizona, 2016. *Multi-chip VECSEL-based laser tunable independently at multiple wavelengths*. U.S. Patent 9,231,373.

[91] Zhang, F., Gaafar, M., Moller, C., Stolz, W., Koch, M. and Rahimi-Iman, A., 2016. Dual-wavelength emission from a serially-connected two-chip VECSEL. *IEEE Photonics Technology Letters*, 28(8), pp. 927-929,

[92] Jasik, A., Sokół, A.K., Broda, A., Sankowska, I., Wójcik-Jedlińska, A., Wasiak, M., Kubacka-Traczyk, J. and Muszalski, J., 2016. Dual-wavelength vertical external-cavity surface-emitting laser: strict growth control and scalable design. *Applied Physics B*, *122*(2), pp.1-8.

[93] Johnston, T.F., 1998. Beam propagation (M 2) measurement made as easy as it gets: the four-cuts method. *Applied optics*, *37*(21), pp.4840-4850.

[94] Boyd, R.W., 2003. *Nonlinear optics*. Academic press.

[95] Boulnois, J.L., 1986. Photophysical processes in recent medical laser developments: a review. *Lasers in Medical Science*, *1*(1), pp.47-66.

[96] Kilmer, S.L. and Anderson, R., 1993. Clinical Use of the Q-Switched Ruby and the Q-Switched Nd: YAG (1064 nm and 532 nm) Lasers for Treatment of Tattoos. *The Journal of dermatologic surgery and oncology*, *19*(4), pp.330-338.

[97] Latina, M.A., Sibayan, S.A., Shin, D.H., Noecker, R.J. and Marcellino, G., 1998. Q-switched 532-nm Nd: YAG laser trabeculoplasty (selective laser trabeculoplasty): a multicenter, pilot, clinical study. *Ophthalmology*, *105*(11), pp.2082-8.

[98] Yariv, A. and Yeh, P., 1984. *Optical waves in crystals*. Wiley, New York.

[99] Boeuf, N., Branning, D., Chaperot, I., Dauler, E., Gue, S., Jaeger, G., Muller, A. and Migdall, A., 2000. Calculating characteristics of noncollinear phase matching in uniaxial and biaxial crystals. *Optical Engineering*, *39*(4), pp.1016-1024.

[100] Nikogosyan, D.N., 2006. *Nonlinear optical crystals: a complete survey*. Springer Science & Business Media.

[101] Boyd, G.D. and Kleinman, D.A., 1968. Parametric interaction of focused Gaussian light beams. *Journal of Applied Physics*, *39*(8), pp.3597-3639.

[102] Broyer, M., 1985. Intracavity cw difference frequency generation by mixing three photons and using Gaussian laser beams. *Journal de Physique*, *46*(4), pp.523-533.

[103] Zondy, J.J., 1998. The effects of focusing in type-I and type-II difference-frequency generations. *Optics communications*, *149*(1), pp.181-206.

[104] http://www.bristol-inst.com/_literature_178663/771_Series_Specifications

[105] Richter, D., Fried, A. and Weibring, P., 2009. Difference frequency generation laser based spectrometers. *Laser & Photonics Reviews*, *3*(4), pp.343-354.

[106] http://gentec-eo.com/Content/downloads/specifications-sheet/THZ-D_2014_V1.0.pdf